technische universität dortmund

astroparticle physics

Saving Time and Money for Monte Carlo

Estimation of Instrument Response Functions as an Alternative Approach to Minimize the Cherenkov Telescope Array Observatory's Need for Simulations

Rune Michael Dominik

2024

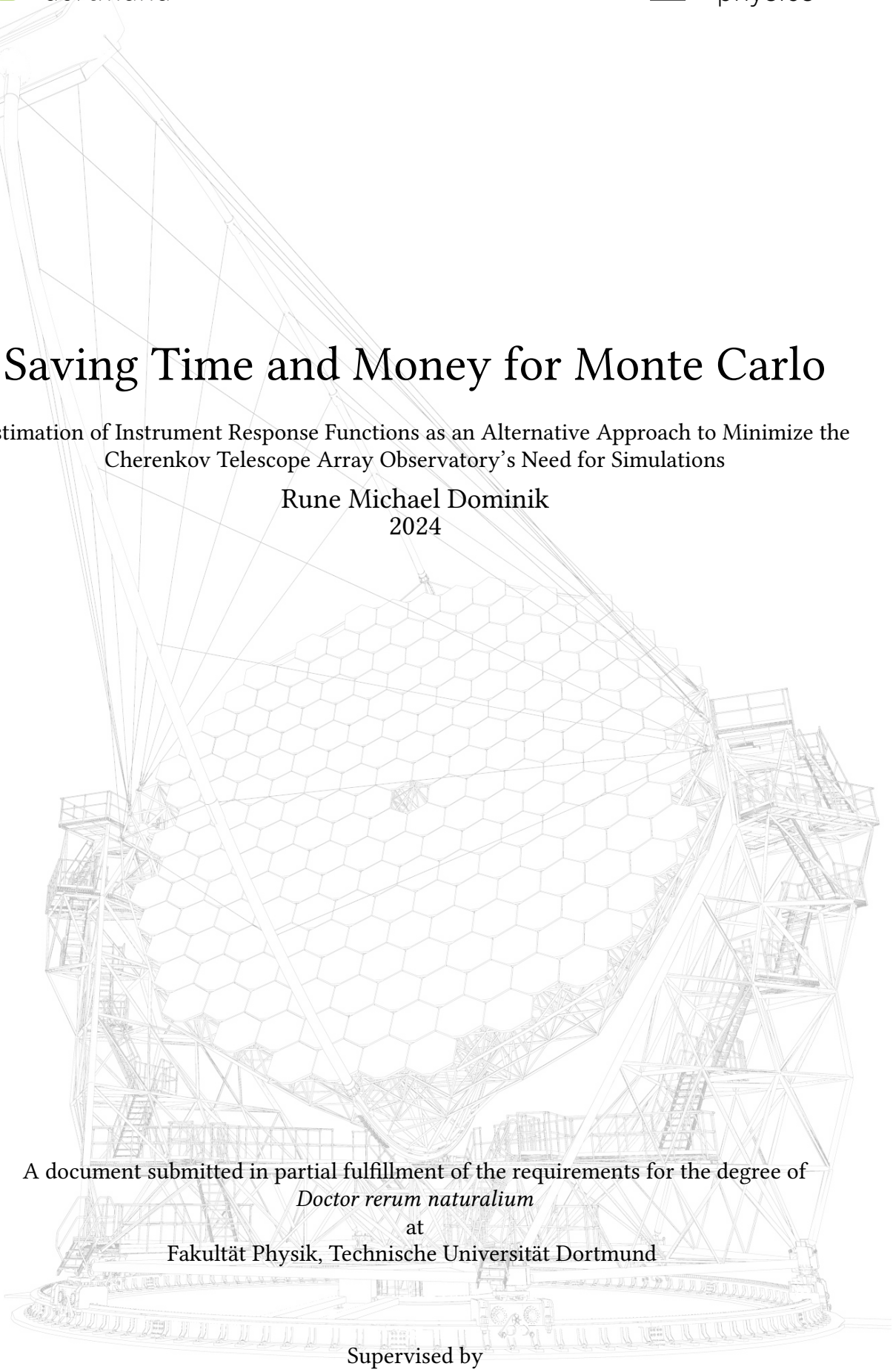

A document submitted in partial fulfillment of the requirements for the degree of
Doctor rerum naturalium
at
Fakultät Physik, Technische Universität Dortmund

Supervised by
Prof. Dr. Dr. Wolfgang Rhode and Prof. Dr. Julia Tjus

This thesis is set in Libertinus (Serif, Sans and Math) and Fira Code,
typeset using LaTeX with LuaTeX and BibLaTeX through TeX-Live 2024.
Title graphic by K. Brügge, layout altered from M. Linhoff.

Abstract

The Cherenkov Telescope Array Observatory (CTAO) will be the next-generation ground-based very-high-energy (VHE) gamma-ray observatory once its construction and commissioning are finished. Like its predecessors, CTAO relies on Instrument Response Functions (IRFs) to relate the observed and reconstructed properties to the true ones of the primary gamma-ray photons and thus reconstruct spectral and spatial information of the observed sources. As IRFs are derived from Monte Carlo simulations and depend on observation conditions like telescope pointing and atmospheric transparency, producing a complete set of IRFs is a time-consuming task and not feasible when analyzing data on short timescales. To facilitate the production of optimized IRFs in such scenarios, this work studies the use of inter- and extrapolation algorithms to quickly compute IRFs from a pre-computed grid for the Large-Sized Telescope prototype (LST-1) using the `pyirf python` software package. As some constituents of an IRF are given as probability distributions, specialized methods are needed.

Using 35.9 h of LST-1 Crab Nebula observation taken with zenith angles up to 35 deg, this thesis shows the compatibility of estimated IRFs and a nearest neighbor approach on the provided LST-1 simulation grid. When using sparser grids, estimated IRFs maintain a stable performance well beyond the point where the nearest neighbor approach can no longer yield reasonable results. Applying estimated IRFs to observations of NGC 1275 from December 2022 and January 2023 in the same zenith range shows clear signs of two flares in this period, matching the signature obtained from past events. Estimated IRFs present themselves to be fully capable of being used with LST-1 analyses in a zenith range of up to 35 deg.

Kurzfassung

Das Cherenkov Telescope Array Observatory (CTAO) wird, sobald sein Bau und seine Inbetriebnahme abgeschlossen sind, das bodengestützte hochenergie Gammastrahlen-Observatorium der nächsten Generation sein. Wie seine Vorgänger stützt sich CTAO auf Antwortfunktionen (IRFs), um die beobachteten und rekonstruierten Eigenschaften mit den wahren Eigenschaften des ursprünglichen Photons in Beziehung zu setzen und so die spektralen und räumlichen Informationen der beobachteten Quellen zu rekonstruieren. Da IRFs aus Monte Carlo-Simulationen berechnet werden und von Beobachtungsbedingungen wie Teleskopausrichtung und atmosphärischer Transparenz abhängen, ist die Erstellung eines vollständigen Satzes von IRFs eine zeitaufwändige Aufgabe und bei der Analyse von Daten auf kurzen Zeitskalen nicht möglich. Um die Erstellung von optimierten IRFs in solchen Szenarien zu ermöglichen, wird in dieser Arbeit die Verwendung von Inter- und Extrapolationsalgorithmen zur schnellen Berechnung von IRFs aus einem vorberechneten Gitter für den Prototyp des Large-Sized Telescope (LST-1) unter Verwendung des `pyirf python` Softwarepaket untersucht. Da einige Bestandteile einer IRF durch Wahrscheinlichkeitsverteilungen gegeben sind, werden spezialisierte Methoden benötigt.

Anhand von 35.9 Stunden LST-1 Krebsnebelbeobachtung mit Zenitwinkeln bis zu 35 deg wird in dieser Arbeit die Kompatibilität der geschätzten IRFs und eines nächste-Nachbar Ansatzes auf dem bereitgestellten LST-1 Simulationsgitter gezeigt. Bei der Verwendung von weniger dicht besetzten Gittern behalten die geschätzten IRFs auch jenseits des Punktes, ab dem der nächste-Nachbar Ansatz keine nutzbaren Ergebnisse mehr liefern kann, eine stabile Leistung bei. Die Anwendung der geschätzten IRFs auf Beobachtungen von NGC 1275 vom Dezember 2022 und Januar 2023 im selben Zenitbereich zeigt deutliche Anzeichen für zwei Strahlungsausbrüche in diesem Zeitraum, die mit der Signatur von vergangenen, vergleichbaren Ereignissen übereinstimmen. Die geschätzten IRFs zeigen eine uneingeschränkte Eignung für LST-1-Analysen in einem Zenitbereich bis zu 35 Grad.

Contents

1 Introduction

For millennia, astronomical observations have fascinated human beings, providing wonder and mystery and aiding them in tasks such as time-keeping and navigation. While early cultures could only study objects visible to the naked eye, telescopes became available in the late Renaissance. It took astronomy until the 19th century to develop into modern science, paving the way for astrophysics while still being constrained by the physical limitations of the human eye to electromagnetic radiation with wavelengths between about 380 and 750 nm. Even though infrared light was discovered by William Herschel in 1800 in sunlight [72], it took until the beginning of the 20th century for the first extrasolar observations outside the optical range by Edward Leamington Nichols, who detected the stars Vega and Arcturus in infrared [116].

A groundbreaking discovery, pioneering the field of astroparticle physics, was made by Victor Hess in 1912. During balloon flights, he observed increased levels of ionizing radiation with increasing height, calling the phenomenon "Höhenstrahlung" [73]. In retrospect, this was the first indirect observation of charged cosmic rays, high-energy protons and heavier atomic nuclei. These particles interact in the atmosphere, forming Extended Air Showers (EAS) whose subcomponents Hess could detect. While his discovery fueled particle physics and awarded Hess the 1936 Nobel Prize in Physics, it took astrophysics 50 more years to observe actual distant objects in these high energies.

Until then, the 20th century, fueled by technological advances, brought further insights into the electromagnetic spectrum. After the dawn of radioastronomy (1932, [86]) and X-ray astronomy (1948, [87]), several space-bound experiments, such as Explorer XI (1961) and the Orbiting Solar Observatories (from 1967), detected the first astrophysical gamma-ray photons, unable to pinpoint actual sources. From there, the second half of the 20th century gave rise to several successful experiments, pushing further into the highest energies [111], resulting in three main constituents to probe different high-energy ranges. Space-bound telescopes, most notably the *Fermi Gamma-ray Space Telescope*'s Large Area Telescope (*Fermi*-LAT) [22], provide insight into MeV to a few hundred GeV photons, constrained by a satellite's limited collection area. The needed increase in collection area to observe between a few tens of GeV and some ten TeV is provided by Imaging Air Cherenkov Telescopes (IACTs), employing indirect but ground-based measurements of gamma rays in this very-high-energy (VHE) band. With the current construction and commissioning of the next generation IACT experiment, the Cherenkov Telescope Array Observatory (CTAO), this threshold will be extended past 100 TeV [48]. The highest currently reachable energies, referred to as ultra-high-energies, are probed by the LHASSO experiment by combining multiple subsystems, resulting in detecting the first sources at PeV energies in 2021 [40].

This availability of broad sections of the electromagnetic spectrum gave rise to the so-called multi-wavelength astronomy, where the combination of measurements from multiple experiments offers

the most detailed insights into astrophysical phenomena. During the 21st century, this approach was extended to multi-messenger astronomy, combining multi-wavelength astronomy, neutrino astronomy, and, the most recent contribution, gravitational wave signals. However, the list of identified neutrino sources with existing electromagnetic counterparts is short. The most recent addition is the observation of the galactic plane [82].

As each discovery in multi-wavelength and multi-messenger astronomy aids the goal of probing the mechanisms at work in the universe's most extreme environments, cooperation between multiple experiments is mandatory. Most noticeably, this includes mutual observations of transient events, short time-scale phenomena such as gamma-ray bursts, or flaring activity of known sources. These events will be detected by CTAO and a Real-Time Analysis (RTA) will be needed to alert other experiments to perform follow-up observations. To provide high-level data products like Spectral Energy Distributions (SEDs), CTAO relies on Instrument Response Functions (IRFs) to establish a relation between the observed and reconstructed events and the actual properties of the primary photons. While these IRFs depend on observation conditions such as telescope pointing and have to be computed from extensive Monte Carlo simulations, the short time scales of a RTA require alternative approaches. One such approach is the estimation of IRFs through inter- and extrapolation from an existing grid of precomputed IRFs for different observation conditions. This thesis aims at providing such methods and assessing their feasibility.

To do so, chapter 2 provides an insight into gamma-ray astronomy, including the sources and the indirect detection principle used by IACTs. Next, chapter 3 introduces CTAO, focusing on the Large-Sized Telescope prototype LST-1 that is already actively observing. A discussion of the IRFs and further tools needed to perform a LST-1 data analysis follows in chapter 4. This chapter also introduces the inter- and extrapolation schemes and assesses their performance. Estimated IRFs are further tested with two prominently known astronomical sources: the Crab Nebula in chapter 5 and NGC 1275 in chapter 6. While the Crab Nebula, the remnant of supernova SN 1054, was the first confirmed VHE gamma-ray source and has, since its detection by the Whipple IACT experiment, served as the standard candle of gamma-ray astronomy [132], NGC 1275 is one of the few known TeV radio galaxies. Given its known tendency to flare up to TeV energies [17] and signs for precession found in an earlier work [52], hinting at a supermassive black hole binary inside its Active Galactic Nucleus (AGN), NGC 1275 is a prime candidate for a source that will experience a transient event in the future, thus providing an actual use-case where IRF estimation will be needed. Concluding this thesis, chapter 7 will summarize the results and present an outlook on future developments.

Very-High-Energy Gamma-Ray Astronomy and Astroparticle Physics

2

Modern multi-messenger and multi-wavelength astronomy combines many experiments to collect as much information about astrophysical sources as possible. The most extreme astrophysical sources can emit radiation up to and beyond the VHE band between tens of GeV and hundreds of TeV. Even though Earth's atmosphere is opaque to particles at these energies, traces of interactions can be detected at ground level using IACT experiments. This chapter briefly introduces the field of VHE gamma-ray astronomy. It discusses sources and mechanisms to accelerate particles to the needed energies, their propagation to the Earth, and the detection principles for IACTs.

2.1 Sources of VHE Gamma-Rays

Distinct sources of VHE gamma-ray emission have been known since the late 20th century when the Whipple telescope first observed the Crab Nebula nebula [132], a supernova remnant, in 1989. From there, numerous experiments detected a variety of different source types. As collected in the TeVCat catalog [131], 308 sources of TeV emission are currently listed, distributed over the whole observable sky as shown in Figure 2.1. In the neighboring, slightly lower energy-band between 50 MeV and 1 TeV, *Fermi*-LAT has detected over 7000 sources during 14 years of service, collected in their 4FGL-DR4 catalog [4, 24].

2.1.1 Active Galactic Nuclei

Among the extragalactic emitters of VHE gamma rays, Active Galactic Nuclei (AGN) are the most noumerously observed subclass, contributing about 92 % of all identified extragalactic sources to TeVCat. While Thomas Wright first formulated the idea of the existence of galaxies outside our own Milky Way in 1750, the first evidence of strong emitting sources inside their nuclei was found by Seyfert in 1943 [120]. During the following decades, the nature of these nuclei and their energy output was widely discussed, eventually arriving at the idea of accretion processes onto massive objects converting gravitational energy to electromagnetic emission [119]. This basic model persists to this day; AGN are assumed to be hosts to Super Massive Black Holes (SMBH) that, together with the surrounding matter, drive the observed radiation from low-energy radio waves to VHE gamma rays.

The AGN unification scheme

The modern view on AGN attributes multiple, formerly allegedly distinct, source classes to different facets of the same object. This unified model of AGN, shown in Figure 2.2 and following [70],

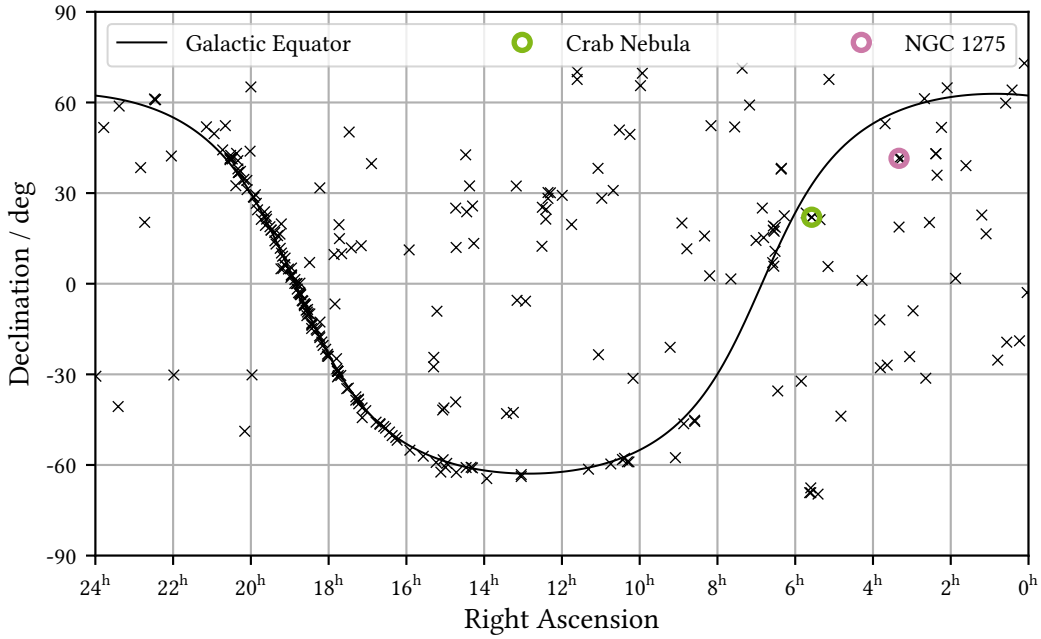

Figure 2.1: All 275 TeVCat [131] sources in International Celestial Reference System (ICRS) coordinates, 1^h of Right Ascention is equal to 15 deg. The Crab Nebula and NGC 1275 are highlighted.

assumes a geometrically thin and optically thick accretion disc around the central SMBH, from which a relativistic jet can emerge. With this disc's extreme UV through optical emission along an outwards-going temperature gradient, upscattered by inverse-Compton processes up to X-ray energies, the broad- and narrow-line regions (BLR and NLR) are ionized and heated. The BLR is assumed to consist of high-density gas clouds with velocity dispersions in the order of 1000 km/s. Thus emission lines induced through heating these clouds are severely Doppler-broadened. The further out NLR is less dense and has a lower velocity-dispersion. Thus, the Doppler-broadening of emission lines is less prominent yet still existent. Both regions emit in UV-, optical, and infrared wavelengths. Due to the lower densities in the NLR, otherwise forbidden emission lines are present since meta-stable states are, in contrast to the BLR, not collisionally de-excited [110]. Ranging beyond the NLR, a dust torus obscures the line of sight onto the accretion disc from certain viewing angles onto the AGN. This torus absorbs emission from the inner structure, re-emitting in the infrared.

With this model, the appearance of an AGN is now highly dependent on the viewing angle [128]. If the AGN features a jet in alignment with the line of sight onto the source, thus having the observer look down the jet, AGN are designated Blazars, showing emission over the whole electromagnetic spectrum. As the jet accounts primarily for high-energy radiation, Blazars are the most common class of VHE observed AGN, accounting for 83 of the current 90 AGN in TeVCat. Blazars are further divided into BL Lac objects, named after the first observed specimen, BL Lacertae, characterized by a lack of emission lines. These lines are present in observations of Flat Spectrum Radio Quasars (FSRQs). Both subclasses show the same underlying phenomena: high luminosity and rapid

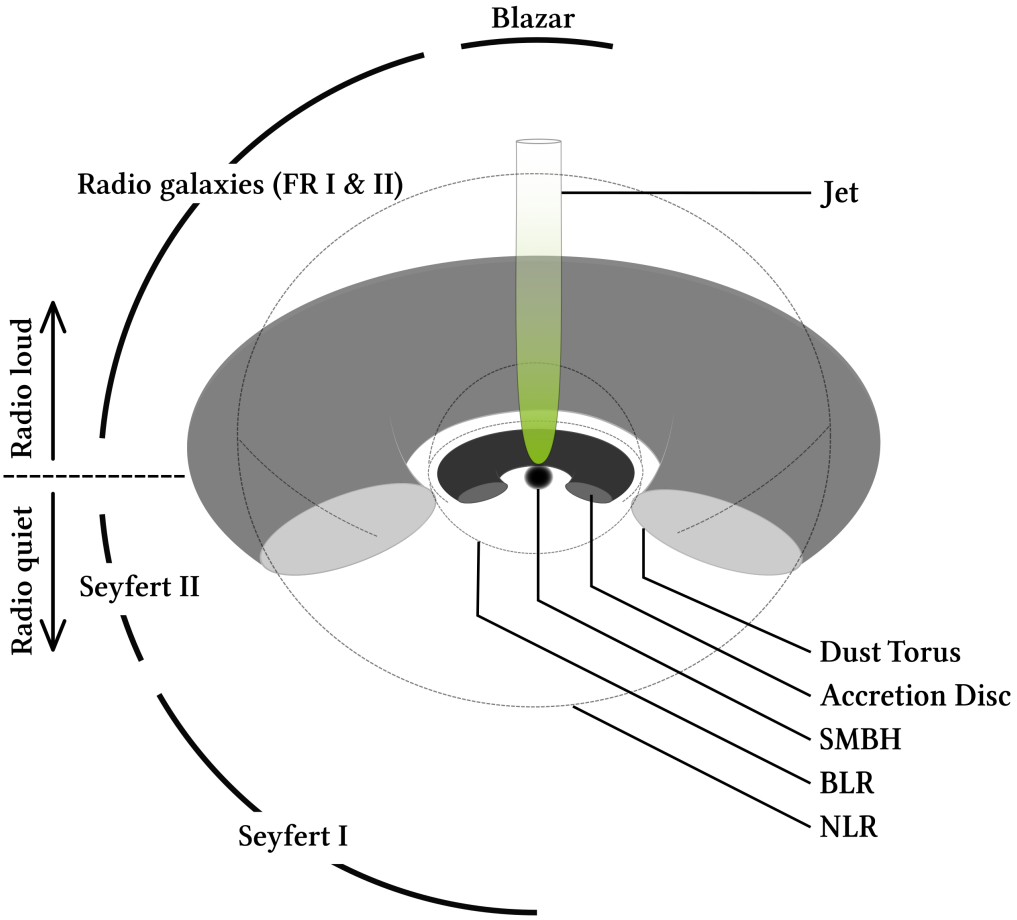

Figure 2.2: Schematic view of an AGN according to the unified model with the upper half representing radio-loud and the lower half radio-quiet AGN. Emission from an accretion disc surrounding the central SMBH illuminates BLR and NLR. A dust torus obscures the view onto the BLR and the accretion disc from certain viewing angles. Additionally, a powerful, in reality two-sided, jet is emitted perpendicular to the accretion disc.

variability. If the line of sight is more tilted with respect to the jet axis but still shows high emissions in radio wavelengths, AGN are designated as radiogalaxies. A further distinction into the Fanaroff-Riley (FR) types I and II is often applied, where FR I AGN show strong emission from the jet whereas FR II AGN feature lobes more outwards from the jet base that account for most of the radio emission. Together with the Blazars mentioned above, FR radio galaxies constitute the class of radio-loud AGN due to their strong radio emission. Emission in TeV energies from FR radio galaxies is, however, rare. AGN with weak radio signals and without relativistic jets are designated Seyfert galaxies, depending on whether they show emission from the BLR (Seyfert I) or NLR (Seyfert II) in cases where the dust torus obscures the BLR with respect to the line of sight. These two Seyfert types form the majority of the so-called radio-quiet AGN. Further subdivisions of these AGN classes and intermediate types of course exist, and while this unification scheme is widely accepted, observations of, e.g., Low-Ionization Nuclear Emission-line Regions (LINERs) in nuclei challenge it, leading to more distinctive differentiation between AGN types (see, e.g., [70]).

The case of NGC 1275

One well-studied specimen of AGN is NGC 1275, also known as 3C 84, the nucleus to the central galaxy in the constellation of Perseus, Perseus A, located at a redshift of $z = 0.0176$ (about 100 Mpc). Together with its neighboring AGN IC 310, NGC 1275 can be studied in observations of the so-called Perseus-MA, a mock-up source in between both AGN that ensures both sources to be in an IACT's field-of-view at the same time and offset.

Despite being close and often observed, multiple features of NGC 1275 are unclear, starting with its classification in the aforementioned AGN model. Often cited as FR I [45], classifications also include Seyfert II [33] and Blazar of uncertain type [96]. Regardless of this uncertainty, NGC 1275 is one of the few radio galaxies also detected in TeV energies [17].

In addition to this rare classification as TeV radio galaxy, NGC 1275 exhibits multiple interesting phenomena:

- NGC 1275 shows strong and recurring flaring activity, e.g., during New Year's Eve 2016/2017 [17] as well as in December 2022 [46] and in January 2023 [135],
- NGC 1275 has shown at least one occurrence where the jet restarted and changed its structure [106],
- NGC 1275 shows strong signs of jet precession, hinting at underlying phenomena like, e.g., a binary SMBH; this result from an earlier work was published in Dominik, Linhoff, Elsässer, and Rhode [52].

Especially the flaring is a strong indicator that future observations of NGC 1275 will randomly discover another flare and thus alert other telescopes to follow-up observations. Given that, NGC 1275 is a prime use case for a short time-scale analysis using interpolated IRFs.

Open Questions

Even though Seyfert's AGN observations are nearing their centennial and studies have been intensively ongoing ever since, AGN physics still needs to be understood entirely. CTAO will

dedicate a whole key science program to the observation of AGN, aiming to answer open questions formulated in [48] (selection):

- What are the relevant acceleration and emission processes in VHE Blazars?
- What causes the observed variability in AGN?
- From where does the VHE emission of radio galaxies originate?
- Do other classes of AGN emit VHE gamma rays?

The third question especially implies frequent future NGC 1275 observations by CTAO.

2.1.2 Supernovae and Their Remnants

Another source of VHE emission are Supernova Remnants (SNRs). Contrary to AGN, SNRs are mainly observed inside the Milky Way and are thus not necessarily extragalactic sources. However, there have been occurrences where a supernova was observed outside the Milky Way, e.g. SN 1987a in the Large Magellanic Cloud, a satellite galaxy to the Milky Way [19].

A supernova is an event in the later stages of a star's lifecycle. After burning through its reservoir of fusionable elements, at some point, the produced elements cannot be processed further due to insufficent temperature and pressure or as fusion of iron and nickel does not produce an energy output. As these elements require the most extreme temperatures and pressures to form, they accumulate inside the star's core. From there on, two main paths to ignite a supernova are theorized. In binary systems, the heavier and thus more short-lived star will eventually enter a white dwarf state after an intermediate giant phase, hurling away its outer hydrogen-rich layers, which are partially accreted by the secondary star. With time, the separation between the binary partners decreases, and the secondary star will also enlarge in the later stages of its lifecycle. The white dwarf starts to accrete mass from the secondary star, processing fusionable elements to heavier ones until the non-fusionable mass, stabilized by electron degeneracy, comes close to the Chandrasekhar limit. At some point, the increased inwards-facing gravitational pressure results in an environment that allows the remaining elements to fuse into heavier ones in seconds, producing a tremendous energy output. This path is designated thermonuclear or type Ia supernova [77]. The second possible path applies to stars heavier than 8 $M_\odot$, heavy enough to fuse their initial material until the inert core itself exceeds the Chandrasekhar limit. When the core's electron degeneracy can no longer withstand the gravitational compression the core implodes, sending strong shockwaves through its surrounding medium and hurling away the star's outer shells. While the exact nature of the exploding process is still the subject of current research, this supernova type is called core-collapse or type II supernova [39] in the presented scenario, or type Ib and Ic if the progenitor star has lost its outer hull before the explosion. While the expanding outer shells create a nebula, the shock waves propagating through it induce the emission of a wide range of wavelengths up to gamma rays [115], making supernovae sources of VHE emission.

In the meantime, the former core of the star has been mainly converted to neutrons. The newly created neutron star, considerably smaller than the original star, is stabilized by the degeneracy pressure of the neutrons. If the gravitational force again outweighs this pressure, a black hole is

thought to be formed [39]. In both cases, the resulting object conserved its precursor's magnetic field and angular momentum but confined both to smaller scales [83]. If the precursor star was thus rotating, a neutron star would also do so, yet considerably faster. Combined with the increased magnetic field densities, such an object can emit beams of high energy radiation from its magnetic poles that can then be periodically detected on Earth. These pulsars also hurl out winds from their magnetosphere, accelerating particles to relativistic speeds and causing emission throughout the electromagnetic spectrum. This phenomenon is called Pulsar Wind Nebula (PWN). In general, particle acceleration in SNRs and PWN are thought to be similar to those described for AGN [61].

The Crab Nebula

One such PWN is the Crab Nebula. The supernova creating the Crab Nebula was observed in 1054 by Chinese and Japanese astronomers, being visible for 23 days in daylight [112]. Even though interest in this "guest star" eventually faded in ancient times, modern-day astronomy has extensively studied the Crab Nebula in multi-wavelength campaigns, especially since it is a well-dated, comparably young and luminous source. Figure 2.3 shows a composition of infrared observations of the Crab Nebula.

Figure 2.3: Cutout from NASA's James Webb Space Telescope observations of the Crab Nebula in near- and mid-infrared. Gaseous filaments (red-orange) and dust emissions (yellow-white and green) are visible. Synchrotron radiation can be seen as white mist overlaying the image, seemingly originating from the Crab Nebula's central engine, its pulsar, the small white dot in the center of the image. Image: NASA, ESA, CSA, STScI, T. Temim (Princeton University).

Due to its comparably constant flux in VHE, the Crab Nebula is the standard candle of gamma-ray astronomy [100] and thus often used as a cross-check for novelty analysis methods and even as a

flux unit with 1 CU (Crab Unit) being either the differential flux at or the integrated flux above a certain energy. A reference Spectral Energy Distribution (SED) of the Crab Nebula was measured with the MAGIC telescopes [10] and log-parabola parametrized as

$$\Phi(E) = 3.23 \times 10^{-11} \left(\frac{E}{1\,\mathrm{TeV}}\right)^{-2.47-0.24\log_{10}(E/1\,\mathrm{TeV})} \mathrm{TeV}^{-1}\mathrm{cm}^{-2}\mathrm{s}^{-1} \tag{2.1}$$

which integrates to a flux of

$$\int_{0.1\,\mathrm{TeV}}^{\infty} \Phi(E)\,\mathrm{d}E \approx 4.76 \times 10^{-10}\,\mathrm{cm}^{-2}\,\mathrm{s}^{-1} \approx 0.4\,\mathrm{m}^{-2}\,\mathrm{d}^{-1} \tag{2.2}$$

above 100 GeV, showing the limitations of space bound experiments such as *Fermi*-LAT. Both references will be used throughout this work.

As discussed in [100], the high-energy emission of the Crab Nebula is sufficiently well described by a leptonic model. Four seed photon populations contribute to the high-energy flux by being upscattered through relativistic electrons in the nebula in inverse-Compton processes. The seed photons originate from synchrotron, thermal, and line emissions as well as from the Cosmic Microwave Background CMB.

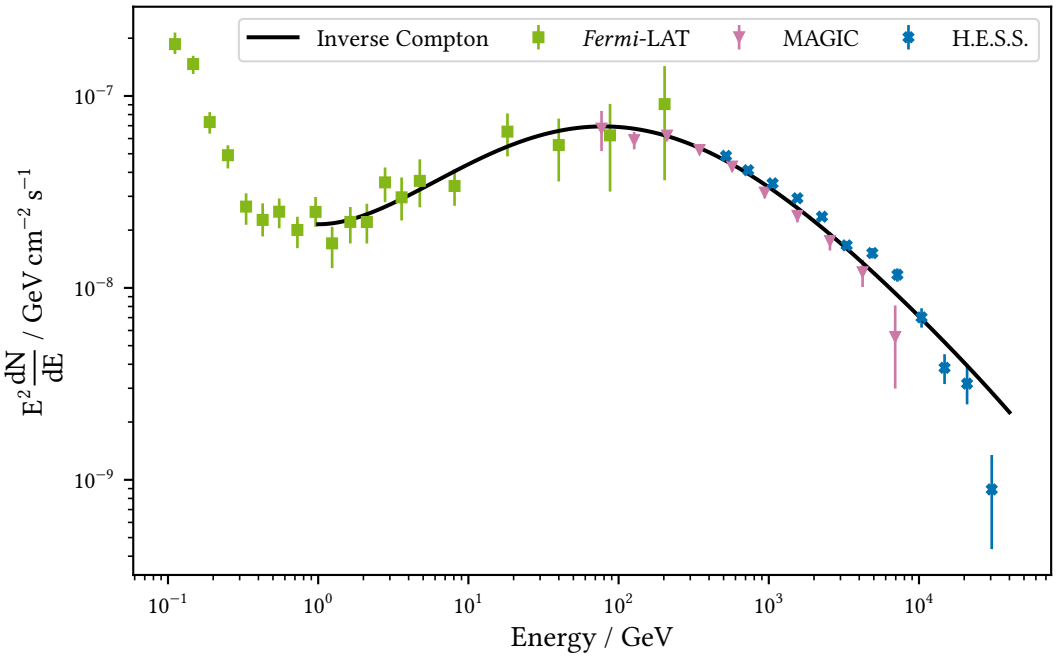

Figure 2.4: SED of the Crab Nebula at high energies with data by *Fermi*-LAT [3], H.E.S.S. [8] and MAGIC [10], together with the flux predicted by modeling inverse Compton emission, originally published in [100].

2.1.3 Transient Events

A final class of events detectable in VHE are transient events, significant to the science case of CTAO and one of its key science projects [48] next to CTAO's dedicated AGN flare program. Transients

are a collection class of multiple different events that are characterized by short time-scale changes of the underlying source's flux. These include sources that experience outbursts of electromagnetic energy, e.g., in gamma-ray bursts, but also events detected using different messenger particles like neutrinos and gravitational waves to further enhance multi-messenger astronomy.

While most of CTAOs transient event monitoring will be triggered by dedicated monitoring experiments and consequently be follow-up observed by CTAO, chances are that CTAO will observe, e.g., a flaring source during routine observations. As discussed in subsection 2.1.1, this might be seen observing NGC 1275 and its neighbor IC 310, both known for past and present flaring activity (see [17] and [9]). CTAO will issue alerts to other facilities to maximize science output, just as current experiments already do. To do so, CTAOs RTA will continuously monitor the data taken and produce data products on short time scales, internally designated CAT-A data products. One of the primary use cases of this work's result is to take part in producing such quick-look results and thus enable CTAO to trigger multi-experiment observations of promising astrophysical events.

2.1.4 Acceleration of Particles and Emissions at VHE-Energies

From multi-wavelength observations of multiple sources, including the Crab Nebula, most sources of VHE emission show a distinctive double-bump SED. The simplest used model describing this is the so-called one-zone Synchroton Self-Compton (SSC) model. In this model, relativistic electrons emit photons by synchrotron emission when moving through the source's magnetic fields. These photons are then, in turn, up-scattered to higher energies by inverse Compton processes with the same electron population

$$\gamma_{\text{Sync.}} + e^- \rightarrow \gamma_{\text{IC.}} + e^-. \tag{2.3}$$

In this SSC model, the synchrotron emission, the first of the two bumps, inherits a modified version of the injected electron spectrum. Following [60], assuming an electron power-law with spectral index Γ_e, the differential photon SED shows a rise with a spectral index of

$$\Gamma_{\text{Sync.}} = \frac{\Gamma_e + 1}{2}. \tag{2.4}$$

Energy losses through the synchrotron radiation and small energy transfers from inverse Compton processes in the Thompson regime then modify the injected electron spectrum to $\Gamma_e \rightarrow \Gamma_e + 1$, thus changing the photon spectral index to

$$\Gamma_{\text{Sync.}} = \frac{\Gamma_e + 2}{2}. \tag{2.5}$$

At some point, inverse Compton processes transfer all energy from an electron to upscattered photons, thus causing the breakdown of the synchrotron peak in the so-called Klein-Nishina regime. The upscattering of the synchrotron photons in the already mentioned inverse Compton processes results in spectral indices of

$$\Gamma_{\text{IC}} = \begin{cases} \frac{\Gamma_e+1}{2}, & \text{Thompson regime} \\ \Gamma_e + 1, & \text{Klein Nishina regime} \end{cases} \tag{2.6}$$

at the highest energies [91]. All constituents of this SSC model are sketched in Figure 2.5. In actual observations, this pure power-law scenario often proves insufficient, especially since the high

energy regime seems considerably curved, as seen in Figure 2.4. Most often, as e.g. also done for the Crab Nebula in Equation 2.1, the whole inverse Compton peak is more precisely parametrized by a log-parabola

$$N(E) = A\left(\frac{E}{E_0}\right)^{-\alpha-\beta\log_{10}(E/E_0)} \tag{2.7}$$

with three parameters A (amplitude), α (spectal index at E_0), and β (parabola curvature) at a typically fixed reference energy E_0 [97]. Second-order processes to this purely leptonic SSC model have been discussed, including the upscattering of external photons from the accretion disc or BLR line emission through the same inverse Compton process and hadronic interactions [21].

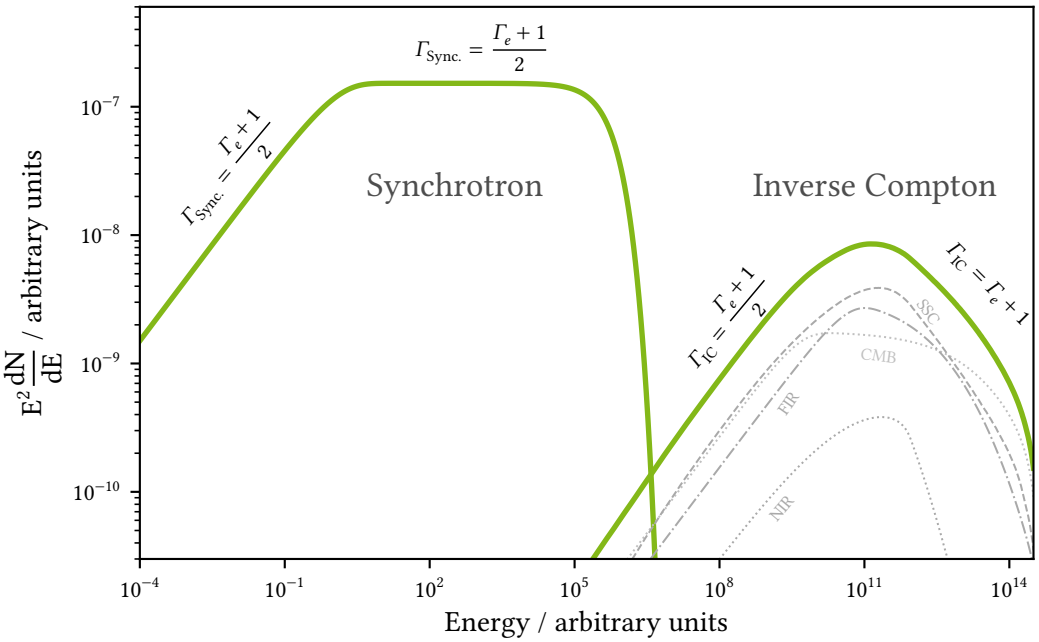

Figure 2.5: A sketch of an SSC SED, following the approach taken in [60], assuming an electron power-law with $\Gamma_e = 3$ and a synchroton loss break at 10^{12} arbitrary units. Contribution to the inverse Compton peak from synchrotron radiation is highlighted as SSC, further contributions from CMB alongside far and near-infrared (FIR/NIR) seed photon populations are also included for completion. Image created using `naima` [136] and building upon code from K. Brügge [38].

The remaining question is the source of the relativistic electrons, whose spectral shape has been assumed to follow a power law or, to fit actual observations, the log-parabola in (2.7). While the exact nature of energy conversion through an AGN's SMBH and the actual jet physics is still up to debate, shock acceleration is considered crucial to accelerate particles in SNR and AGN. This mechanism is named first-order Fermi acceleration [56] and can explain a power-law distribution of the accelerated particles. When additional scattering at the comoving magnetic fields and turbulences in the shockwaves is combined with a stochastical approach, the resulting mechanism can account for a log-parabola spectrum [127].

2.2 Charged Cosmic Rays

Near sources energetic enough to accelerate electrons to in turn produce photons up to VHE energies, the acceleration of a second class of particles is possible. These charged cosmic rays are the main background to IACT observations like those planned for CTAO and are composed of atomic nuclei from protons up to iron, with heavier nuclei becoming increasingly important with higher energies. While typically not regarded as charged cosmic rays in the communities termini, electrons and positrons provide a secondary population of charged particles arriving at Earth.

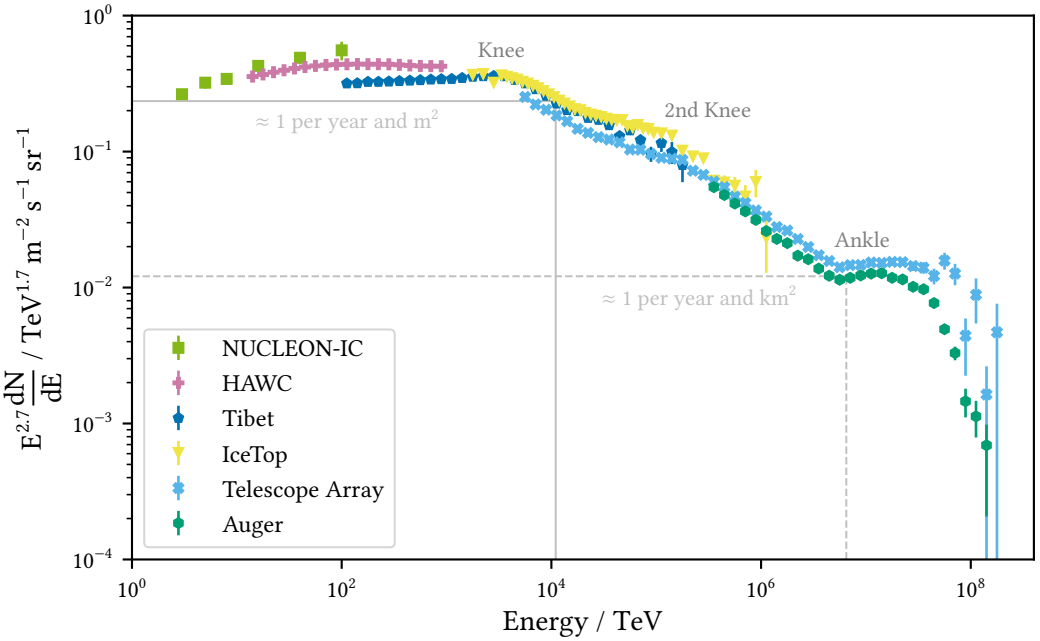

Figure 2.6: All-particle spectrum of high-energy charged cosmic rays over nearly nine orders of magnitude from 3 TeV to about 1.8×10^2 PeV, scaled by $E^{2.7}$, with statistical errors. Multiple named features (Knee, 2nd Knee, and Ankle) are highlighted. Data from NUCLEON-IC [65] (two data points omitted due to high uncertainties), HAWC [104], Tibet [14], IceTop [2], Auger [1] and the Telescope Array [84]. All data but Tibet were extracted using [99].

The sources of charged cosmic rays are mainly unknown. Identifying them is an important goal of astroparticle physics and among the possible candidates are yet again AGN. The acceleration mechanisms responsible for the charged cosmic ray flux ranging from keV up to EeV and thus 15 orders of magnitude are, again, thought to be Fermi-like shock acceleration, discussed in subsection 2.1.4. While interplanetary shocks can accelerate lower energy cosmic rays [64] and solar interactions can account for energies up to GeV and even provide a source for charged cosmic rays at these energies [89], higher energy cosmic rays, as those displayed in Figure 2.6, originate from outside our solar system. Up to about 100 PeV, acceleration in shockwaves propagating through SNRs can account for the observed population. Beyond that energy, however, processes are not certain, though AGN are considered as possible engines [26].

2.3 Propagation and Attenuation

The photons emitted by the numerous source types discussed above propagate through a nearly perfect vacuum for most of their journey. Nevertheless, occasional clouds of dust and gas attenuate the flux of photons, and even the remaining vacuum is not as empty as it might seem. The universe is filled by the so-called Extragalactic Background Light (EBL), radiation emitted by all sorts of resolved and unresolved sources from the beginning of the universe as well as thermal radiation from dust clouds. This EBL provides a considerable density of photons throughout the universe. Given photons of sufficient energy, e.g. VHE photons, the cross-section for

$$\gamma_{\mathrm{EBL}} + \gamma_{\mathrm{VHE}} \rightarrow e^+ + e^- \tag{2.8}$$

pair-production becomes non-negligible, thus providing a considerable amount of attenuation in the VHE regime. For that reason, the universe becomes opaque for VHE emission of high-redshift sources [55]. Consequently, the study of close sources such as NGC 1275 becomes more important. For energies above a few TeV, similar, yet weaker, effects may result from the galactic interstellar radiation field, galactic stellar and dust emissions, especially for sources located near the galactic center. Highest energy photons above 100 TeV, even from galactic sources, experience attenuation by pair-production with CMB photons [105]. Besides these attenuation effects, photons provide one vital characteristic: if a photon reaches Earth, it retains the information of its source position.

This is not the case for charged cosmic rays, as magnetic fields of various origins deflect them on their path to Earth and they thus arrive isotropic. Despite this, considerable interest exists in reconstructing their sources [57], especially since their extensive energy range possibly provides insight into numerous phenomena, as discussed in section 2.2. As higher energy cosmic rays are less deflected by magnetic fields, they offer the best chance to allow for some hints of their origin. Besides being increasingly rare, their flux steeply declines beyond 60 EeV as can be seen in Figure 2.6. This is thought to be the result of the Greisen-Zatsepin-Kuzmin effect [66]; the production of Delta-resonances by interaction with the CMB

$$p + \gamma_{\mathrm{CMB}} \rightarrow \Delta^+ \rightarrow p + \pi^0 \tag{2.9}$$

$$\rightarrow \Delta^+ \rightarrow n + \pi^+. \tag{2.10}$$

Heavier nuclei are predominantly thought to be subject to photodisintegration at comparable energies [121]. Nevertheless, experiments like the Telescope Array detected charged cosmic rays beyond these energies, straining existing theories [126].

2.4 Interaction with Earth's Atmosphere

As Earth's atmosphere becomes opaque to wavelengths below the near UV, VHE emission does not reach ground level. Since each VHE photon carries energy well above the pair-production threshold, an electron-positron pair is produced as soon as the photon interacts with an atmospheric atom

$$\gamma_{\mathrm{VHE}}\ (+Z) \rightarrow e^+ + e^-\ (+Z'). \tag{2.11}$$

As both leptons end with a significant amount of energy from the primary gamma ray, emitted Bremsstrahlung photons in the electromagnetic fields around nuclei in

$$e^{\pm} (+Z) \rightarrow e^{\pm\prime} + \gamma_{\text{Brems.}} (+Z') \tag{2.12}$$

processes again carry enough energy to, in turn, produce an electron-positron pair. Both processes are thus repeated, and a cascade, an electromagnetic Extended Air Shower (EAS), forms. In this EAS, the number of particles roughly doubles each iteration, halving their energy. The cascade consequently stops when the photon energy falls below the pair-production threshold. While this simplified model was discussed in this form first by Walther Heitler in 1944 [71] and is thus commonly called the Heitler model, he cited Carlson and Oppenheimer [41], along Bhabha and himself [31], to have laid the groundwork for it independently in 1936. Such an electromagnetic EAS can be seen on the left side of Figure 2.7.

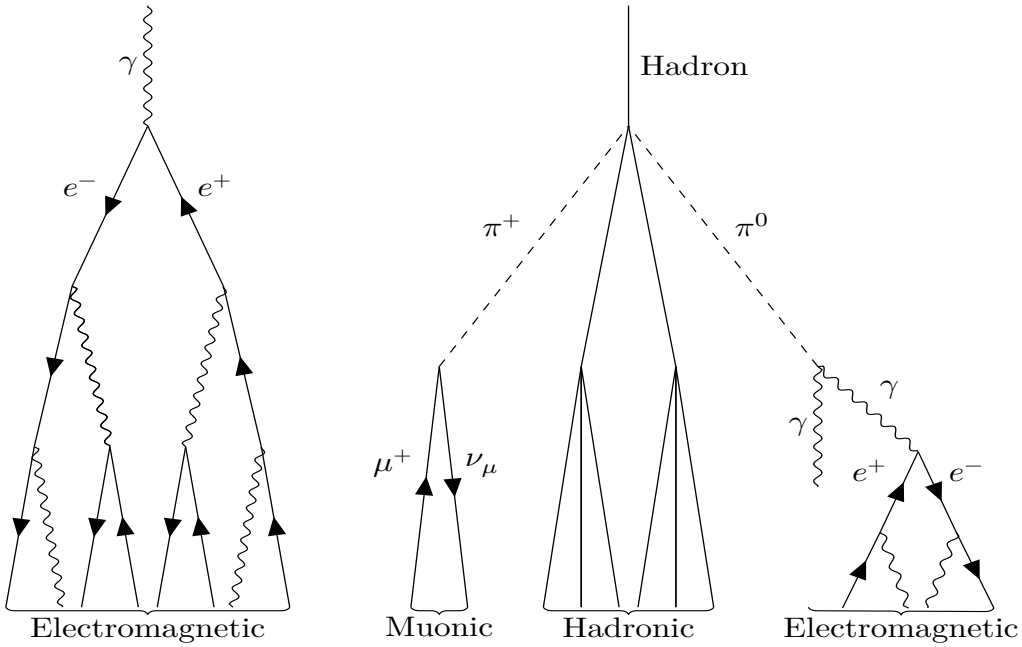

Figure 2.7: Schematic view of an electromagnetic EAS following the Heitler model (left) and a hadronic EAS (right). Atoms needed for some of the depicted processes are not shown. For the hadronically induced EAS, muonic and electromagnetic components mediated through a π^+ and π^0 are shown examplary for multiple possible mesons.

Photons are not the only particles that can induce such a shower. While electrons and positrons can induce a virtually indiscriminate electromagnetic cascade that only varies from those induced by photons by the type of the first interaction, bremsstrahlung or pair-production, charged cosmic rays behave vastly differently. As these hadronic particles interact via the strong force, they can induce a cascade of multiple strongly interacting particles upon interacting with an atmospheric nucleus. Following Heitler's reasoning, James Matthews introduced a simplified model for a hadronic EAS induced by a primary proton, the Heitler-Matthews model [98]. The proton is, in the first step, converted into the lightest mesons, pions, splitting the energy equally among π^+, π^- and π^0 sub

cascades

$$p\,(+N) \rightarrow \pi^{\pm} + \pi^{0} + \ldots . \tag{2.13}$$

Charged pions of sufficient energy live long enough to interact again in subsequent strong processes until their interaction length becomes larger than their decay length, having them decay predominantly into muons and neutrinos. Neutral pions, on the other hand, decay directly, predominantly into photons

$$\pi^{0} \rightarrow 2\gamma. \tag{2.14}$$

These photons carry enough energy to induce an electromagnetic cascade. Consequently, the EAS induced by cosmic rays and photons are hardly distinguishable. Thus, cosmic rays are the primary background class when observing showers induced by photons. A hadronic EAS following the Heitler-Metthews model is displayed on the right side of Figure 2.7.

While the discussed Heitler-Metthews model only considers primary protons, similar approaches exist for heavier nuclei [103], again only considering pions. While pions are the lightest hadrons and should thus be the most abundant part of a hadronically induced EAS, the occasional production of heavier particles is possible. Kaons, for example, were first observed in EAS [118], as were, in fact, positrons [16], muons [122], and pions [90]. Today, accounting for these and more different particles, interaction models, and lateral shower development, Monte Carlo methods are used to simulate the EAS. The most prominent example is `CORSIKA` [69], a software package first released in 1989 and actively used by current VHE experiments as well as CTAO.

The charged particles in both EAS types are, although still slower than the speed of light in vacuum c_0, energetic enough to travel with a speed above the local speed of light $c_n = c_0/n$ in the dielectric atmosphere with a refractive index n. When passing through the medium above that speed, the dipoles in that medium can no longer arrange symmetrically around the moving particle. Electromagnetic radiation emitted from these dipoles can thus interfere constructively, forming a cone with an opening angle

$$\cos\left(\theta_{\mathrm{Ch}}\right) = \frac{1}{n\beta} \tag{2.15}$$

at relative speed $\beta = v/c$. This is called the Cherenkov effect [43, 59]. As the refractive index of a medium increases with pressure, the refractive index of Earth's atmosphere decreases with height above sea level. While the cone formed by a particle moving at $\beta \rightarrow 1$ has an opening angle of about 1.35 deg at sea level, the angle was significantly smaller at the start of the cascade. Hence, the radiation from a single particle is strongly focused. Nevertheless, cones of light from each of the many charged particles in the shower reach the ground, leaving an extended footprint of the original EAS. This whole process is, however, extremely short-lived. The flash of light produced by an EAS typically lasts between 20 and 30 ns [7] and is consequently too fast for the human eye, even though the emission peaks in blue and near UV wavelengths.

2.5 Detection of VHE Gamma Rays with Imaging Air Cherenkov Telescopes

To briefly recap the previous chapters, VHE photons from the most extreme sources in the universe reach Earth alongside a background of charged cosmic rays and interact with the atmosphere,

creating EAS and thus leaving an indirect trace of their origin that can be detected at ground level. Detecting these traces is the observation principle of Imaging Air Cherenkov Telescopes (IACT). On a low level, the idea is simple: mirrors focus the Cherenkov light emitted in the EAS onto a camera consisting of several hundred PhotoMultiplier Tubes (PMTs) that convert the photon signal into a voltage time series [76]. This time series for each pixel is then digitized, calibrated, and, after some noise suppression, a camera image can be further analyzed to infer the properties of the incidental particle. As long as the telescope lies within the Cherenkov footprint, the shower and the primary particle can be observed. This detection principle is comparably easy to realize. Detector-wise, the main challenge is the development of a camera that is optimized to the wavelengths of the Cherenkov light and can detect and resolve short flashes on time scales in the order of ten nanoseconds. Additionally, the high event rates require a trigger system and readout electronics that can handle the steady stream of data [125].

Since the lateral development of EAS guarantees footprints with a diameter in the order of 100 m [75], an immense volume can easily be instrumentalized, outsizing a satellite experiment by several orders of magnitude. This enables IACTs to reach energies where it is otherwise infeasible to construct a space-bound telescope due to size and weight limits. However, there are downsides to this technique. The indirect nature of the measurement complicates the reconstruction of the primary particle and the steady stream of background events by hadronic EAS severely outweighs the wanted signal counts. Using the all-nucleon spectrum from [123, (29.2)] regardless of breaks in the spectrum at PeV and EeV energies, one finds an energy-integrated flux of

$$\int_{0.1\,\mathrm{TeV}}^{\infty} I_{\mathrm{N}}(E)\,\mathrm{d}E \approx 4.22 \times 10^{-4}\,\mathrm{cm}^{-2}\,\mathrm{s}^{-1}\,\mathrm{sr}^{-1}. \tag{2.16}$$

Using a telescope with a field of view of 4.5 deg or approximately 0.005 sr to observe the Crab Nebula, recalling (2.2), the ratio R between signal and background is

$$R \approx \frac{1}{4433} \tag{2.17}$$

even though the Crab Nebula is one of the brightest known sources of VHE gamma rays.

Regardless of these challenges, the successful history of IACT experiments started with the Whipple telescope and its 10 m diameter mirror, located at the Mount Hopkins Observatory, today's Fred Lawrence Whipple Observatory, in Southern Arizona, USA [132]. During its operation from 1986, it received several upgrades until decommissioned in 2013. Next in line was the High-Energy-Gamma-Ray-Astronomy (HEGRA) installation, in service between 1987 and 2002 at the Observatorio del Roque de los Muchachos (ORM) on the Canary Island of La-Palma, Spain. The HEGRA experiment combined multiple detection principles [58]:

- Scintillation counters to detect the particles of an EAS that reach the ground;
- AIRshower Observation By angle Integrating Cherenkov Counters (AIROBICC), simple installations of single PMTs over a large area to measure whole footprints of EAS;
- Geiger towers to reconstruct and identify electron and muon tracks;
- a stereoscopic system of five IACTs in the final configuration.

In addition to these HEGRA installations, two additional experiments were on the site. The CRT project tested time-projection drift chambers for the detection of EAS [29]. At the same time, the CLUE collaboration developed Cherenkov telescopes optimized for UV wavelengths that used gas-proportional wire chambers as detectors [12].

The current generation of IACT consists of three installations:

- The High Energy Stereoscopic System H.E.S.S., an array of five IACTs, four with mirror diameters of 12 m and one with 28 m in the Khomas region, Namibia. The four smaller H.E.S.S. telescopes started operation between 2002 and 2004 [78], and the larger telescope started data-taking in 2012 [25].
- The Major Atmospheric Gamma Imaging Cherenkov Telescopes (MAGIC), the successor to HEGRA at the ORM, a stereoscopic system of two 17 m diameter IACTs built in 2004 and 2009 respectively, with major upgrades between 2011 and 2012 [11].
- The Very Energetic Radiation Imaging Telescope Array System (VERITAS), the successor to the Whipple telescope at the Fred Lawrence Whipple Observatory, four 12 m IACTs built between 2003 and 2007 [79]. It received multiple upgrades during operation, including the complete relocation of a telescope for improved sensitivity [113].

A recent addition to the list of IACT experiments is the Major Atmospheric Cerenkov Experiment Telescope (MACE), one 21 m diameter telescope in the Ladakh region, India [134]. While these experiments are probably the most successful, there were many precursors and other IACT experiments. One notable example is the First G-APD Cherenkov Telescope (FACT), an IACT of about 4 m diameter, designed to be a pathfinder for the use of silicon photomultipliers instead of PMTs which saw first light in 2011 [15]. A comprehensive history can be found in [101].

Today, VHE gamma-ray astronomy using IACT experiments is at the break towards a new generation of experiments. As the current generation of telescopes is approaching the later stages of their lifecycles, new experiments are planned, building on the successful operation of the aforementioned installations installations. It has become evident over the past decades that the construction of stereoscopic experiments or whole arrays of IACTs severely outperforms monoscopic observations. Naturally, future concepts focus on this approach. The efforts of broad parts of the IACT community culminated in the design of the Cherenkov Telescope Array Observatory (CTAO), two installations of tens of IACTs at two sites, once again at the ORM and in the Atacama desert in Chile. The CTAO installations will probably be the major instrument for VHE gamma-ray astronomy using ground-based IACTs for the next decades. The following chapter will introduce CTAO in greater detail.

The Cherenkov Telescope Array Observatory and the Large-Sized Telescope Prototype LST-1

3

As introduced in the previous chapters, the Cherenkov Telescope Array Observatory (CTAO) will be the next-generation installation for ground-based VHE gamma-ray astronomy. Designed as an open, proposal-driven observatory at two sites, the ORM at La Palma, Spain, and the Paranal Observatory in the Atacama Desert, Chile, CTAO will be able to observe both the northern and southern sky. The currently funded Alpha Configuration layouts [137] of both array sites are shown in Figure 3.1. Combined with optimal observation environments at the selected sides, three different telescope sizes will enable CTAO to observe gamma rays between 20 GeV and 300 TeV.

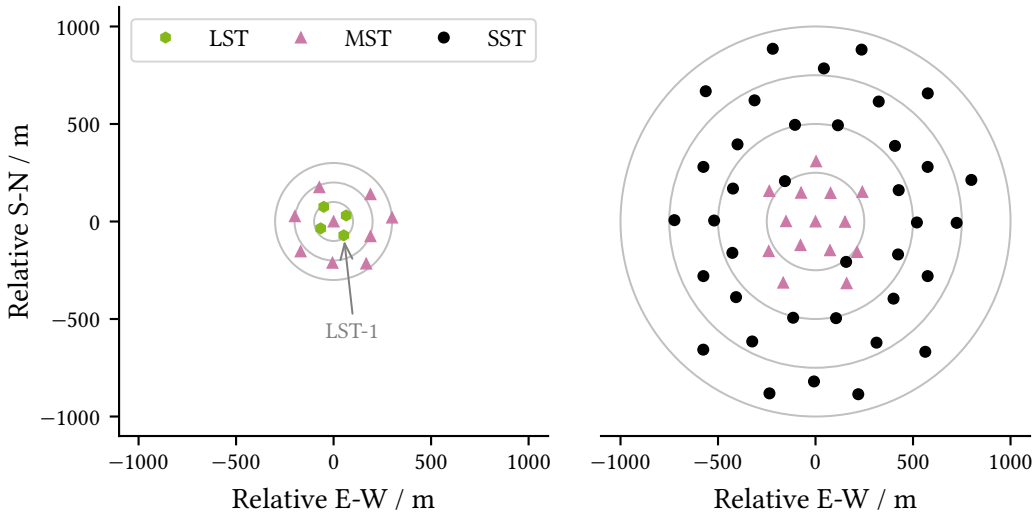

Figure 3.1: The layouts of the northern (left) and southern (right) CTAO arrays in their prod5 [30] Alpha Configuration [137]. Gray circles indicate radii of [100, 200, 300] m (left) and [250, 500, 750, 1000] m (right). LST-1, the telescope used in this thesis, is highlighted.

3.1 CTAO Telescope Types

Large-Sized Telescopes (LSTs) will provide the northern site at the ORM with instruments optimized to observe gamma rays between 20 and 150 GeV. In the north, the LST prototype, LST-1, is nearing the end of its commissioning phase at the ORM and the construction of the second to forth LST has started. While the southern Paranal site will not receive LSTs according to its Alpha Configuration, foundations for four LSTs will be laid down to ease later upgrade of the array.

With a mirror diameter of 23 m and a focal length of 28 m, LSTs will have a field of view of 4.5 deg observed by an 1855 PMT camera. Amongst further requirements, see [47], they are required to reposition to any position in at most 20 s to be able to observe transient events. An image of LST-1 can be seen in Figure 3.2. As it is currently the only telescope planned for CTAO already taking data, the remainder of this work will focus on it.

The Medium-Sized Telescopes (MSTs) with their 12 m diameter mirrors and an 1758 (FlashCam, Paranal) or 1855 PMT camera (NectarCAM, ORM) will be optimized for energies between 150 GeV and 5 TeV. With the camera mounted at a focal length of 16 m from the mirror, these telescopes have a field of view greater than 7 deg [35]. MSTs will be built at both sites, nine at the ORM and 14 at the Paranal observatory. A prototype was operated in Berlin between 2012 and 2020.

Optimized to the highest energies between 5 and 300 TeV, 37 Small-Sized Telescopes (SSTs) will push current boundaries for IACT experiments at the southern array site. Contrary to the single mirror designs of all previously described IACTs, SSTs will be of a double mirror modified Schwarzschild-Couder type [129]. Their 4.3 and 1.8 m diameter primary and secondary mirror and a 2.15 m focal length allow for a 8.8 deg field of view, the largest of all three telescope types [63]. Its 2048 pixel camera builds upon the SiPM technique already used with FACT. Thus, the SSTs will be the only CTAO telescopes with a camera that does not rely on PMTs [51].

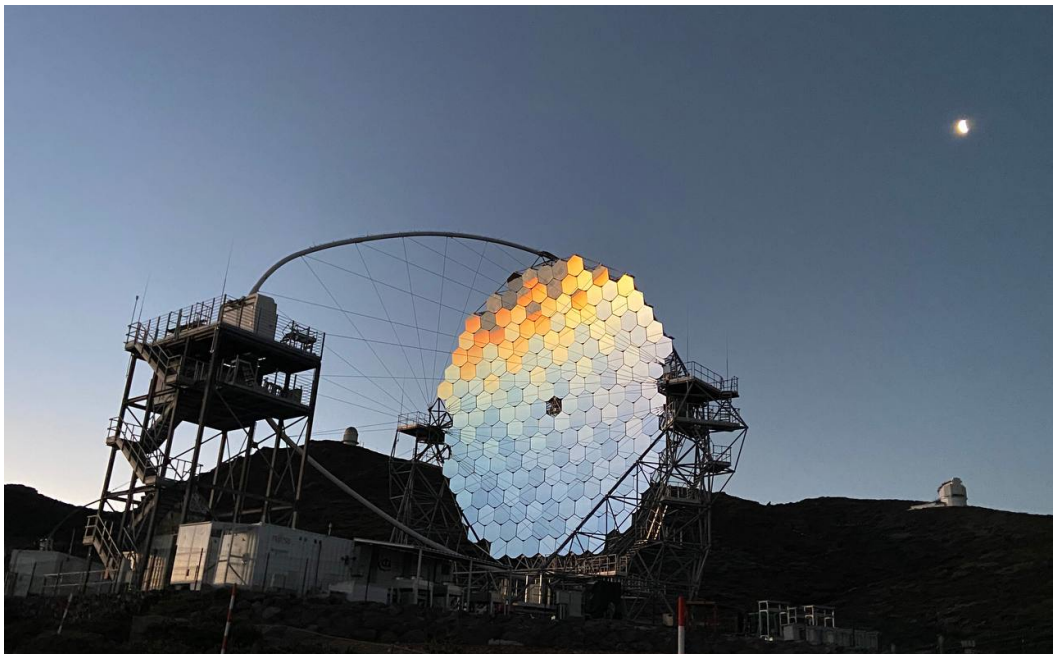

Figure 3.2: Photography of the LST prototype LST-1 at the ORM. The Nordic Optical Telescope's (left) and the Telescopio Nazionale Galileo's (right) domes can be seen on the hill in the background. Image: T. Gradetzke (TU Dortmund University).

3.2 Mode of LST-1 Observations and Significance Estimation

Observations with IACTs, including those used in this thesis, are often taken in the so-called wobble mode [36]. In this observation mode, an IACT does not point at the actual known or assumed source position but rather at some slight offset, the wobble offset, beside it. This allows the telescope to observe the source in an on-region and, simultaneously, one or more off-regions for background estimations at the same wobble offset from the camera center. As the response of the whole system can, in first-order approximation, be assumed to be radially symmetric around the camera center, wobble mode observations allow for on- and off-measurements to be taken with the same response. Additionally, the need for dedicated off-region measurements disappears, maximizing observation time. To account for further systematics, the pointing position around a source is changed between observation intervals, aimed to be 20 min runs for LST-1. The wobble mode principle is sketched in Figure 3.3.

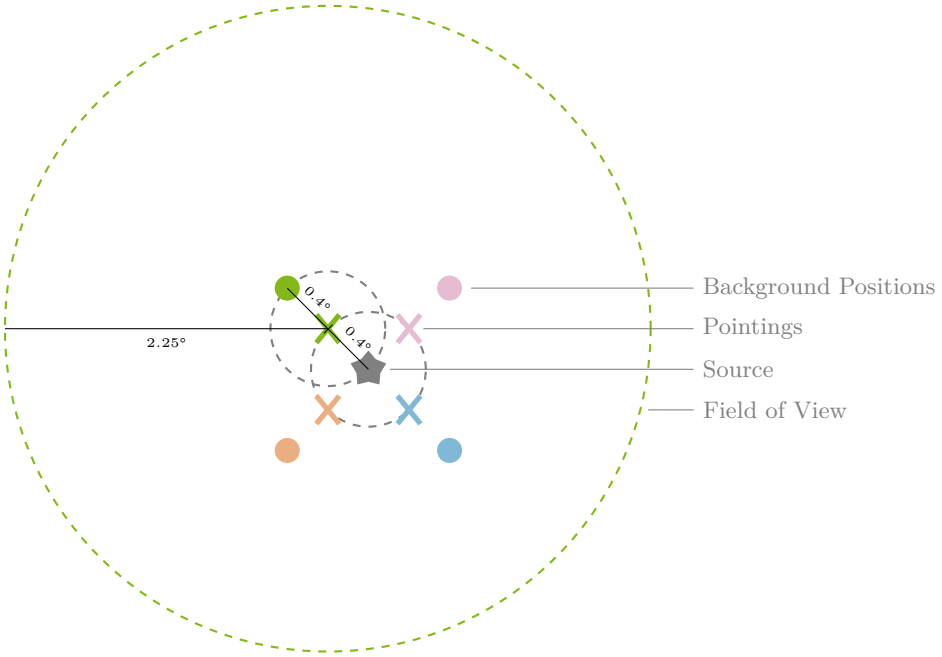

Figure 3.3: Sketch of wobble mode observations. Instead of pointing directly onto the source, the telescope points some offset, 0.4 deg for LST-1, besides it. This way, background measurements can be taken at the same offset simultaneously. Around a source, multiple wobble positions are possible, four used with LST-1 Crab Nebula observations are included in the sketch. Additionally, multiple background positions can be chosen at the same time on the circle around the pointing. In this thesis, only those mirroring the source are used and thus included in the figure.

In case the on- and off-measurements yield N_{on} and N_{off} counts and α is the ratio between on- and off-region size or measurement time, the significance S in units of standard deviation σ of the

observation can be estimated according to [93] as

$$S = \sqrt{2}\left\{N_{\text{on}} \ln\left[\frac{1+\alpha}{\alpha}\left(\frac{N_{\text{on}}}{N_{\text{on}}+N_{\text{off}}}\right)\right] + N_{\text{off}} \ln\left[(1+\alpha)\left(\frac{N_{\text{off}}}{N_{\text{on}}+N_{\text{off}}}\right)\right]\right\}^{\frac{1}{2}}. \tag{3.1}$$

Like particle physics, VHE gamma-ray astronomy considers a source detected if S exceeds 5. A value $S \in [3, 5)$ is considered a strong hint for a source.

3.3 Data Taking and Calibration for LST-1

Events observed by LST-1 can roughly be divided into calibration and actual physical events. For calibration purposes, two different types of events are generated [125]:

- Pedestal events, where the camera is periodically triggered at times when no physical event is measured to estimate the fluctuations of the Night Sky Background (NSB)
- Flat-field events, where the camera is artificially triggered while illuminated by a calibrated light pulse. These events allow LST-1 to study differences in the arrival times and gains of PMTs.

Contrary to these calibration events, the trigger system for physical events utilize the fact that Cherenkov flashes from EAS arrive compactly and coincidently at the camera. This is not the case for random fluctuation of the NSB. Physical events are thus triggered based on temporal and spatial coincidence as explained in [125]: The 1855 PMTs, each resembling one pixel of LST-1s camera, are combined into groups of 7 pixel and connected to one of the 265 Front-End Boards (FEBs), read out at 1 GHz. For cameras built for LSTs, the signal of each PMT is analogously summed for each FEB, resulting in a Level 0 signal. This signal is distributed to neighboring FEBs. Whenever a combination of neighboring FEBs rises above a predefined trigger threshold, the Level 1 system triggers the readout and digitalization of all camera pixels [124]. As there is currently only one operating LST, LST-1, Level 1 is the highest trigger level for LST-1 mono observation. However, stereoscopic observations of an array allow for higher trigger levels. The Level 2 Hardware Stereo Trigger combines the Level 1 signal of multiple telescopes and only triggers camera readout if two or more telescopes coincidently detect a signal. As coincidental detection of a NSB fluctuation by multiple telescopes is highly unlikely, weaker signals can be triggered as NSB events primarily obscure the low energies. Since a Level 1 trigger aiming to reduce NSB events struggles in discriminating between actual low-energy gamma-ray events and NSB fluctuations, the Level 2 trigger will lower the energy threshold of the array. Such a Hardware Stereo Trigger is tested for joined observations between LST-1 and the neighboring MAGIC telescopes. To reduce the amount of data collected, a final Level 3 Software Array Trigger will allow only that data to be written from memory to disc that fulfills further conditions.

In any case, the analog PMT-signals must be digitized after triggering. For LST cameras, this is handled by fourth-generation Domino Ring Sampler (DRS4) chips [117]. As the DRS4 chips provide switched capacitor arrays that store the signal of each PMT in an analog fashion, the signal digitalization allows for some delay to allow for the coincidence triggers to detect a signal. Upon triggering, the DRS4 chips digitize the stored signal into a 40-sample waveform spanning 40 ns

in two gain channels first to memory and later written to disc. Combining these uncalibrated waveforms from one event for all pixels of one telescope's camera with meta-data such as timestamps provides the lowest data level for CTAO, R0. These raw waveforms are further calibrated to account for thermal noise and slight differences in the PMTs by subtracting a pedestal rate acquired from the above calibration measurements and correcting timing differences in the PMTs. As a last step, the voltage waveforms are converted to units of photon equivalents. This result is called R1 data. A measured waveform at R0 and R1 with intermediate steps is shown in Figure 3.4. As a last step before the low-level analysis, waveforms of pixels that do not include a peak and are, besides thermal or NSB noise, flat are discarded, resulting in a conservative but immense data volume reduction. The result of this step is designated DL0.

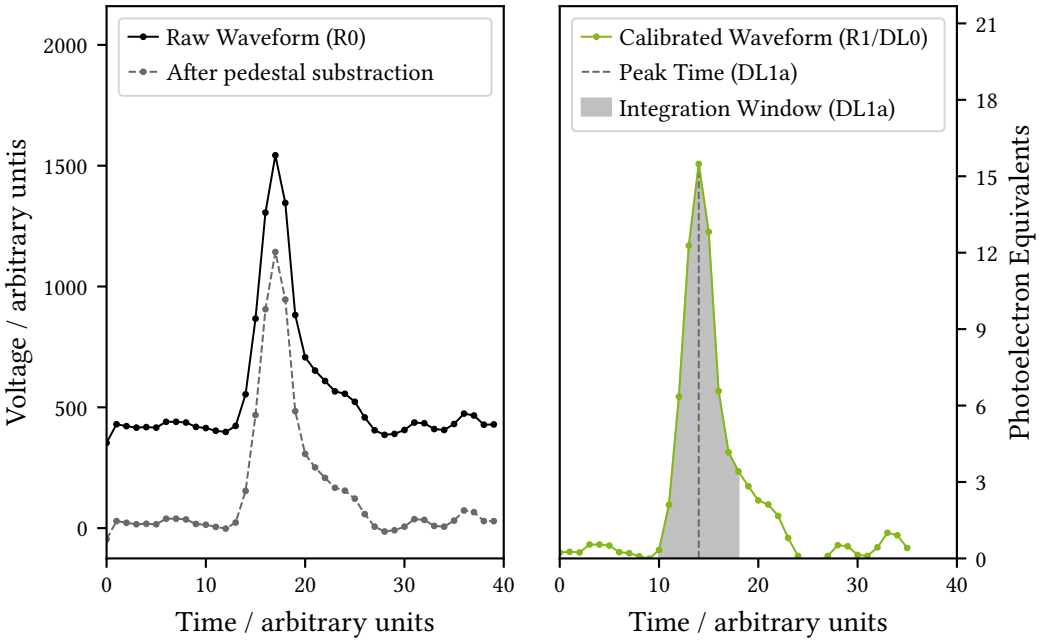

Figure 3.4: Measured waveform taken from NGC 1275 observations at R0 level with intermediate calibration steps (left) and R1 level with intermediate steps to DL1a (right). As the displayed waveform clearly shows a Cherenkov signal, it is not subject to the data volume reduction to DL0. Thus, this waveform is also present in the DL0 file. The peak time is extracted, and the signal is integrated around it to process the waveform from DL0 to DL1a.

3.4 Low-Level Analysis

After reaching DL0, the low-level analysis starts. This analysis is currently implemented in the Python library `lstchain` [95], relying heavily on `ctapipe` [94] and `pyirf` (see, e.g., Dominik, Linhoff and Sitarek [53]). The goal of the low-level analysis chain is to produce science-ready data, labeled DL3. As CTAO is planned as an open, community, and proposal-driven observatory, one of the most relevant use cases is the delivery of data products from requested observations to scientists unfamiliar with the specialties of CTAO. A considerable part of this domain knowledge is concentrated in the low-level analysis chain. The production of science-ready data thus relieves scientists without specific background from further training. Multiple processing steps are needed towards reaching DL3.

DL1a and DL1b: Parametrization of Camera Images

As a first step, the DL0 waveforms for each surviving pixel are converted into two images, one for deposited charge and one for arrival time. To extract these images, a window around the time-series maximum is defined in which the charge is summed for the charge image as was shown in Figure 3.4. The peak times are then used for the arrival time image. While different methods exist to define the integration window, the resulting images still contain noise. The process of excluding pixels that do not contain information related to the observed EAS is called cleaning. Again, different methods for image cleaning exist; the most commonly used is the so-called tailcuts cleaning approach, which is also used as a first pass method in this work. Tailcuts cleaning provides three free parameters, uses only the charge image, and does not consider timing information. In a first pass, pixels above a threshold T_1 are selected if they have at least N neighboring pixels also satisfying this condition. The second pass then adds all pixels above a second threshold $T_2 < T_1$ that have at least one neighboring pixel from the first pass. Information from pixels that are not selected by these two passes is discarded in the original form of tailcuts cleaning. Modern experiments such as LST-1 and, thus, this thesis, include further information from, e.g., the arrival times, in a second pass. The results of applying image-extraction and cleaning to DL0 data can be seen in Figure 3.5. These two cleaned images provide the so-called DL1a data per triggered event and telescope.

While advanced machine learning approaches like deep learning can start from DL1a or lower, the common and successfully applied more classical machine learning algorithms such as random forests or boosted decision trees need further parametrized versions of the images. These parameters are extracted during processing to DL1b. The most classical and still successfully applied approach is the so-called Hillas parametrization [74], building upon a principal component analysis of the cleaned charge image around the weighted mean of all pixels, the center of gravity. The square roots of the two principal component eigenvalues, thus the standard deviations, are designated length and width of the image; both are included in Figure 3.5. The main axis of the EAS is thought to be given by the length component. The orientation of this axis in the camera is a strong proxy for the source of the inducing particle. Together with the sum and weighted average of all pixels, a proxy on the energy of the inducing particle, these parameters were already used by the Whipple experiment. To facilitate better analyses, higher order moments of the charge distribution in the image and a linear fit of the timing information are nowadays added to refine the source reconstruction further. Parameters summing the charge deposition in the outmost camera

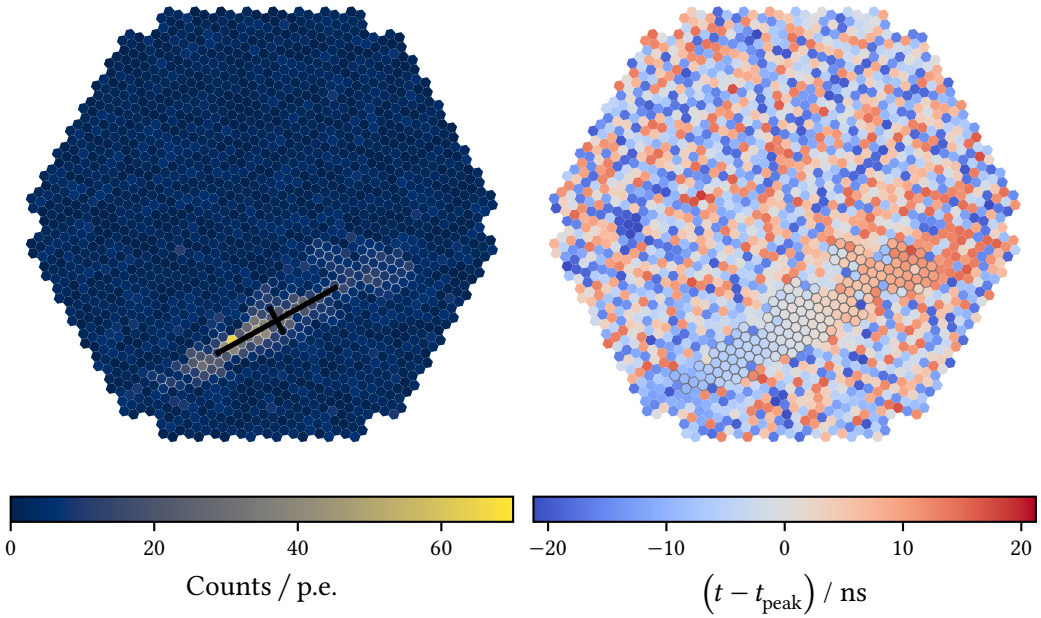

Figure 3.5: Extracted DL1a charge (left) and arrival time image (right) with highlighted cleaning mask (white/gray pixel boundaries) for the same event whose brightest pixel was used in Figure 3.4. The charge image also displays the Hillas parameters length and width as in the center of gravity intersecting black lines computed from the pixels inside the cleaning mask during the processing step towards DL1b.

pixels can give a proxy on how complete the image is. In contrast, counts of separated islands of charge deposition inside the image help to distinguish between electromagnetic and hadronic EAS, as the latter tends to produce multiple sub-showers, each producing one island of charge in the image. While this list of parameters is not exhaustive, and new parameters could still increase the performance of CTAO, the collection of all image parameters again for each triggered event and telescope is designated DL1b and fed to machine learning algorithms.

DL2: Estimating Primary Particle Properties and the First Application of Simulations

The machine learning algorithms use the DL1b parameters to estimate the three important quantities for further analysis:

- The type of the primary particle that induced the EAS, given by a classifier score typically called gammaness with a value around 1 indicating a high probability for a gamma-ray event.
- The energy $\hat{E}$ of the primary particle, the result of a regression model.
- The two-dimensional source position $(\hat{\alpha}, \hat{\delta})$, again at least partially the result of a regression.

For the latter one, multiple methods exist. The conceptionally most straightforward approach

would be the estimation of a source position $(\Delta x, \Delta y)$ relative to the center of gravity in the telescope's camera, needing two regression models. As binary classification is typically more manageable than a regression, the disp-method splits this into one regression and one classification task. Here, the regressor estimates the distance between the center of gravity and the projected source position in the camera, hence the norm $\|(\Delta x, \Delta y)\|_2$, by assuming it to lie on the projected shower axis. The classifier then predicts on which side of the center of gravity, with respect to the dominating primary component, the source lies. For stereoscopic systems such as H.E.S.S. and, once more progressed, CTAO, purely geometric approaches projecting the respective image of each telescope that observed an EAS into a common frame are most promising [92].

The machine learning models need to be trained before application. For this and further parts of the analysis chains, exhaustive simulations of EAS produced by hadrons and photons are conducted for CTAO; the latter ones are further separated into point-like photons, where the simulated photon source is fixed at one offset to the field-of-view, similar for all simulated events in the production, and diffuse photons, where the sources are randomly distributed over the whole simulated sky. Additionally, simulations for electrons and muons are also computed. As mentioned, EAS simulations for CTAO are produced by the `CORSIKA` software. The tracing of the Cherenkov photons throughout the telescope systems up to the generation of datasets that resemble real data is, in turn, handled by `sim_telarray` [28] and then processed using the same analysis chain as real events.

The production of these simulation datasets is an extremely time- and resource-consuming task, and a complete "all-sky" production spanning the whole field of view observable by any of the CTAO sites with sufficient statistics is infeasible. To circumvent this, the strategy deployed for LST-1 intends to limit the total production of hadron and photon simulations to declination lines with multiple telescope pointings along the trajectory, called training nodes. The DL1b datasets obtained from these simulations are used to train the mentioned machine learning models, and the analyzer then uses those models trained on the nearest declination line to the respective source. To provide further independent pointings for testing and later IRF computation, a grid of testing nodes inside the observational boundaries of the site is simulated with fewer statistics and further processed with the models trained on each declination line. The current shape of this testing node grid results from a living process. While it started as a regular grid, as can still be imagined from the black crosses in the right-hand side graphic of Figure 3.6, it was extended due to observational needs afterward, resulting in the current shape. The whole simulation strategy alongside the trajectories of Crab Nebula and NGC 1275 is shown in Figure 3.6.

After estimating the initially mentioned quantities alongside an estimated arrival time $\hat{t}$ that is, given high precision clocks, quite well known, the information is again most present in a table where each row represents a triggered event and telescope. Thus, stereoscopic systems must combine this information for EAS observed by multiple telescopes into an array-level estimation. To do so, the most straightforward approaches utilize (weighted) means or, more sophisticated, compute new stereoscopic parameters like, e.g., mean scaled cuts [49] that allow for a better distinction between photon and hadron induced EAS or, perspectively, further machine learning models. For LST-1 observations and thus this work, combining stereoscopic information is irrelevant due to the lack of a stereoscopic system. Nevertheless, the resulting list of estimated gammaness, energy,

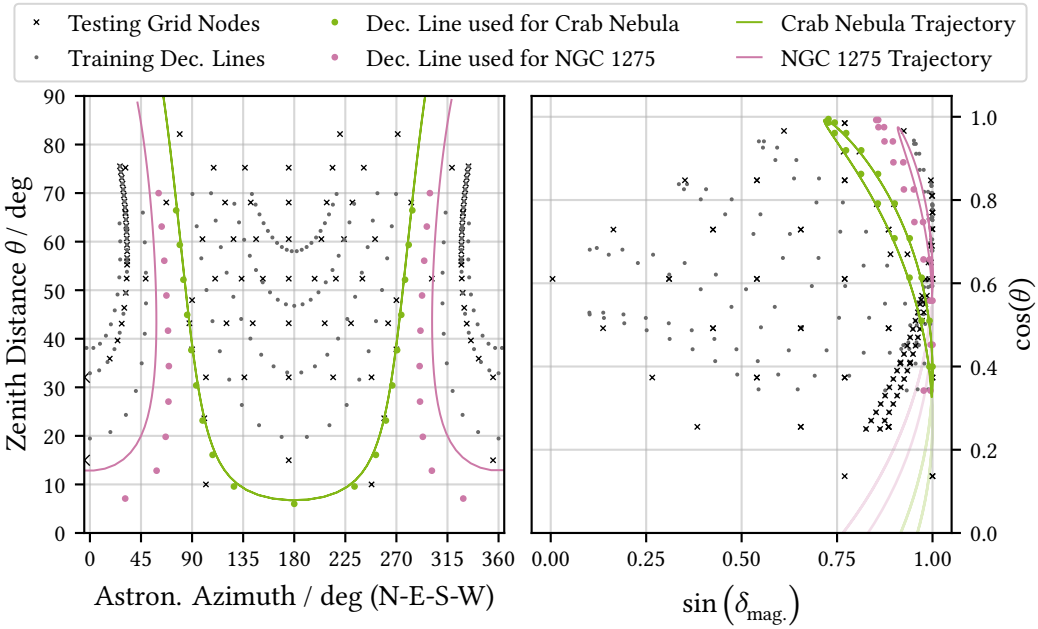

Figure 3.6: Illustration of the declination lines used as training nodes and the testing nodes grid points alongside the trajectories of Crab Nebula and NGC 1275 as seen at the ORM. Figures in astronomical azimuth and zenith distance θ (left) alongside a $\sin(\delta_{\text{mag.}})$ and $\cos(\theta)$ representation (right) with $\delta_{\text{mag.}}$ being the angle between the magnetic field and the pointing to the respective position on the sky. The latter representation is a potential candidate for a later interpolation grid.

source position, and arrival time per event and array (or mono telescope) is a DL2 data product.

DL3: Science Ready Datasets and the Second Application of Simulations

The DL2 event lists are almost science-ready. However, some tasks remain until they can be used for high-level analysis.

1. The event lists still contain entries from hadron induced EAS.
2. The event lists only contain estimated quantities which do not perfectly relate to the actual properties of the inducing particle.
3. There is no handle to estimate how many events the telescope or array missed due to, e.g., corner-clipping events or insufficient Cherenkov light yield.

To resolve the first issue, only those events from the DL2 files are selected for further processing that survive some cuts on the gamma-hadron classification score, commonly computed from simulations to yield a predefined percentile of surviving gamma-ray events in a specified bin of estimated energy. These events are regarded as signal events. Yet, there will always be a remaining amount of hadron events in this selection. Instrument Response Functions (IRFs) are supplied for the remaining tasks. These IRFs are produced by comparing the true and reconstructed energy

and source position as well as the amount of simulated and successfully reconstructed events for the aforementioned testing node simulations using the same models that were applied for the DL2 lists. While the exact nature and computation of IRFs for a specific measurement and the background separation is described in the following chapter 4, the collection of selected DL2 events and IRFs is called DL3 data. Up to DL3, all analysis steps and the used data structures were, albeit implemented in open source software, CTAO internal. However, the format of DL3 files produced by CTAO results from an IACT community effort to provide a standard format for VHE gamma-ray astronomy [109]. Defining this common DL3 format enabled the first joint analysis of Crab Nebula observations taken by *Fermi*-LAT, MAGIC, VERITAS, FACT, and H.E.S.S. [108].

Interpolation of Instrument Response Functions and High-Level Analysis

4

To be able to produce high-level data products, including spectral and spatial features, knowledge of the instrument response to an incoming signal is needed. As stated in the previous chapter, this information is supplied by Instrument Response Functions (IRFs) computed from simulated events. However, they depend on observational conditions such as telescope pointing and atmospheric conditions. The production of a matching IRF for each distinct IACT observation would thus require specialized simulations and is a highly time-consuming task. This process is infeasible when time and resources are constrained, e.g., in observations of transient events. In these cases, IRF interpolation may offer a solution.

Regardless of how an IRF was computed, the DL3-file containing it alongside observed events is the starting point for further high-level analysis. This chapter will thus introduce the concept of IRFs and the problem they are central to, the scheme to interpolate IRFs in short timescale settings introduced by this thesis, and a first assessment of its performance. Lastly, this chapter will also introduce the high-level analysis chain used to derive the physical results presented in the two following chapters.

4.1 Introduction into IRFs

DL2 files only contain estimated or reconstructed quantities for energy $\hat{E}$, source position in ICRS coordinates as right ascension and declination $(\hat{\alpha}, \hat{\delta})$ and arrival time $\hat{t}$ of the observed signals. Deviations from the true values E, α, δ, and t are inevitable due to the indirect measurement process and the employed reconstruction algorithms, and some events might not be triggered at all or might not have survived the reconstruction process. Following the reasoning in Dominik, Linhoff, and Sitarek [53], the relation between measured and actual properties is provided through a convolution with the IRF. While the time reconstruction is, for most applications, sufficiently correct and thus $\hat{t} = t$ holds in most settings, the observed distribution of events $g(\hat{E}, \hat{\alpha}, \hat{\delta}, t)$ is related to the true gamma-ray signal arriving at Earth $f(E, \alpha, \delta, t)$ and a background $b(\hat{E}, \hat{\alpha}, \hat{\delta}, t)$ by the Fredholm integral

$$\underbrace{g(\hat{E}, \hat{\alpha}, \hat{\delta}, t)}_{\text{Observed distribution}} = \iiint \overbrace{R(\hat{E}, \hat{\alpha}, \hat{\delta} \mid E, \alpha, \delta, t)}^{\text{Instrument Response}} \cdot \underbrace{f(E, \alpha, \delta, t)}_{\text{True gamma-ray signal}} \, \mathrm{d}E \, \mathrm{d}\Omega \, \mathrm{d}t + \overbrace{b(\hat{E}, \hat{\alpha}, \hat{\delta}, t)}^{\text{Background}} \tag{4.1}$$

with the solid angle differential $\mathrm{d}\Omega = \sin\delta \, \mathrm{d}\alpha \, \mathrm{d}\delta$. The computation of the desired scientific result, either fully or partially spectrally-, spatial- and temporally-resolved gamma-ray flux $f(E, \alpha, \delta, t)$, thus requires solving an inverse problem.

As already stated in the previous chapter, the background separation is handled based on the classifier score estimated in the step from DL1b to DL2. A typical approach is to compute the cut value on the simulated events in a way that ensures the survival of a predefined percentage, e.g., 68 %, of the simulated gamma-ray events in each bin of $\hat{E}$. These gamma-hadron-cuts are then applied to the measured and reconstructed events. The tables are saved and supplied alongside the IRF. They are, however, not part of it.

After removing the background, the next step is to compute the IRF. In the general form introduced in (4.1) however, this IRF is a six-dimensional, time-dependent quantity $R(\hat{E}, \hat{\alpha}, \hat{\delta} \mid E, \alpha, \delta, t)$. The full estimation of R in this form is computationally infeasible; thus a factorization

$$R(\hat{E}, \hat{\alpha}, \hat{\delta} \mid E, \alpha, \delta, t) = \underbrace{A_{\text{eff}}(E, \alpha, \delta, t)}_{\text{Effective Area}} \cdot \overbrace{M(\hat{E} \mid E, \alpha, \delta, t)}^{\text{Energy Migration}} \cdot \underbrace{\text{PSF}(\hat{\alpha}, \hat{\delta} \mid E, \alpha, \delta, t)}_{\text{Point Spread Function}} \tag{4.2}$$

is commonly applied. These components, shown in Figure 4.1, are the

- Effective Area (A_{eff}): the combination of the experiment's sensitive area and the probability of a gamma ray with some true properties to be present in the data as a gamma ray after all analysis steps; this combination is chosen to ease the later computation of fluxes in per-area units as has been done in (2.2)

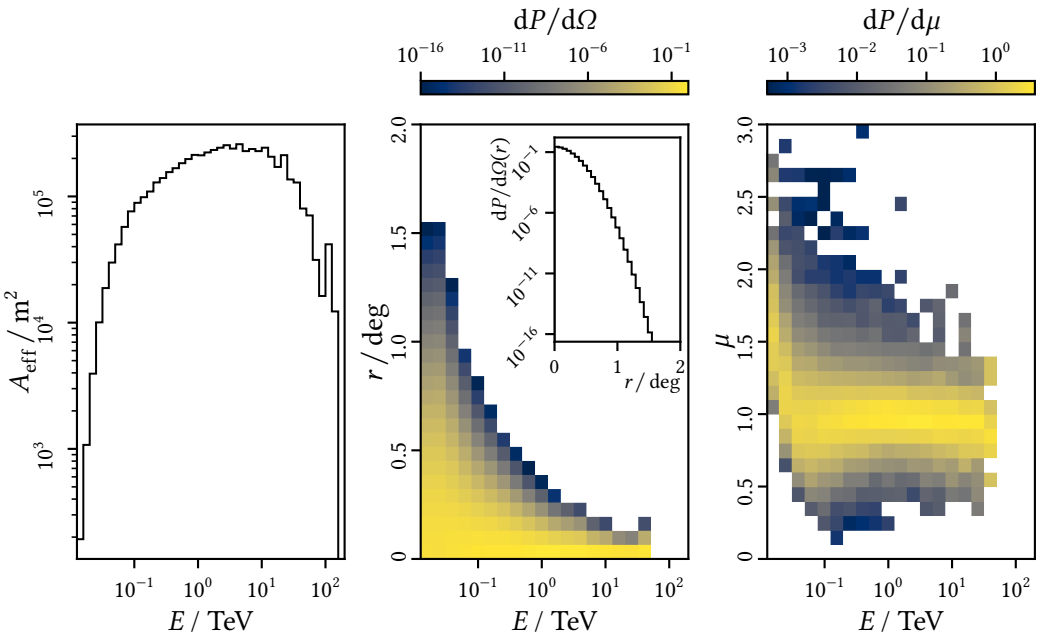

Figure 4.1: Illustration of the components of a full-enclosure IRF from the CTAO prod5 IRF release [44] from 50 h simulations of the planned northern LST subarray pointing at a zenith of $\theta = 20$ deg. The components include only events reconstructed at most 1 deg from the center of the telescope's field of view. Left: A_{eff}, center: PSF as the probability of finding an event in a solid angle $\mathrm{d}\Omega$ at an offset r, right: M_{EDisp} as the probability to find an event in a bin of $\mu = \hat{E}/E$. Inset axis: Closeup of the first PSF energy bin.

- Energy Migration (M) or Energy Dispersion matrix (M_{EDisp}): the conditional probability to reconstruct a gamma ray of some true properties with a certain energy $\hat{E}$; the migration gives the direct relation between E and $\hat{E}$ while the often used dispersion relates E with $\mu = \hat{E}/E$
- Point Spread Function (PSF): the conditional probability of reconstructing a gamma ray of some true properties at a certain source position $(\hat{\alpha}, \hat{\delta})$.

Combined, they form a so-called full-enclosure IRF that applies to all analysis use cases.

If only being interested in a spectrally and temporally resolved result, thus assuming a point source, the PSF can be exchanged for so-called RAD_MAX tables θ_{cut}. These tables then only contain $\hat{E}$-dependent radii defined as the θ_{eff}-percentile of the reconstructed events closest to the assumed source position. A common choice used is $\theta_{\mathrm{eff}} = 68\,\%$, a θ_{cut} table constructed for this value is shown in Figure 4.2. IRFs containing a θ_{cut} table are called point-like IRFs and are used for the remainder of this thesis.

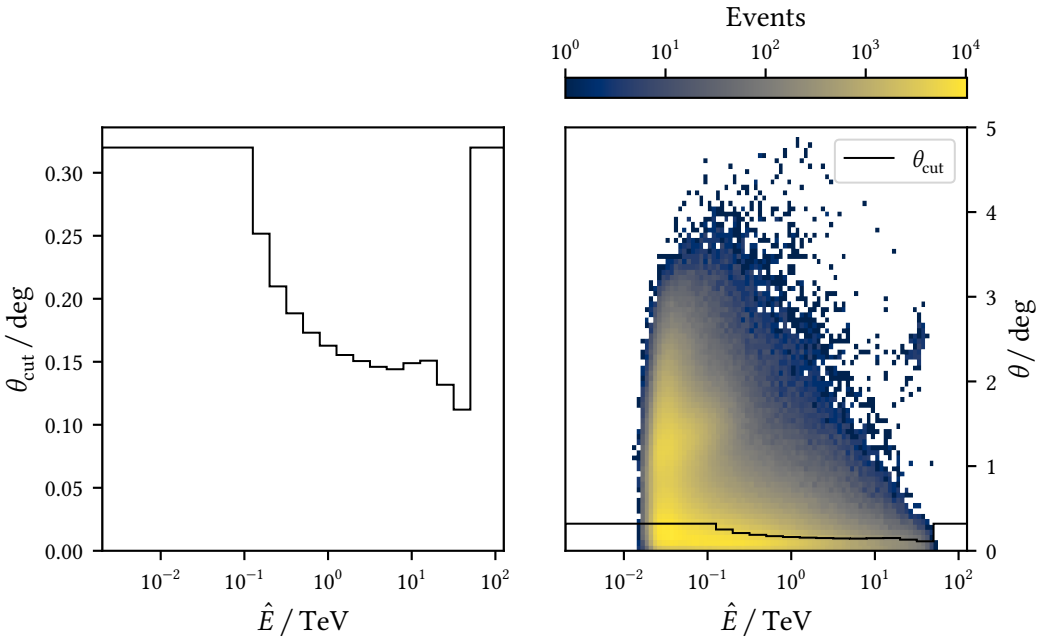

Figure 4.2: Illustration of the θ_{cut} component of a point-like IRF. Left: θ_{cut} values computed from simulated photon events to retain those 70 % events in each energy bin reconstructed closest to the simulated source. Right: Scatterplot of the angular distances θ between simulated and reconstructed source positions with respect to the reconstructed energies $\hat{E}$ for the same events used to compute the left-hand side θ_{cut} values, included as a black line. The high variance of θ values for low $\hat{E}$ values is partially built by disp ghostbusters where the disp classification, as introduced in section 3.4, estimated the wrong sign. These events were not considered when computing the θ_{cut} values. The θ_{cut} values were clipped to at most 0.32 deg, ensuring proper separation of the on- and off-region in wobble mode observations. This value was also the fill value for energy bins with insufficient statistics.

4.2 Dependence of IRFs on Observation Conditions

The performance of the telescope system that governs the IRFs is, as already stated above, neither constant with time nor independent of the observation conditions. Especially the latter ones severely influence the development of EAS through the atmosphere and thus change the footprint that is measured by an IACT. Consequently, EAS induced by identical particles appear differently in the telescope's camera based on the conditions in place during their formation. These differences, in turn, change the results of the low-level analysis and need to be accounted for through matching IRFs. Extended knowledge of the underlying effects is necessary to compute matching IRFs. Given that knowledge, the most optimal approach would be the simulation of a whole IRF accounting for the exact observation conditions. As this is time- and resource-consuming, estimation through inter- and extrapolation might offer a solution which will be further explored in the following chapters. The present chapter aims to explain some of the effects and derive suitable parameters for these estimation techniques.

Atmospheric Effects

Assuming a plane parallel atmosphere, thus a model ignoring the curvature of Earth and its atmosphere, shower particles emitted at a height h and at a zenith angle θ', assumed to coincide with the shower axis, thus $\theta' = \theta$, traverse a path length $l = h \cos^{-1}(\theta')$. Consequently, showers emitted under higher zenith angles traverse more atmosphere and are thus subject to stronger attenuation effects. This plane parallel assumption is typically considered viable up to $\theta = 70$ deg [27]. Higher incidental angles require spherical atmosphere models.

A vital quantity relevant for describing particle interactions and energy losses is the slant depth, the amount of traversed material by the shower. The slant depth can be derived by integrating the atmospheric profile $\rho_{\text{atm.}}$ over the traversed path length. This slant depth reads

$$X(h, \theta) = \int_{z_0}^{\infty} \rho_{\text{atm.}}(h)\, \mathrm{d}h \tag{4.3}$$

for a particle propagating from infinitiy to an observation height z_0 with $\theta = 0$ deg. Following the reasoning above, this has to be altered for particles with $\theta \neq 0$. In this case, the density profile has to be integrated along the traversed path length, thus

$$X(h, \theta) = \int_{z_0}^{\infty} \rho_{\text{atm.}}(h(l, \theta))\, \mathrm{d}l = \cos^{-1}\theta \int_{z_0}^{\infty} \rho_{\text{atm.}}(h)\, \mathrm{d}h = \frac{X(h, \theta = 0\,\text{deg})}{\cos\theta}. \tag{4.4}$$

From there on, [37] discussed multiple dependencies of the shower development with respect to the zenith angle by assuming a $\rho_{\text{atm.}}$ derived for an ideal isotherm gas, thus the most simple form of the barometric formula. Key points in this discussion are as follows:

- The Cherenkov light yield is in first-order approximation given by

$$Y(\theta) \approx \cos(\theta)\, Y(\theta = 0\,\text{deg}), \tag{4.5}$$

  thus, higher zenith angles result in decreased light yield.

- The intensity at the aperture is given through

$$I(\theta) \approx \exp\left(1 - \cos^{-1}\theta\right)^{\zeta} I(\theta = 0\,\mathrm{deg}) \tag{4.6}$$

  with $\zeta \leq 1$ being a measure of the atmospheric absorption. Thus, higher zenith angles result in decreased intensity. For small angles, the expression $\exp\left(1 - \cos^{-1}\theta\right)$ follows approximately $\cos(\theta)$.

- The shower-illuminated area derived from the Moliére radius and with it indirectly A_{eff} changes with

$$A_{\mathrm{M}}(\theta) \approx \cos^{-2}(\theta)\, A_{\mathrm{M}}(\theta = 0\,\mathrm{deg}), \tag{4.7}$$

  thus increased zenith angles result in larger footprints that, in turn, allow for a larger effective area to be instrumentized. With this, however, the photon density at the aperture decreases.

- The image size in the telescope's camera is, in first-order approximation, scaled by the angle ω at which the EAS core, whose extent is given by the Moliére radius, is seen from the telescope. This ω approximately grows with

$$\omega(\theta) \approx \left\{1 - \ln(\cos\theta)\right\}^{-\kappa} \omega(\theta = 0\,\mathrm{deg}). \tag{4.8}$$

  Here, κ is a coefficient dependent on the height of the shower core with typical values between 0.9 and 1.5. For small angles, the expression $\left\{1 - \ln(\cos\theta)\right\}^{-\kappa}$ develops as $\cos^{\kappa}(\theta)$. An increased zenith angle qualitatively results in shrunk images.

- The threshold energy $E_{\mathrm{thresh.}}$, the lowest energy of a primary particle that can trigger the telescope, depends on a combination of these effects and is thus increasingly complicated. For small angles one can derive from the reasoning in [37] an approximate θ-development of

$$E_{\mathrm{thresh.}}(\theta) \approx \cos^{-2}(\theta)\, E_{\mathrm{thresh.}}(\theta = 0\,\mathrm{deg}) \tag{4.9}$$

  with a significant spread in the values for the cosine power for small angles θ. Qualitatively, an increase in zenith angle results in an increased $E_{\mathrm{thresh.}}$.

It is worth noticing that these results are derived from an extremely simplified model. The actual results depend highly on $\rho_{\mathrm{atm.}}$. For small angles θ however, these dependencies are mostly close to either $\cos(\theta)$, $\cos^{-1}(\theta)$ or $\cos^{-2}(\theta)$. As in this small angle regime, the relative evolution of $\cos(\theta)$ and $\cos^{-1}(\theta)$ is the same, and the grid used for IRF estimation was computed in $\cos(\theta)$ as shown in Figure 3.6; $\cos(\theta)$ is used as estimation parameter in the remainder of this thesis.

Earth's Geomagnetic Field

As introduced in section 2.4, electromagnetic EAS and electromagnetic components of hadronic EAS are composed of electron-positron pairs. When propagating through the electromagnetic fields in the atmosphere, they are thus subject to the Lorentz force

$$\boldsymbol{F}_{\mathrm{L}} = \boldsymbol{F}_{\mathrm{L,el.}} + \boldsymbol{F}_{\mathrm{L,mag.}} = q(\boldsymbol{E} + \boldsymbol{v} \times \boldsymbol{B}) \tag{4.10}$$

with electric and magnetic fields $\boldsymbol{E}$ and $\boldsymbol{B}$ for a charge q. Even though Earth's atmosphere contains an electrostatic field in the order of $120\,\mathrm{V\,m^{-1}}$ at ground level and fair weather conditions [68], where IACT observations are typically conducted, effects of this component are minor compared to the magnetic deflection as the latter scales with the incomming particles velocity that is, in the present case, close to the speed of light.

Contrary to the vertical electrical component, the magnetic component of the Lorentz force induced through the geomagnetic field presents a spatially more complicated effect. As the geomagnetic field is oriented, different incident directions of showers are subject to different Lorentz forces. The strength of this effect for electrons and positrons is proportional to

$$|\boldsymbol{F}_{\mathrm{L,mag.}}| = |\boldsymbol{v} \times \boldsymbol{B}| = |\boldsymbol{v}||\boldsymbol{B}| \sin \delta_{\mathrm{mag.}}. \tag{4.11}$$

and thus proportional to the sine of the angle δ between the geomagnetic field and the moving charge. As electrons and positrons are oppositely charged, this effect laterally separates them, widening the shower and its footprint.

The angle δ controlling this effect can be derived using basic geometry as

$$\cos \delta_{\mathrm{mag.}} = \frac{\boldsymbol{v} \cdot \boldsymbol{B}}{|\boldsymbol{v}||\boldsymbol{B}|}. \tag{4.12}$$

Here, $\boldsymbol{B}$ is given through its inclination $I_{\mathrm{mag.}}$, declination $D_{\mathrm{mag.}}$ and total field strength $|\boldsymbol{B}|$. Rotating the whole system to align the x-axis with the declination and recalling that the inclination is measured from the ground, $\boldsymbol{B}$ can be written as

$$\boldsymbol{B} = |\boldsymbol{B}| \begin{pmatrix} \cos I_{\mathrm{mag.}} \\ 0 \\ \sin I_{\mathrm{mag.}} \end{pmatrix}. \tag{4.13}$$

Assuming all shower particles moving parallel to the telescope, pointing at an altitude A or a zenith $\theta = 90\ \mathrm{deg} - A$ and an azimuth ϕ eastwards from north, $\boldsymbol{v}$ is given by

$$\boldsymbol{v} = |\boldsymbol{v}| \begin{pmatrix} -\sin\theta\cos\phi' \\ \sin\theta\sin\phi' \\ \cos\theta \end{pmatrix} \tag{4.14}$$

after accounting for the rotation introduced above through $\phi' = \phi - D_{\mathrm{mag.}}$ and further aligning the positive x-axis towards north, contrary to the usual convention for spherical coordinates having x pointing towards south. Substituting (4.13) and (4.14) into (4.12), δ computes to

$$\delta_{\mathrm{mag.}} = \arccos\left(\sin I_{\mathrm{mag.}} \cos\theta - \cos I_{\mathrm{mag.}} \sin\theta\cos\phi'\right). \tag{4.15}$$

In practice, the magnetic field components are provided through the International Geomagnetic Reference Field while changing over time and are thus interpolated between actual measurements. Computed for December 1st, 2021, at the ORM and 10 km above sea level, those values read $|\boldsymbol{B}| = 38.592\,\mu\mathrm{T}$ at $I_{\mathrm{mag.}} = 37.36$ deg down and $D_{\mathrm{mag.}} = 4.84$ deg west. Those values were used to define the grid shown in Figure 3.6. Given the reasoning above, $\sin\delta_{\mathrm{mag.}}$ will be used as the second estimation parameter throughout this thesis.

4.3 Estimation of IRFs with pyirf

As discussed in the previous chapters, the telescope's performance and, thus, the IRFs depend on observation conditions. Consequently, the optimal scenario would be the complete simulation of datasets with the exact conditions and the subsequent generation of a matching set of IRF components. This would, however, require a tremendous amount of computational resources and especially time. As mentioned in the preceding chapters, IRF estimation might provide a solution. For LST-1, IRFs are known at the grid nodes from the testing grid in some grid parameters mentioned in section 3.4. One possible two-dimensional grid is built in nodes of the parameters $\{\sin \delta_{\text{mag}}, \cos \theta\}$. For the remainder of this thesis, the IRF components at these nodes are named templates, and their direct dependencies on the parameters E, α, δ and t are as discussed in section 4.1, while the dependency on the grid parameters is indirect. For all discussed algorithms, the grid will be Delaunay-tesselated inside its convex hull into simplices, triangles build by one template in each corner. Lastly, the exact observation conditions of a measurement where an IRF file is needed are named target points after being translated into the grid-parameter space.

The challenge in estimating IRFs now lies in them being partially represented by conditional probabilities, discretized into histograms for computational reasons. This applies to M_{EDisp} and the PSF. The A_{eff} and θ_{cut} tables, as well as the, albeit not part of an IRF, gamma-hadron cut tables, are not of this nature; they are represented by not directly connected values. Estimating these quantities is thus comparably simply realized through known inter- and extrapolation algorithms such as linear and barycentric interpolation and extrapolatoric extensions beyond the grid nodes' convex hull. There are two main challenges regarding these estimations:

1. In bins where the amount of simulated events is not sufficient, a fill value replaces these three quantities, and these values are clipped when they fall outside a specified range. Thus, estimations from mixed sets of fill values and actual computations are not meaningful;

2. These components are interconnected in the case of point-like IRFs; the A_{eff} is computed using the θ_{cut} table. It is not guaranteed that independent estimations of these two will still match.

The first point can be handled by checking for these edge cases and refraining from building estimations between the questionable values; the latter needs dedicated studies, following in section 4.4.

For the more problematic M_{EDisp} and PSF, specialized methods are needed as simple, i.e., linear interpolation might result in unwanted multimodal results, as can be easily seen from considering simple Gaussians in Figure 4.3. Since similar problems were solved in high-energy particle physics, promising methods for interpolation exist. Two were adapted to the present use case by translating their formulation towards histograms rather than actual parametric probability density functions. They were implemented in `pyirf` throughout this thesis: Quantile Interpolation [114, 80] and Moment Morphing [23].

In summary and as discussed in Dominik, Linhoff, and Sitarek [53], Quantile Interpolation uses the fact that by construction, points x_i of the template distribution's cumulative distribution (CDF) F_i return equal values $F_i(x_i) = y$ as each of these functions is monotonically rising from 0 to 1. The

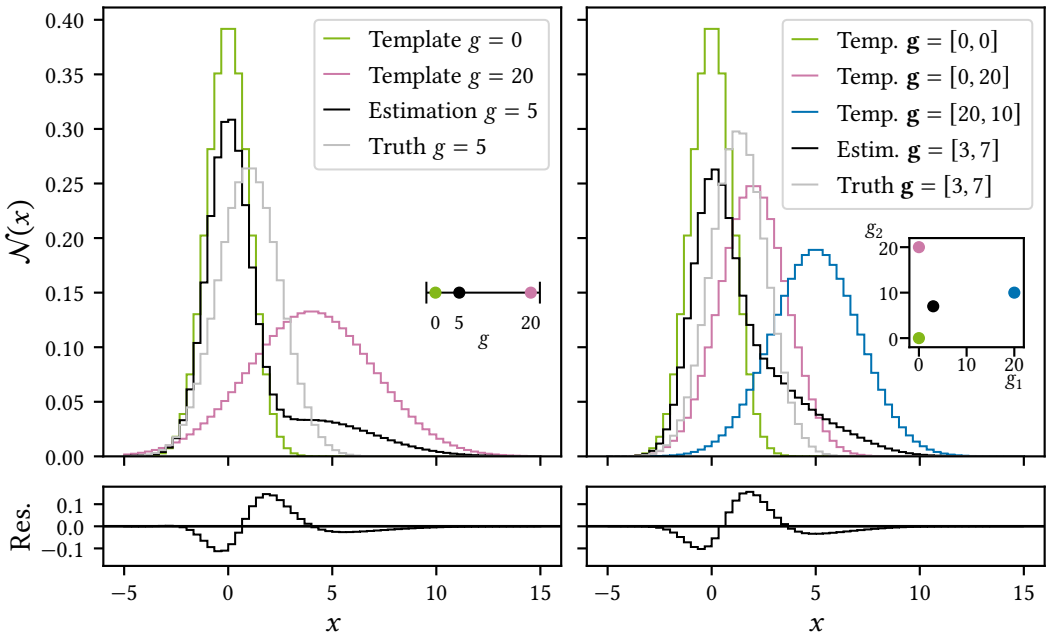

Figure 4.3: Linear (1D) and barycentric (2D) bin-wise interpolation between discretized Gaussians. Left: One grid dimension using Gaussians $\mathcal{N}(x \mid \mu(g), \sigma(g))$ with $\mu(g) = 0.2g$ and $\sigma(g) = 1 + 0.1g$. Right: Two grid dimensions using Gaussians $\mathcal{N}(x \mid \mu(\mathbf{g}), \sigma(\mathbf{g}))$ with $\mu(\mathbf{g}) = 0.2g_1 + 0.1g_2$ and $\sigma(\mathbf{g}) = 1 + 0.04g_1 + 0.03g_2$. Bottom line: Residuals truth - estimation. Insets: The assumed parameter grids.

target distribution's CDF is then constructed to return this value at x_j, a linear interpolation of the x_i to the desired target value. However, the x_i values are not a-priori known. The template distribution's quantile functions are thus substituted and ultimately interpolated, hence the name Quantile Interpolation. Moment Morphing, on the other hand, utilizes a Taylor expansion on the parameter grid to find suitable interpolation coefficients. These, in return, are used to construct a linear combination of the template distributions after centering them and accounting for their varying standard deviation.

As mentioned, both methods were adapted for discretized distributions. Quantile interpolation requires using empirical distribution functions instead of parametrized CDFs and estimations of the quantile functions through linear interpolation. As Moment Morphing requires the input templates' mean and standard deviation, approximative values must be estimated from the discretized functions. Since the original method further needed the evaluation of the probability density function, a look-up from the discretized distribution was implemented for this task. A last adaption was made to make the method applicable to irregularly shaped grids by using barycentric interpolation to compute the interpolation coefficients on triangulated grids in two parameter dimensions.

Quantile Interpolation can, in principle, be applied on parameter grids of arbitrary dimension, while Moment Morphing is restricted to up to two. Moment Morphing can, however, be used to

extrapolate beyond the grid's convex hull. This is currently realized by either using the nearest simplex to the desired target point within the convex hull to compute the extrapolation, thus accepting discontinuities in those regions where the nearest simplex changes, or by blending the results from all visible simplices as discussed in [13]. As complementary estimation options, Nearest Neighbor solutions to both inter- and extrapolation were developed and integrated into `pyirf` as part of this thesis.

As a first benchmark, both methods are applied to the Gaussian from Figure 4.3 in Figure 4.4. Both methods can correctly reconstruct the Gaussians' location and deviation, although some

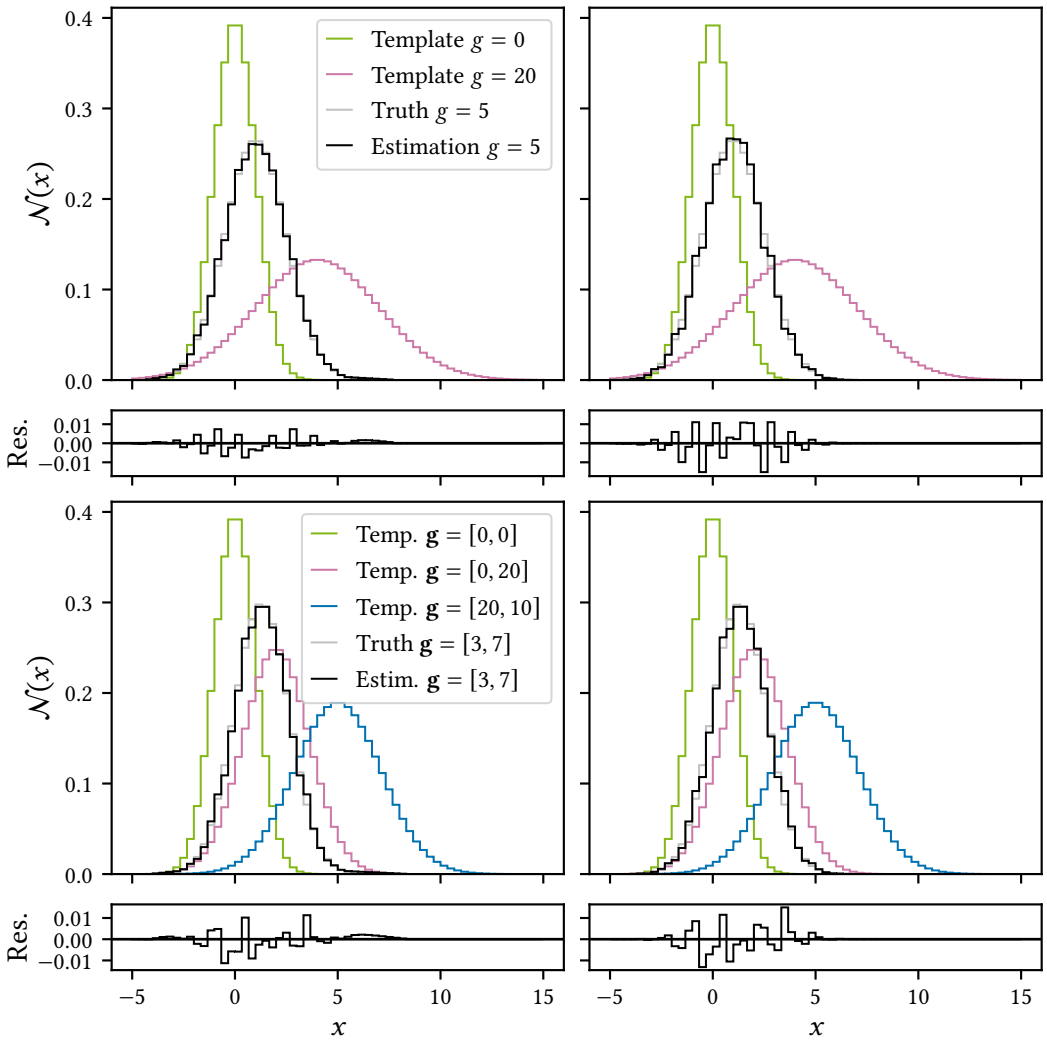

Figure 4.4: Interpolation between the Gaussians used in Figure 4.3 using Quantile Interpolation (left half) and Moment Morphing (right half). Upper half: One grid dimension with residuals truth - estimation. Lower half: Two grid dimensions with residuals truth - estimation.

imperfections are visible. While Quantile Interpolation (left half of Figure 4.4) results in some significant smearing into the tails of the resulting distribution, Moment Morphing shows an oscillating behavior between sections of under- and overestimation. While the latter is also, to a minor extent, the case for Quantile Interpolation, this effect most likely stems from the needed adaptions to discretized distributions and the related problems with discontinuities at bin-edges. Nevertheless, both methods' results lie within the expected error margins for approximative methods and perform well on one- and two-dimensional grids. It is, however, essential to note that the performance of both approaches varies within a small range respective to the target point and one method might outperform the other for a specific value. The presented values are chosen to show comparable performance from both algorithms.

For a more realistic case, Figure 4.5 applies both methods to skew normal distributions with a parameter a

$$\mathcal{N}_{\text{skew.}}(x \mid \mu, \sigma, a) = 2\mathcal{N}(x \mid \mu, \sigma) \int_{-\infty}^{a\left(\frac{x-\mu}{\sigma}\right)} \mathcal{N}(t \mid \mu = 0, \sigma = 1)\, \mathrm{d}t \tag{4.16}$$

so that $a = 0$ retains the normal distribution. Again, both approaches perform within expected error margins, although compared to Figure 4.3 the magnitude of the residuals increased. All but the one-dimensional Moment Morphing result seem more Gaussian-like and thus less skewed than the actual distribution at the target point, with the Quantile Interpolation results showing a heavier tendency towards this than Moment Morphing. While the magnitude of this again varies with the exact target point, the effect itself is not unexpected. For Quantile Interpolation, this follows from the approximative nature of the adaptions mentioned earlier in this section, which should result in problems where the distribution shows a high rate of change. In the present case, this should occur along the rising flank, a behavior visible in Figure 4.5. Moment Morphing, on the other hand, only accounts by construction for the mean and standard deviation of the distribution, not directly covering higher-order moments such as skewness. Under this aspect, it is surprising that the one-dimensional Moment Morphing result retains the characteristics of those in Figure 4.4. As mentioned, this is subject to slight change when choosing a different target point.

As a final toy data benchmark, Figure 4.6 applies Moment Morphing to an extrapolation case, again using the Gaussians from Figure 4.3. The one-dimensional case presents an extreme scenario, as the template distributions heavily change between narrow and wide, with the distribution at the target point being even narrower than the left-side template distribution. Regardless of these difficulties, Moment Morphing can correctly reconstruct the location of the target distribution, although the exact shape shows the highest deviation from the truth yet. Given this problem's challenge, the result still matches the target remarkably well. As the two-dimensional target distribution lies between the template distributions, the result is on par with those from Figure 4.4. If the target point moved further from the grid's convex hull, results would quickly resemble those from the one-dimensional case. Performance quickly deteriorates when moving too far from the template points, and negative bin entries are possible. While these can be clipped, the results are consequently less reliable than those from interpolation scenarios. As in this thesis' use case, extrapolation is only needed within a small region outside the grid, as can be seen for high $\cos\theta$ and $\sin\delta_{\text{mag.}}$ values in the upper right corner of Figure 3.6's right side, this should not be a problem.

To summarize these toy dataset tests, Quantile Interpolation and Moment Morphing perform

well on Gaussians and can sufficiently estimate skewed Gaussian distributions. As both methods provide estimation techniques, corresponding errors are to be expected. The encountered errors are, however, within reasonable margins. In addition to the excellent interpolation performance, Moment Morphing can extend beyond the grid's convex hull to solve extrapolation within reasonable boundaries. In general, however, interpolation results are more reliable than those from extrapolations.

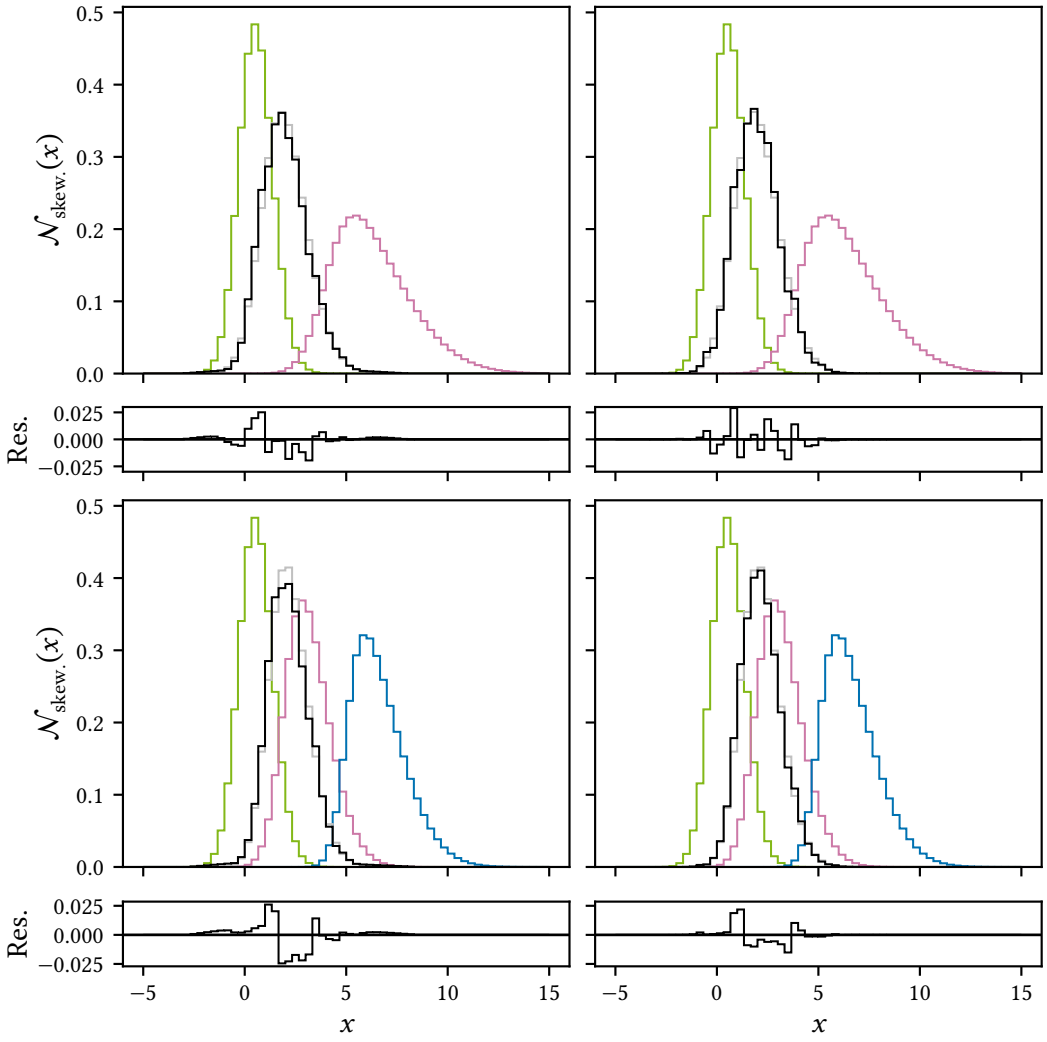

Figure 4.5: Same as Figure 4.4 but with skew normal distributions $\mathcal{N}_{\text{skew.}}(x \mid \mu(g), \sigma(g), a(g))$. For the one-dimensional grid, $a(g)$ is given by $1 + 0.1g$ and for the two-dimensional case $a(\boldsymbol{g})$ is $1 + 0.1g_1 + 0.05g_2$. The remaining parameters μ and σ are as in Figure 4.3. Upper half: One grid dimension with residuals truth - estimation. Lower half: Two grid dimensions with residuals. Left half: Quantile Interpolation. Right half: Moment Morphing.

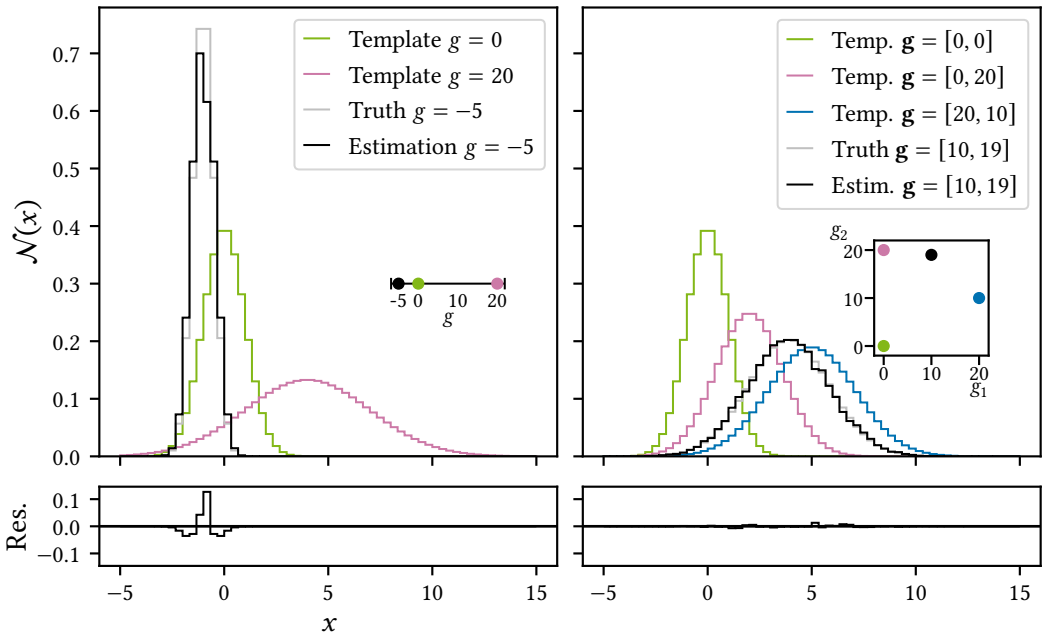

Figure 4.6: Extrapolation from discretized Gaussians using Nearest Simplex Moment Morphing from Gaussians given by the same relations as in Figure 4.3. Bottom line: Residuals truth - estimation. Insets: The assumed parameter grids.

4.4 Performance Measures on Estimated IRFs

While performance measures on toy data might give a good first insight into the working principles of the estimation algorithms, more problem-related tests are necessary. To do so, this chapter uses an actual subset of the IRFs produced for the analysis of LST-1 data to estimate IRFs at target points, where simulated IRFs are available. To test the interpolation capabilities, IRFs computed from simulations at (zenith, azimuth) pointings of (rounded) (10 deg, 248 deg), (15 deg, 355 deg) and (32 deg, 248 deg) will be used to estimate the IRF components at the target (24 deg, 259 deg). To provide an extrapolation setup, the second template is exchanged for a node at (15 deg, 175 deg).

Starting with the M_{EDisp}, the only component of a point-like IRF needing the specialized methods introduced earlier in this chapter, Figure 4.7 shows the results of applying both Quantile Interpolation and Moment Morphing to the interpolation setup. While both results seem to resemble the target sufficiently well at first glance, subtracting the estimations from the truth in Figure 4.8 shows that both methods shift the distributions towards smaller μ-values. While the magnitude of the shifting itself seems comparable between both methods, those results retained from Moment Morphing show considerably lower estimation errors. This is also evident in the Wasserstein distance shown in the lower row of Figure 4.8 where Moment Morphing can lower the metric value to values near zero for energies between about 100 GeV and 3 TeV. Quantile Interpolation also performs best in this energy range, although again considerably worse than Moment Morphing. Seeing the peak performance at those energies is not unexpected, as the LST's performance is optimized there, providing more regular and Gaussian-like shaped templates.

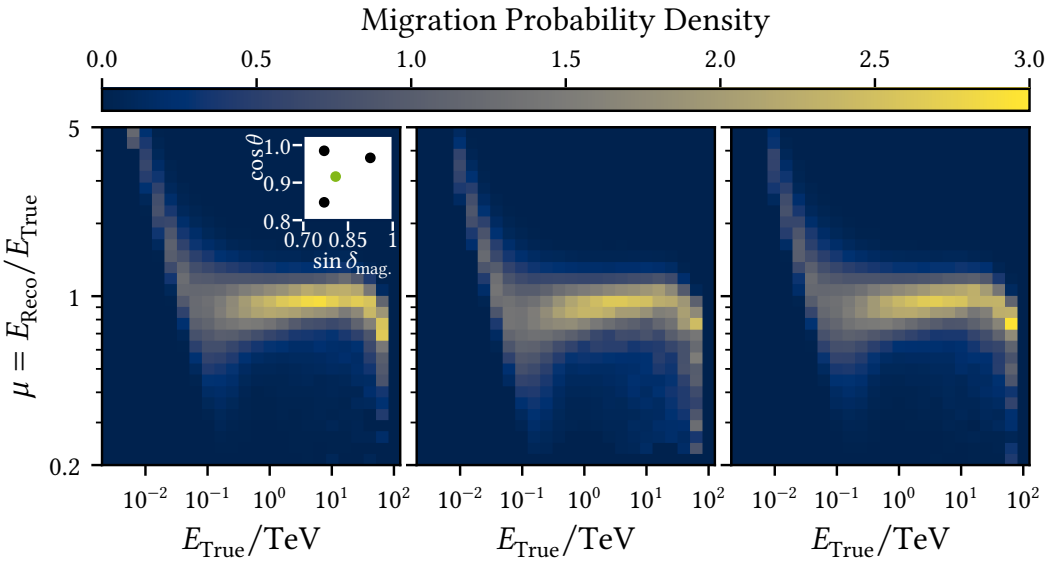

Figure 4.7: M_{EDisp}-tables interpolated from testing node IRFs computed using the Crab Nebula declination line as shown in Figure 3.6. Left to right: The simulated M_{EDisp} at the target point and M_{EDisp}s interpolated using Quantile Interpolation and Moment Morphing. Inset: The interpolation setup with the black template points and the green target.

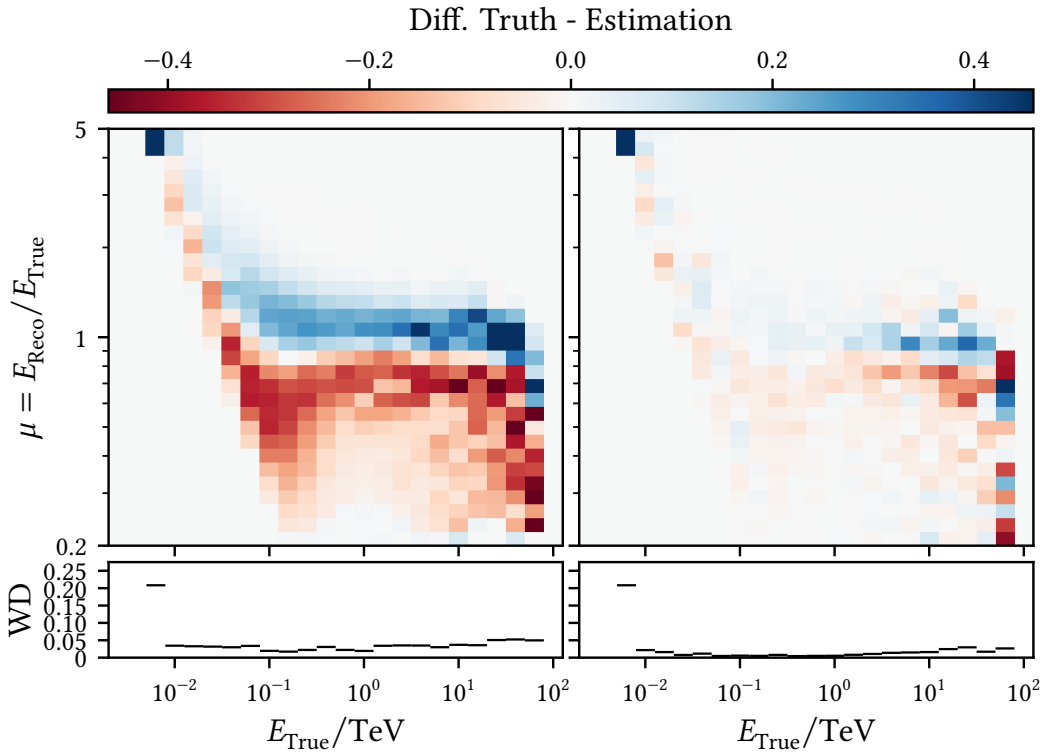

Figure 4.8: Absolute (upper row) and Wasserstein distance (WD, lower row) between simulated and Quantile (left) or Moment Morph interpolated (right) M_{EDisp} from Figure 4.7.

Applying Nearest Simplex Moment Morphing to the aforementioned extrapolation setup results again in well matching M_{EDisp}, as seen in Figure 4.9. The performance is comparable to Moment Morphing interpolation, although the Wasserstein distance ends at slightly higher values. Nevertheless, Moment Morphing shows excellent promise in estimating M_{EDisp} components of IRFs. As Moment Mophing is, at the moment, the only method that offers the possibility to be used for extrapolation and is outperforming Quantile Interpolation in the interpolation setting, it will be exclusively used for the estimation of M_{EDisp} for the remainder of this thesis.

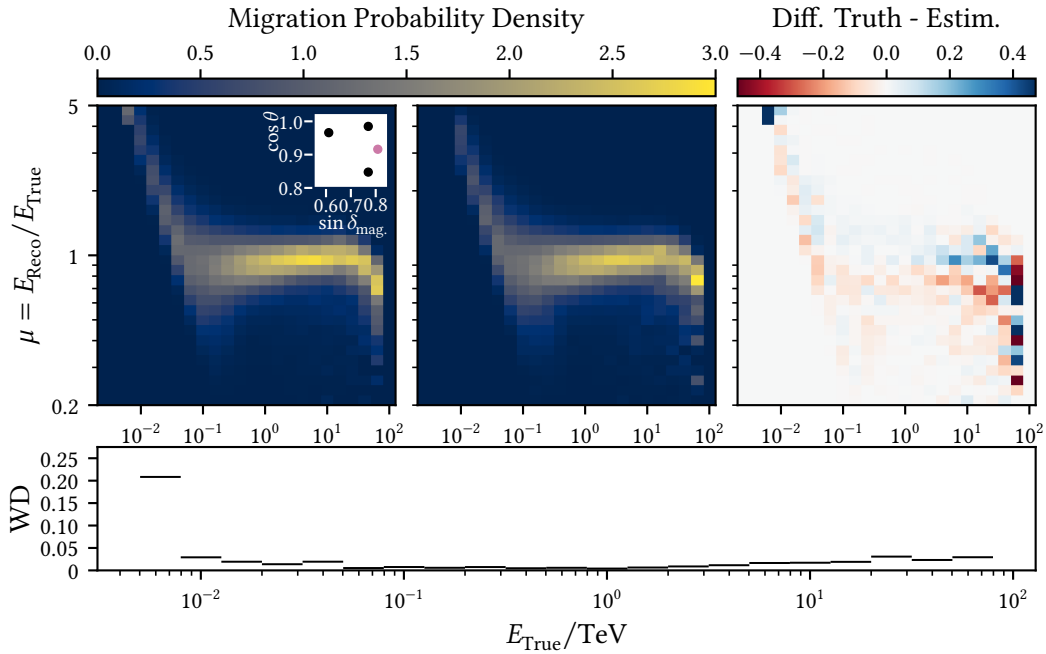

Figure 4.9: M_{EDisp}-table exptrapolated from IRFs computed at testing grid points shown in Figure 3.6 using the Crab Nebula declination line training nodes. Upper row: The simulated M_{EDisp} (left), M_{EDisp} extrapolated using Nearest Simplex Moment Morphing (mid) and the absolute difference between the former two (right). Lower row: The Wasserstein distance WD (right) between the simulated and extrapolated M_{EDisp}. Inset: The extrapolation setup with the black markers as template points and the magenta marker as the target.

Looking at the results obtained from estimating $\mathrm{A}_{\mathrm{eff}}$-tables, shown in Figure 4.10, both inter- and extrapolation again yield reasonable results. While the $\mathrm{A}_{\mathrm{eff}}$ is slightly underestimated for most energies, the best performance is again reached for medium energies between about 100 GeV and 3 TeV for the interpolation result. The extrapolation performance is slightly worse than the interpolation performance, although the differences are minimal. In conclusion, the $\mathrm{A}_{\mathrm{eff}}$ estimations result in a good matching compared to their simulated counterparts. However, this does not necessarily indicate a good matching between the estimated IRF components as discussed in section 4.3, and a corresponding test must follow below.

Repeating the test above for θ_{cut}, Figure 4.11 shows higher discrepancies. The interpolation results, driven by one template node, (15 deg, 355 deg) with $\sin\delta_{\mathrm{mag.}}$ near 1, show clear overestimation of

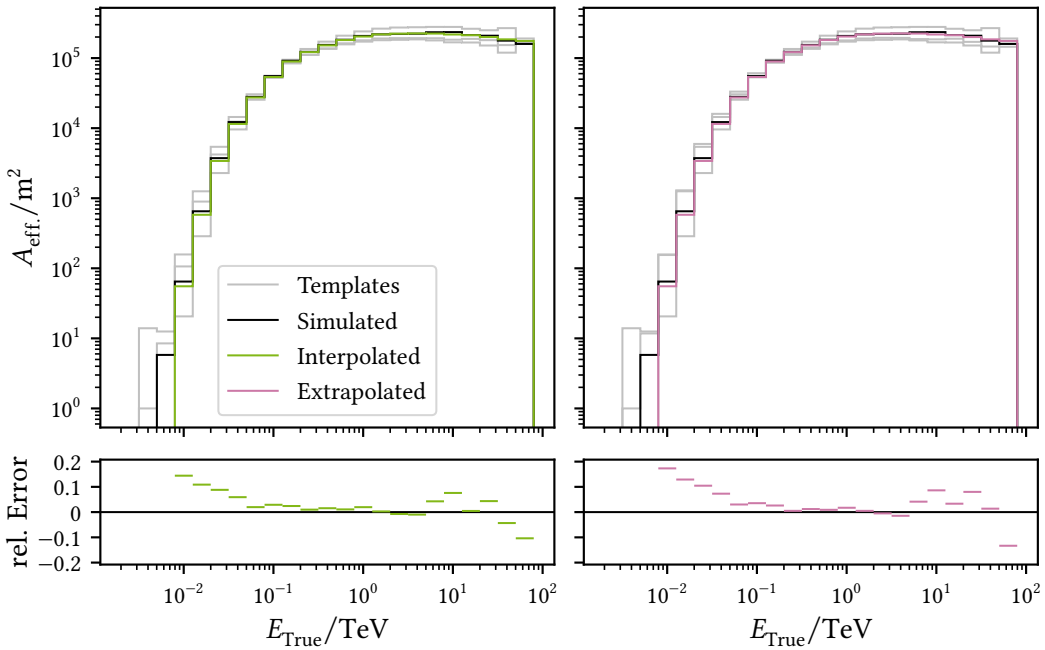

Figure 4.10: A_{eff}-tables inter- (left half) end extrapolated (right half) in the same settings as Figure 4.7 and Figure 4.9. Upper row: The A_{eff}-tables, lower row: The relative error $(A_{\text{eff.}}^{\text{Sim.}} - A_{\text{eff.}}^{\text{Est.}})/A_{\text{eff.}}^{\text{Sim.}}$.

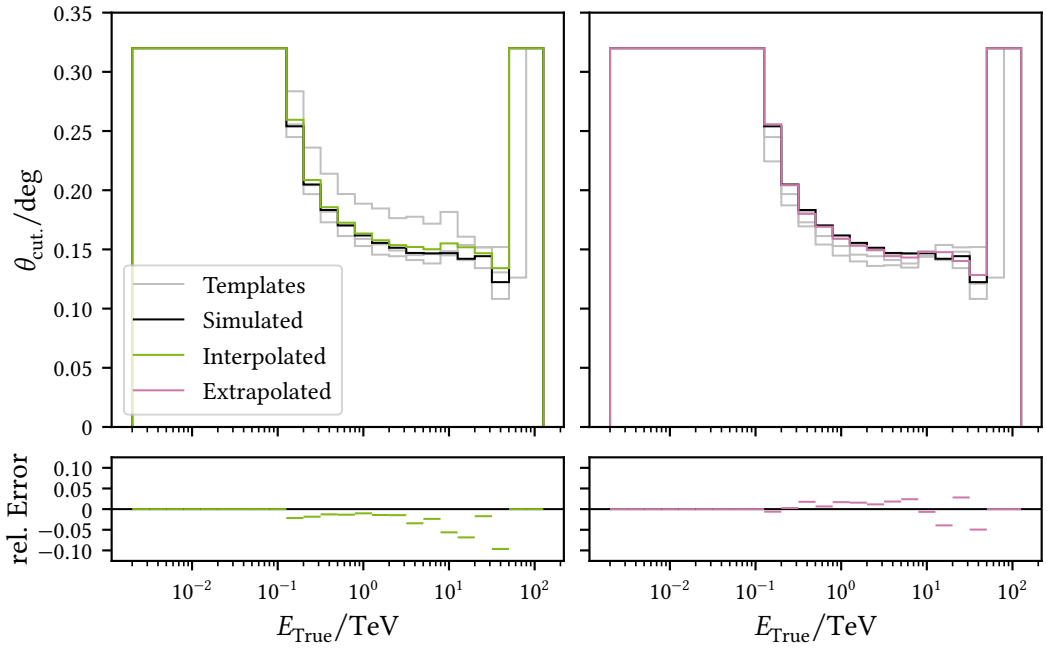

Figure 4.11: Same as Figure 4.10, but showing inter- (left half) end extrapolated (right half) θ_{cut}-tables.

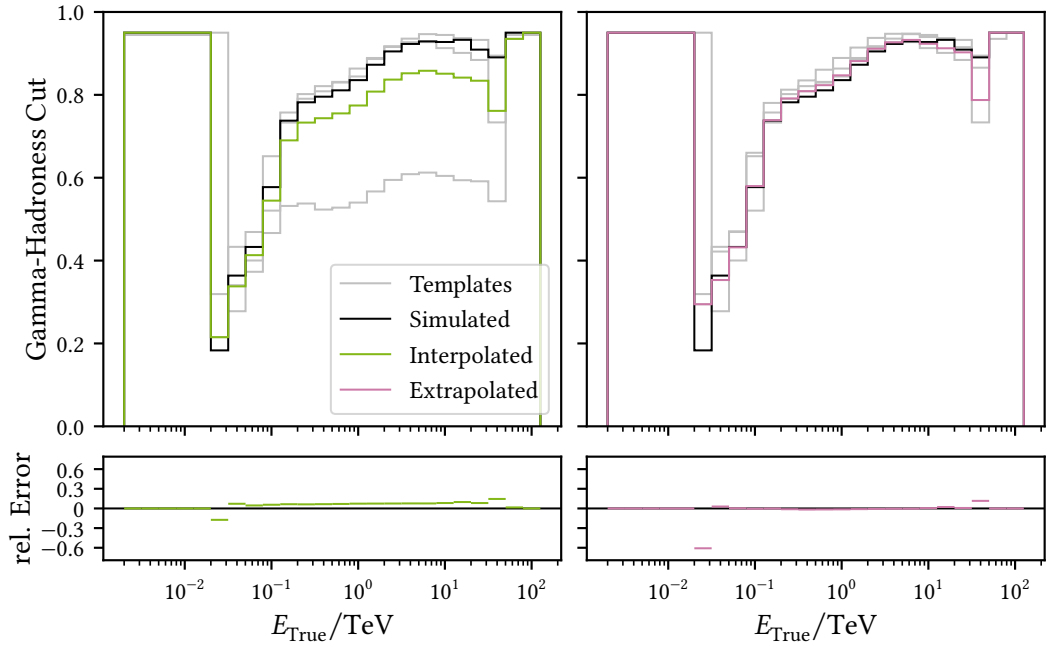

Figure 4.12: Same as Figure 4.10, but showing inter- (left half) end extrapolated (right half) gamma-hadroness cut tables.

the θ_{cut} values. While a high variance between the individual template node IRFs is not unexpected and $\sin \delta_{\mathrm{mag.}} \approx 1$ indicates that EAS from the corresponding directions experience the strongest magnetic field effects with negative effects on the origin reconstruction, the overestimation indicates that this does not influence the θ_{cut}-tables linearly. Consequently, there might be a better-suited grid for this exact estimation task. However, again, the best performance is reached for medium energies. As the extrapolation setup does not include a template node with such a high $\sin \delta_{\mathrm{mag.}}$-value, the results are slightly closer to the simulated entries. The results are, however, underestimated, further contributing to the picture that the θ_{cut}-tables' dependencies are non-linear.

This effect is even more substantial for the interpolation of gamma-hadroness cut tables, even given that those are no constituent of an IRF albeit needed to compute one. As can be seen in the upper left panel of Figure 4.12, the high-$\sin \delta_{\mathrm{mag.}}$ node shows severely lower cut-values than the two remaining template nodes. Hence, the estimated values are underestimated by the simulated values. As the extrapolation templates are again all at more comparable values, the extrapolation shows a nicely matching result.

While the deviation of the interpolation results might seem discouraging, the important question is again the matching between the components themselves. It is important to remember that both gamma-hadroness cuts and θ_{cut}-tables are computed in a way that ensures that either a quantile of most gamma-like events or of gamma events reconstructed most closely to the assumed source remain. Both values are somewhat arbitrary and, in the test case, set to 70 %. Even though it is obvious that the interpolated components no longer satisfy this value, this is not much of a problem as long as the A_{eff}, for the template nodes computed using both cut-tables, correctly accounts for it.

Conducting this test, one finds in Figure 4.10 that for the interpolation case, where high discrepancies were found, the recomputed A_{eff} lies up to 20 % over the estimated A_{eff}. There is thus some mismatch between the estimated A_{eff} and the estimated θ_{cut} and gamma-hadroness tables. It is, however, important to notice that, despite strong discrepancies in the respective components, the corresponding A_{eff}, a quantity spanning over five orders of magnitude, still yields remarkable results. For the extrapolated results, as was to be expected due to the good component-wise performance, the recomputed A_{eff} well matches the extrapolated one.

In short summary, IRF estimation performs sufficiently well. Despite discrepancies in individual components in cases where one template IRFs presents an outlier case, the estimated IRFs still match the simulated ones remarkably well. From the conducted tests, IRF estimation shows great promise in yielding reasonable IRFs on short timescales with minimal resource consumption.

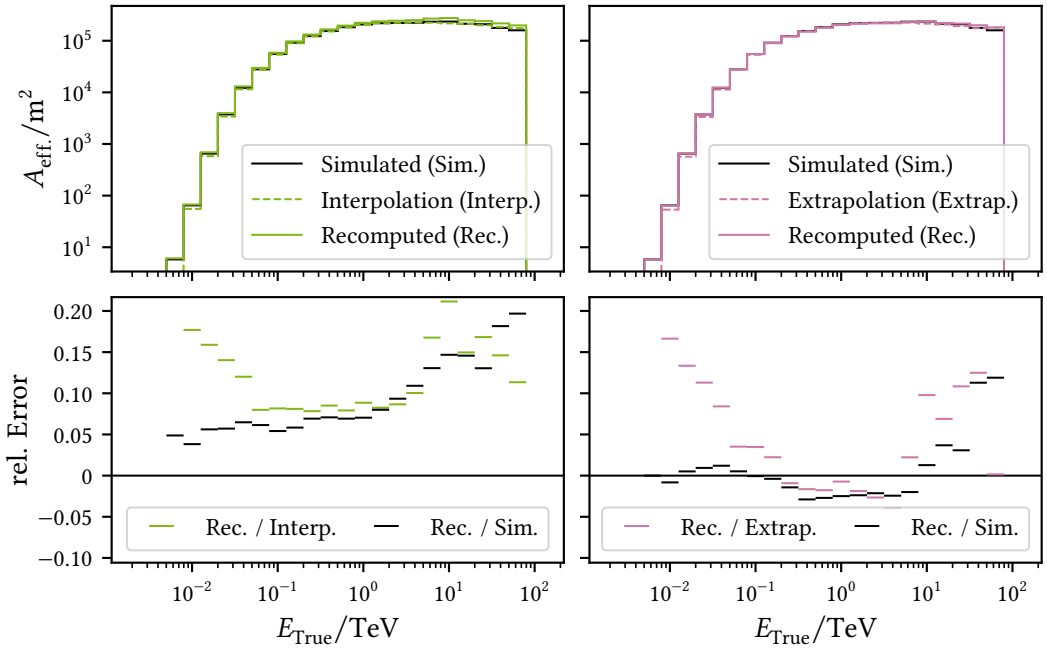

Figure 4.13: Comparison between the estimated A_{eff}-tables from Figure 4.10 and A_{eff}-tables computed from simulations using the estimated θ_{cut} and gamma-hadroness cut tables from Figure 4.11 and Figure 4.12. Left half: Interpolated components using the same setting as in Figure 4.7. Right half: Extrapolated components using the same setting as in Figure 4.9. Upper row: The A_{eff}-tables, lower row: The relative error $(A_{\text{eff.}}^{\text{Rec.}} - A_{\text{eff.}}^{\text{Est./Sim.}})/A_{\text{eff.}}^{\text{Rec.}}$.

4.5 High-Level Analysis in gammapy

The previous chapter explained in greater detail methods to compute IRFs, either through direct computations from matching simulated DL2 datasets or through estimation techniques from a grid of IRFs. Both methods, to varying extend, need simulated DL2 datasets beforehand, the goal was to

produce science ready DL3 files in any case. These files, the reconstructed signal events alongside the matching IRF, are then handed to the analyzer and contain all information needed to extract spectral, spatial and temporal information. For this task, CTAO declared the open source Python package `gammapy` [54] its official science software. Consequently, `gammapy` is compatible with the open gamma-ray astronomy data format standard for DL3 data [109] and thus multiple existing experiments such as MAGIC started to increasingly incorporate it into their high-level analyses. The final aim of `gammapy` is to produce DL5 data, scientific results such as a light curve or a SED.

The first step towards DL5 results is a binning of the per-event data provided by the DL3 files, designated DL4. While an immense data reduction, this binning only allows for further analysis as a spectrally, spatially, and temporarily continuous observation is currently not possible. The nature of this binning depends on the desired DL4 products. If the analyzer wishes to extract information from all three dimensions, the binning must be done in time, energy and space. This, of course, implies both a high amount of observations and a sufficient resolution in the respective dimensions to obtain reasonable results. While the observation time is sufficiently well known, as was discussed in section 4.1, and the energy resolution of a mono-telescope such as LST-1 can be seen as sufficient, the spatial resolution is strongly limited by the unavailability of stereo information. Thus, this thesis only aims to extract spectral and temporal information, namely SEDs and light curves and only requires point-like instead of full enclosure IRFs, as was already mentioned in section 4.1. However, there are already promising attempts to include spatial results into LST-1 analyses, and CTAO will provide the optimal experiment for this kind of analysis once more telescopes become available.

To extract a physical model and thus the DL5 information from this binned data, `gammapy` currently provides a likelihood approach, assuming Poissonian bin-statistics. For this thesis, as it uses on-off wobble mode observations without a specific background model, `gammapy` applies a so-called WStat fit statistic. In this approach, the expected number of background events is marginalized from the likelihood, meaning it is treated as a free parameter that can be obtained by minimizing the corresponding negative log-likelihood. For the expected number of signal events, a flux model $\phi(\vartheta)$, e.g., a log-parabola SED as in Equation 2.7, is folded with the IRF and inserted into the likelihood. Then again, minimization of the negative log-likelihood using `iminuit` [50], a `python` wrapper for minuit [85], allows for the estimation of the model parameters ϑ. From there, flux points can be estimated by re-fitting the model in the desired energy range. While this whole procedure could, in principle, be applied to each singular DL4 file, the spectral flux model is typically retained from combined observations. Two options currently exist in `gammapy`. Assuming all observations to be taken under the same conditions, all data can be stacked before starting the fitting procedure, combining all IRFs-components into one weighted average. This would, to some extend, void the idea of this thesis to compute matching IRFs on a per-observation basis. The alternative approach computes a joint likelihood from all singular observations with their respective IRFs and is thus used in this work. On the downside, bins with a low event count cannot be used in a meaningful way; the singular likelihoods will partially be evaluated near or at bin counts of zero. Consequently, information at the highest energies is not accessible.

Even though introducing a complete temporal model would be possible in the same way the spectral model was accounted for, this thesis only aims to compute a light curve, showing simple

temporarily binned variability of a source. To extract this light curve, gammapy reestimates the flux model normalization for the stacked observations of each time bin, keeping the remaining parameters fixed, and then integrates the model in energy bins. In reminiscence of the integrated flux from Equation 2.2, this thesis aims to extract only light curves for energies in one bin over 100 GeV. This thesis' high-level workflow, wrapping the routines provided by gammapy, relies on and extends groundwork provided by N. Biederbeck [32] and L. Nickel [107]. An overview over the used software packages is given in Appendix C.

From this DL5 data, outside the scope of this thesis and the current operational status of CTAO, a final DL6 stage exists. This DL6 offers some of the long-term goals of CTAO, providing catalogs or sky surveys to the community. Thus, it is comprised of a collection of the DL5 science results for multiple sources.

Analysing the VHE Standard Candle - the Crab Nebula

5

With the promising results from the tests in the previous chapter, the next step is to continue the high-level analysis using estimated IRFs. As the Crab Nebula is VHE gamma-ray astronomy's standard candle, it is the typical target for such a test, and since it is a common observation target for all IACT experiments, including LST-1, a massive amount of observation time was already dedicated to this source. Following this reasoning, the CTAO-LST project, in its first performance study, utilized Crab Nebula observations and nearest neighbor IRFs to assess LST-1's capabilities. Consequently, a sufficient sample of data taken at good observation conditions by LST-1 is available at a comparably high data level and will be used here. The next step is thus to repeat the LST-1 analysis using estimated IRFs to assess their usage implications while closely following the mentioned LST-1 analysis for comparable results.

5.1 Data Selection and Analysis Configuration

Both data selection and analysis configuration for the analysis presented in this chapter follow those of the LST-1 performance paper [5]. This analysis thus starts with 117 observation runs, taken between November 18, 2020 and March 5, 2022, amounting to 35.9 h of Crab Nebula observations taken at zenith distances below 35 deg, dark sky, and good atmospheric conditions. Accounting for dead time, [5] estimated the sample to span a live time of 34.2 h. The distribution of the measurement time is shown in Figure 5.1. As this sample has already been used for a publication, it is present at DL2 level, and no customizations at the preceding data levels were applied in this thesis. It is, however, important to notice that the software used to prepare said publication contained a bug in an older `pyirf` version that introduced a wrong normalization of the M_{EDisp} tables and further applied a stacked rather than a joint analysis. Consequently, the results presented below will not precisely match those from [5] even when computed with Nearest Neighbor IRFs.

From DL2 onwards, events were further selected to have at least been parametrized with an intensity parameter above a value of 80 p.e. While [5] showed that a value of 50 p.e. would suffice for data taken after August 2021 when tests to find optimal trigger settings concluded, the 80 p.e. value is applied to the whole dataset for common analysis settings. For the processing towards DL3 files, the point-like IRFs are computed with energy-dependent gamma-hadroness cut and θ_{cut} tables, yielding an efficiency or containment of 70 %. As the $\sin\delta_{\mathrm{mag.}}$-values are naturally mirrored around $\phi' = 180\ \mathrm{deg} - D_{\mathrm{mag.}}$, overlapping points in $\left(\sin\delta_{\mathrm{mag.}}, \cos\theta\right)$-space exist. These overlaps, corresponding to different azimuth pointing, would cause problems with the Delaunay triangulation used to find the estimation nodes and must not necessarily yield matching IRFs. The estimation was thus computed on the IRF subset closest to the target point. The further

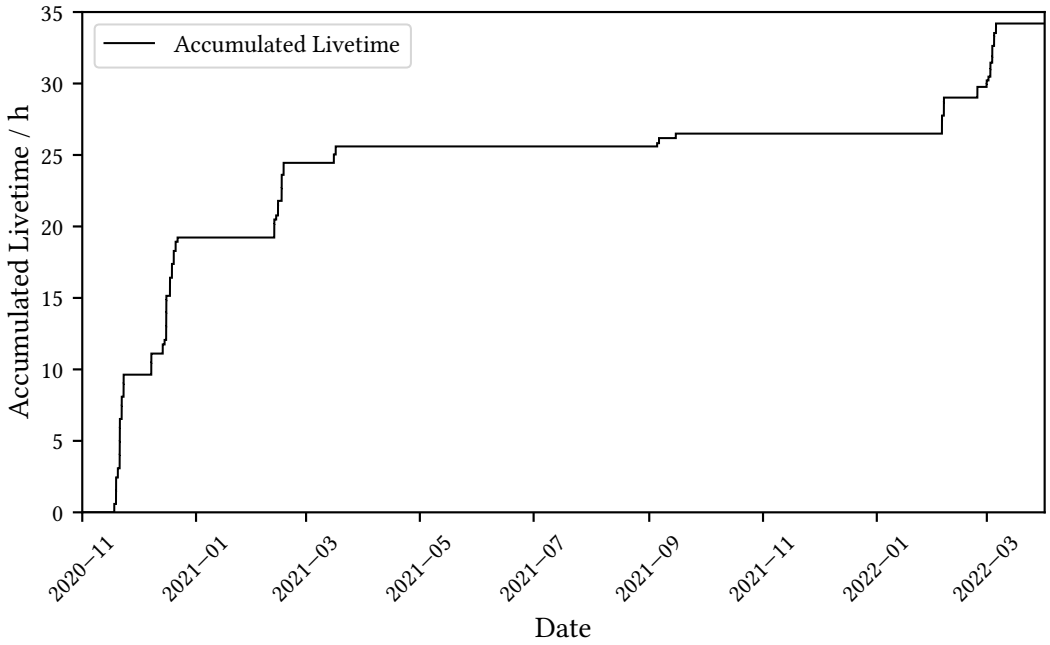

Figure 5.1: Cumulative distribution of the dead-time corrected measurement time used for the presented Crab Nebula analysis.

configuration used during the processing from DL2 to DL3 is attached in Listing 1 of appendix A.1. This configuration also contains information on the binning and fill or capping values used to create the IRFs. The used observation runs are given in Listing 9 of Appendix B.

For the high-level analysis, the Crab Nebula flux is parametrized as a log-parabola SED, as given in Equation 2.7. The starting values used in minimizing the negative logarithmic likelihood, as discussed in the previous section 4.5, can be found in Table 5.1 and corresponds to the results of [5]. As usually done when fitting a log-parabola, the reference energy E_0 was frozen and thus not minimized. One average SED was fitted between 50 GeV and 10 TeV using a joint likelihood fit to preserve the individual IRFs. Building upon this SED, 20 flux points were computed between 30 GeV and 10 TeV. The night-wise light curve only contains the flux above 100 GeV for increased robustness against background fluctuation due to the dramatically decreased measurement time per observation night. All configurations used for the high-level analysis are shown in Listing 2 and Listing 3 of appendix A.1. Besides the mentioned energy ranges, these files rely on `gammapy`'s defaults.

Table 5.1: Starting values for the minimization used to derive the Crab Nebula log parabola SED as in Equation 2.7

Parameter	A	E_0	α	β
Meaning	Amplitude	Ref. Energy	Spectral Ind. at E_0	Curvature
Value	3.05×10^{-10}	0.4	2.25	0.114
Unit	$\mathrm{cm}^{-2}\,\mathrm{s}^{-1}\,\mathrm{TeV}^{-1}$	TeV		

5.2 Analysis Results

As described earlier, the following analysis will focus on obtaining SEDs and light curves from the 117 Crab Nebula observation runs. To further assess the quality and usability of estimated IRFs, the following Crab Nebula analysis will be performed with both nearest neighbor and estimated IRFs. For a preliminary assessment of the data quality and a first estimate of the differences between both IRF types, θ^2 and excess significances will be shown first to assess the influence of the estimated cut values. The next step then showcases the obtained SEDs and flux points, followed by the light curves.

5.2.1 θ^2 Plots and Excess Significances

As a first analysis step, Figure 5.2, Figure 5.3, Figure 5.4, and Figure 5.5 show histograms of all events present in the 117 observations' DL3 files' on and off regions in bins of θ^2 for low, medium, and high energies as well as a cumulated version both for an analysis using nearest neighbor and estimated IRFs. As with the θ_{cut} tables, the distance θ gives the angular distance of each event's reconstructed position to the known position of the Crab Nebula. Consequently, events in the first θ^2 bin were reconstructed closest to the Crab Nebula's catalog position. All energy bins show an apparent signal excess close to the Crab Nebula position for analyses performed with both nearest neighbor and estimated IRF compared to the respective off-region measurements. All off measurements appear sufficiently flat, as would be expected, with the low energies showing the highest fluctuations. Using Equation 3.1 and clipping negative significances to 0, the overall excess from the summation of all events used up to $\theta^2 = 0.2\ \text{deg}^2$ is significant in all shown energy bins. While the lowest energies contribute the most events to the overall analysis, the corresponding excess over the off measurement is limited, as seen in Figure 5.2. This is not unexpected. Not only is the source position reconstruction for low energy gamma-ray events more prone to errors as the light yield in the camera is low, and thus, the Hillas parameters needed are less reliable, but there is also a significant background of misclassified hadronic events. Especially this energy range will thus profit from the stereoscopic system future that multiple LSTs will provide. The highest excess and significance are found for medium energies; high energies show the flattest off-measurement distributions.

Interestingly, the event rates from DL3 files obtained with estimated IRFs are significantly higher than those from nearest neighbor IRFs. This effect stems from the different gamma-hadroness cut tables that select the signal events. As the excess rates are the same and thus only a constant offset is introduced to the data, this observation is not concerning but showcases the possible influence of the gamma-hadroness cuts. Consistent with the matching excess rates, the Li-Ma significances between both analyses vary within a small margin and are thus comparable. This translates to Figure 5.6, where the θ^2 bin-wise for the energy bins of Figure 5.2, Figure 5.3, Figure 5.4, and Figure 5.5 is shown. As can be seen from the rightmost difference panel, most deviations fall within $\pm 1\,\sigma$, with slightly higher significances from the nearest neighbor analysis being seemingly more prevalent than from the estimated IRF analysis.

Consistently between both analyses and as could have been assumed from the excess rates shown before, the significances from the low energy events drop quickly below $5\,\sigma$. At the same time,

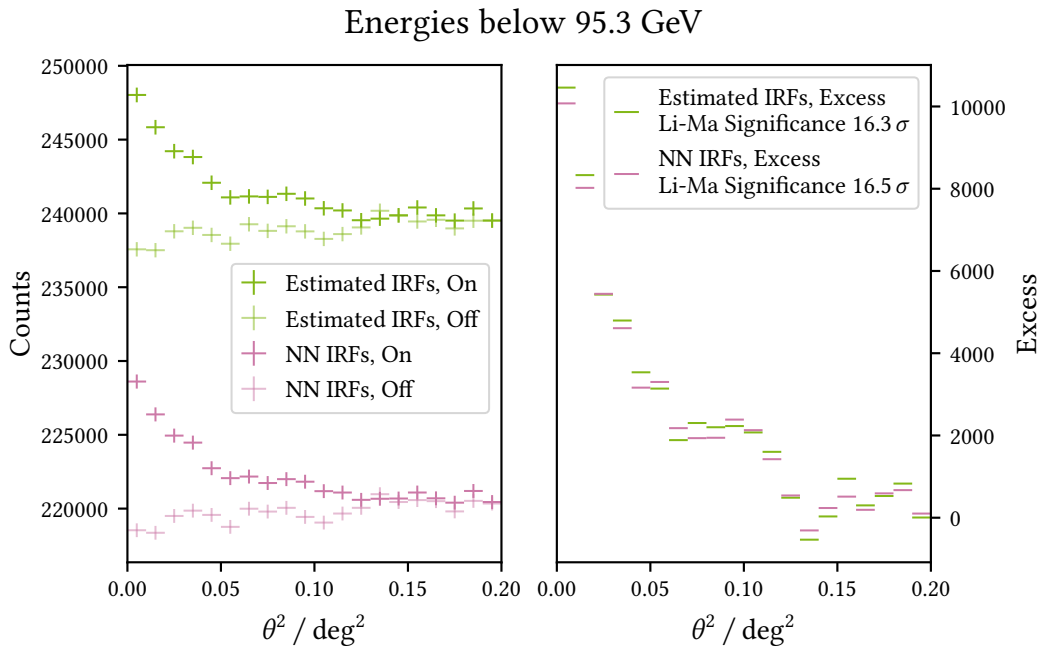

Figure 5.2: Left: θ^2 plot of low-energy events up to 95.3 GeV for estimated and nearest neighbor (NN) IRFs. Right: Corresponding excess plot with Li-Ma significance according to Equation 3.1.

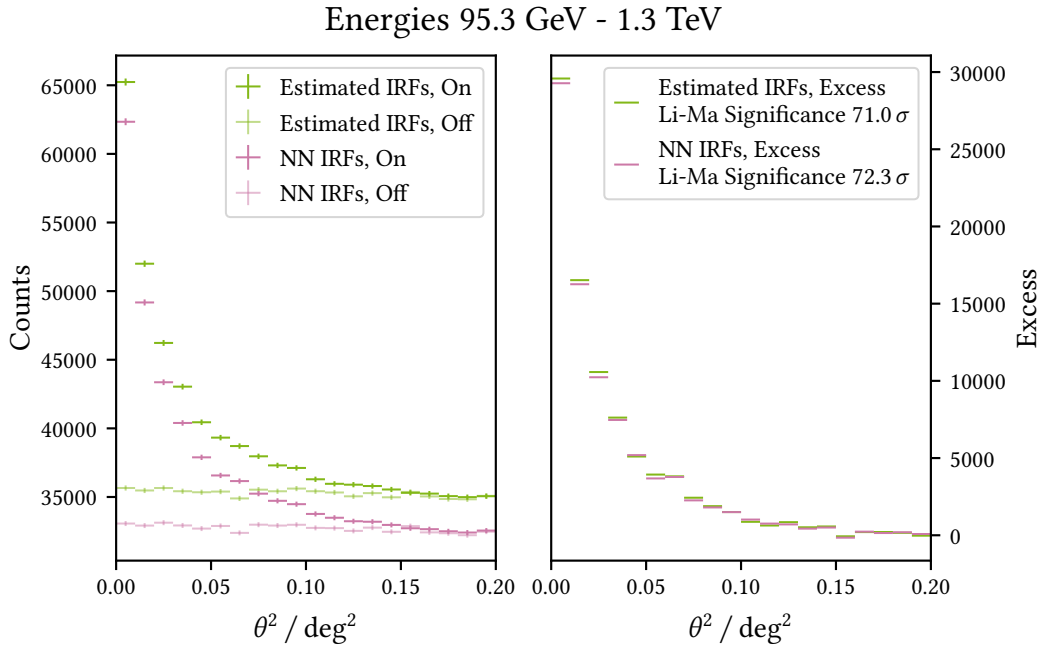

Figure 5.3: Same as Figure 5.2 but with medium energy events between 95.3 GeV and 1.3 TeV.

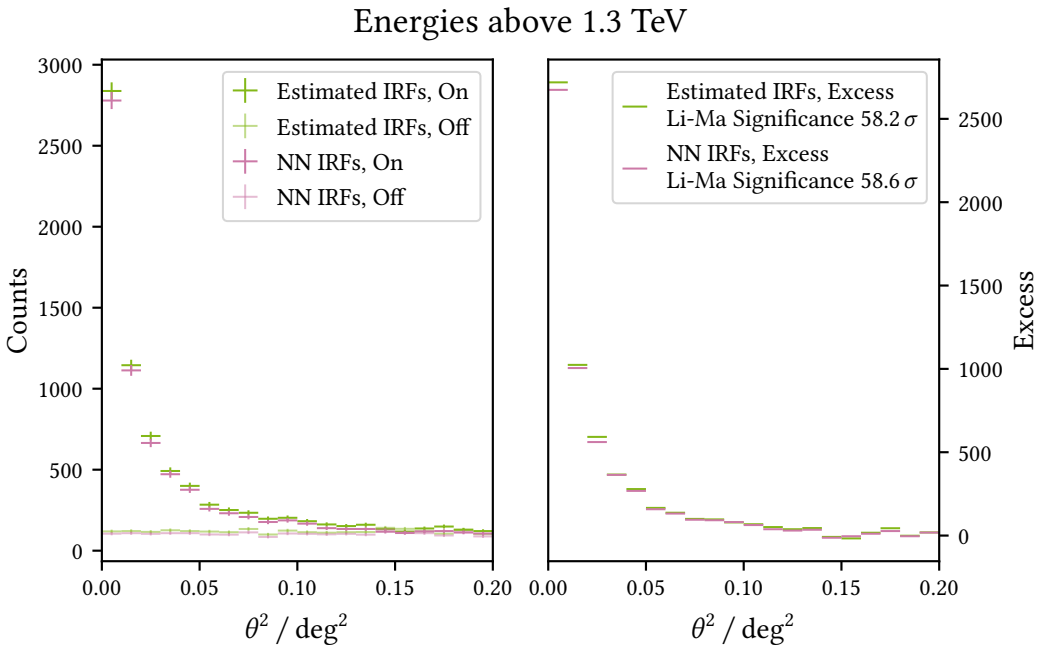

Figure 5.4: Same as Figure 5.2 but with high energy events above 1.3 TeV.

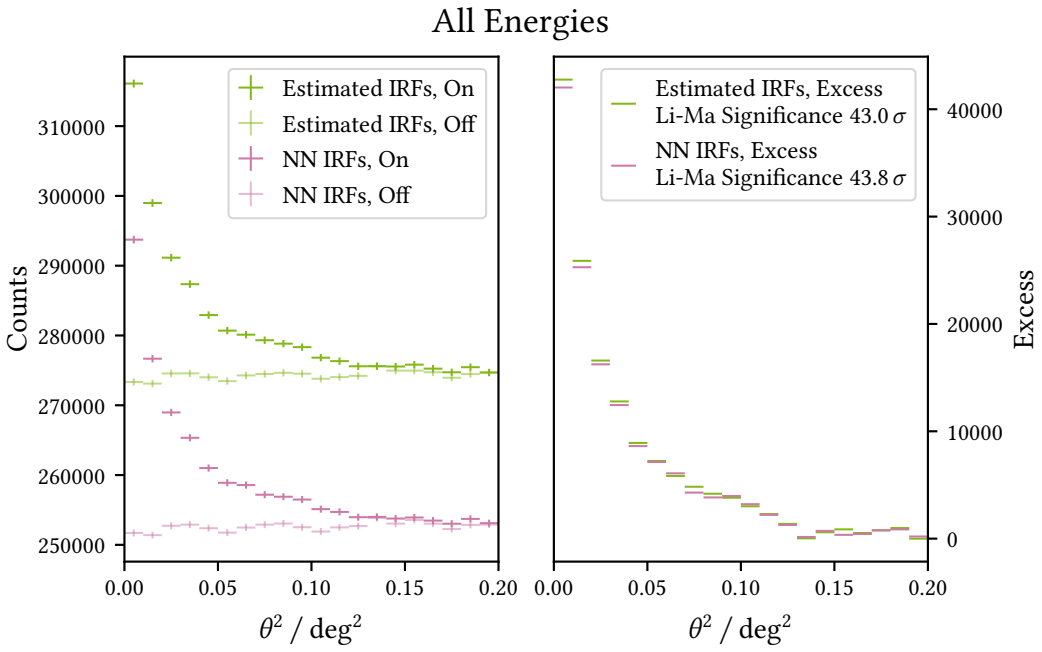

Figure 5.5: Same as Figure 5.2 but with all events.

the remaining higher energy bins yield higher significances also for higher θ^2 values. However, it is important to stress that, with these analyses being point-like, there is no information on, e.g., the source's extent at a certain energy that can be derived from these plots. On the other hand, they show a clear detection of the Crab Nebula at all energies and indicate where the highest sensitivities, and thus, the most reliable high-level results are to be expected.

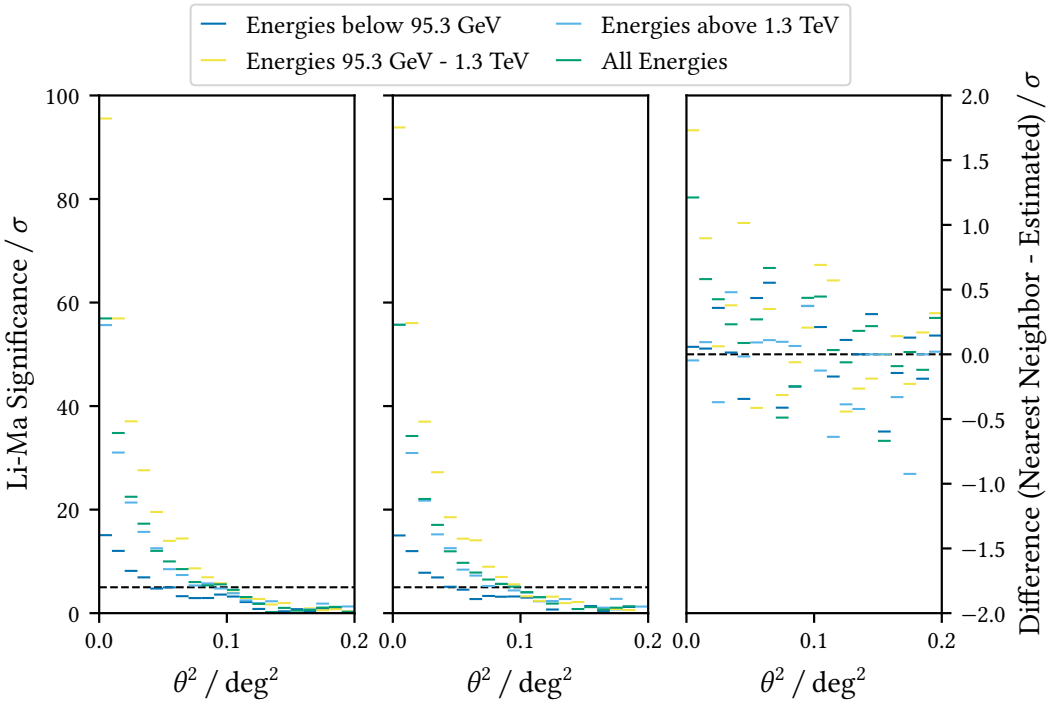

Figure 5.6: Li-Ma significances in bins of θ^2 for the energy bins used in Figure 5.2, Figure 5.3, Figure 5.4, and Figure 5.5 for analyses performed with both nearest neighbor (left) and estimated IRFs (center) alongside the difference (right) between them.

As the (excess) count rates, as expected from 34.2 h of observations of a bright source, are overall high, Figure 5.7 enables a more detailed insight into the data by an even finer binning of the events before computing the Li-Ma significances. As can be seen in the central plots, the highest excess significance is found for energies between 100 GeV and about 3 TeV, with significances about 5 σ being achieved up to 10 TeV. When again comparing both analyses by computing the differences between the respective significances in Figure 5.8, the nearest neighbor analysis results in higher excess significances most of the time. Both results, again, mostly lie within an interval of 1 σ.

In summary, the θ^2-plots, the excess rates and the Li-Ma significances show a clear detection of a signal excess at the Crab Nebula position in the used dataset. As the significances easily surpass 5 σ and the event rates are high, the chosen set of observations presents an optimal case to study the effects of estimated IRFs on the results, as they will not be governed mainly by statistical effects.

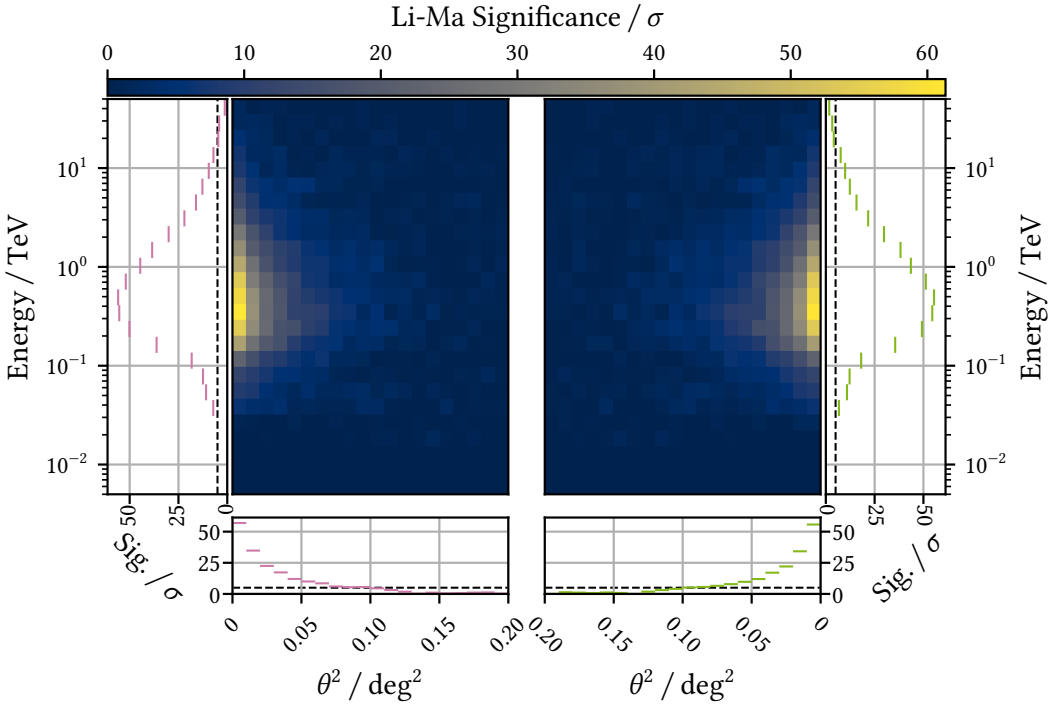

Figure 5.7: Li-Ma significance according to Equation 3.1 in bins of θ^2 and energy for DL3 files produced with nearest neighbor (left half) and estimated IRFs (right half). The side and bottom plots show the significance after the summation of all events over the respective axis. The black dashed lines indicate a significance of 5 σ.

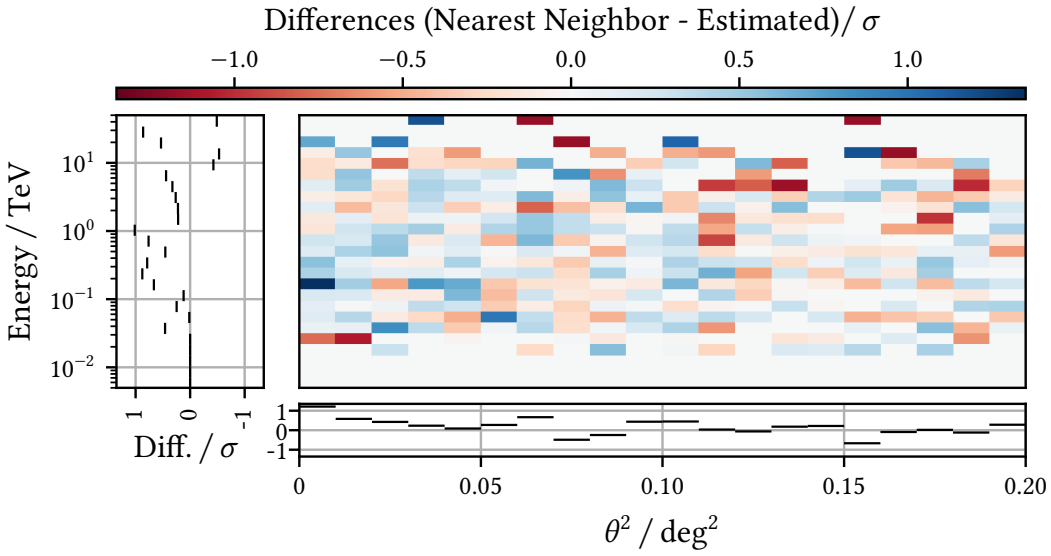

Figure 5.8: Significance differences between the nearest neighbor and estimated IRF analyses for the respective panels of Figure 5.7.

5.2.2 Obtaining SEDs

Looking at Figure 5.9, both analysis scenarios result in reasonable SEDs with flux values in the expected order of magnitude. The same holds for the corresponding parameter values, which are given in Table 5.2. The corresponding flux points, which are, as mentioned in section 4.5, not independent from the SED parameterizations, follow the curves closely. While deviations in the low and high energies are present and expected, the high self-consistency between flux points and SEDs indicates a proper fit performance and a good match between the original data and the obtained models.

The direct comparison between nearest neighbor and estimated IRF results, with the difference between the respective SEDs shown in Figure 5.10's upper and the difference between the flux points in Figure 5.10's lower panel, shows an excellent matching between both analyses. While the SED difference is on the order of a few percent, even in the lower energies, the flux point difference is compatible with zero, given the error estimates. This was to be expected given the good matching in the previous θ^2 plots and again shows the therein-found systematic offset to be no problem. On the other hand, the high similarity between nearest neighbor and estimated IRF analyses suggests that for the presented IRF grid density, IRF estimation is not yet needed, and the usage of nearest neighbor IRFs provides sufficient results, at least near the Crab Nebula trajectory. It is worth noticing that this is the wanted result of this test, as the Crab Nebula was observed in excellent conditions for an excessive amount of time near a sufficient number of IRF grid nodes. Substantial deviations between both analyses would indicate problems with the estimated IRFs. These deviations are nowhere to be found; the results are nearly indistinguishable.

Contrary to the excellent agreement between both analyses, the discrepancies between the LST-1 results obtained here and the 2015 MAGIC reference [10] are clearly visible, with the LST-1 SEDs yielding consistently higher fluxes than MAGIC, as can also be seen in the upper panel of Figure 5.10. It is, however, essential to note that the offset between both SEDs is amplified by the E^2 scaling used in the chosen flux visualization. In addition to the offset, this works SEDs especially predict the peak of the inverse Compton emission at higher energies. These significant discrepancies are, however, not entirely unexpected. While LST-1 is still in its commissioning phase and the optimal performance of all subsystems is not yet guaranteed, MAGIC has the advantage of already using a stereoscopic system. Consequently, these results need to be revisited once the LST-1 commissioning is finished and more telescopes of the CTAO LST subarray are available. It is, however, important to mention that all shown error estimates do not take into account systematics and are purely statistical. Possibly, once a handle on the telescopes systematics exists, the agreement between both experiments will increase, especially in the high energies.

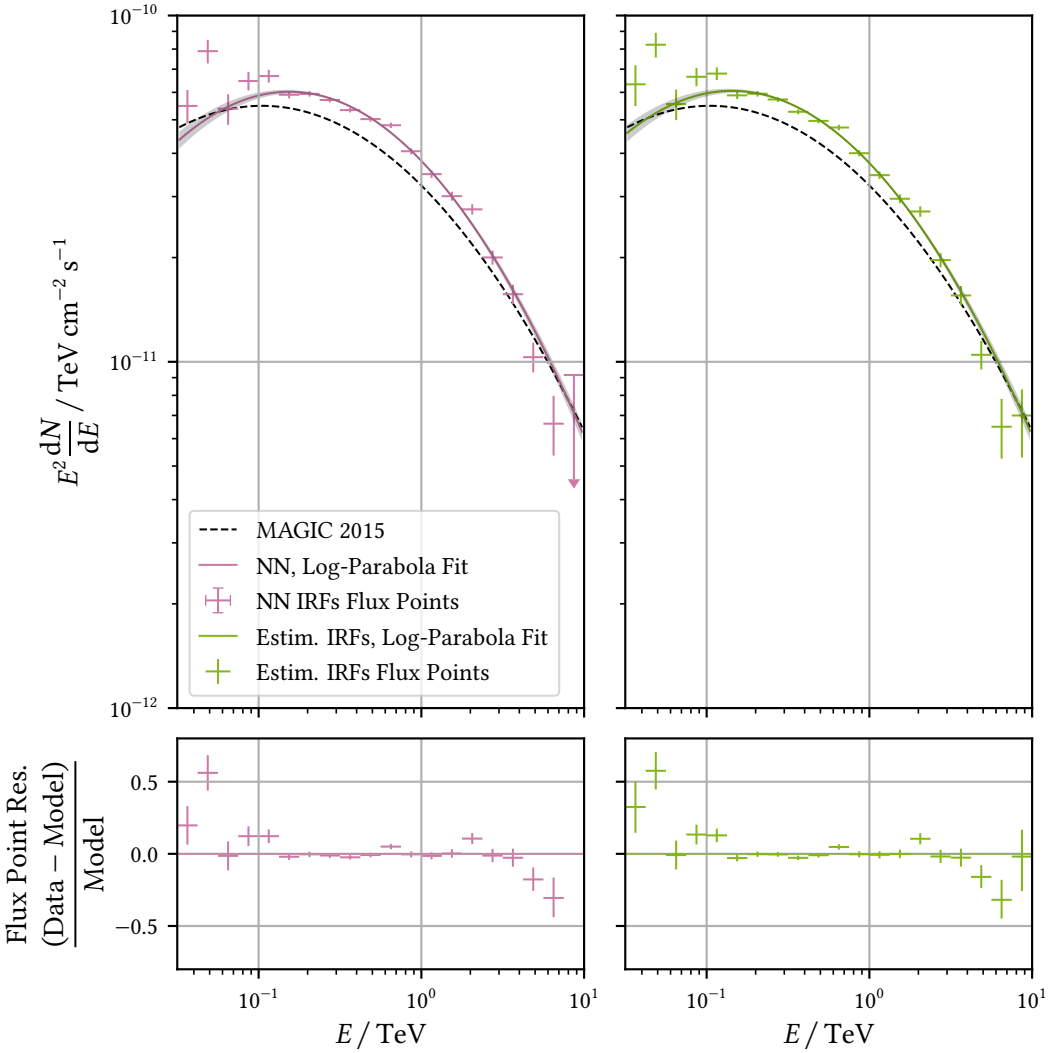

Figure 5.9: SEDs and flux points (upper panel) and residuals (lower panel) obtained using both nearest neighbor (left) and estimated IRFs (right) from 117 runs of Crab Nebula observations. For reference, the SED obtained from Equation 2.1 ([10]) is shown.

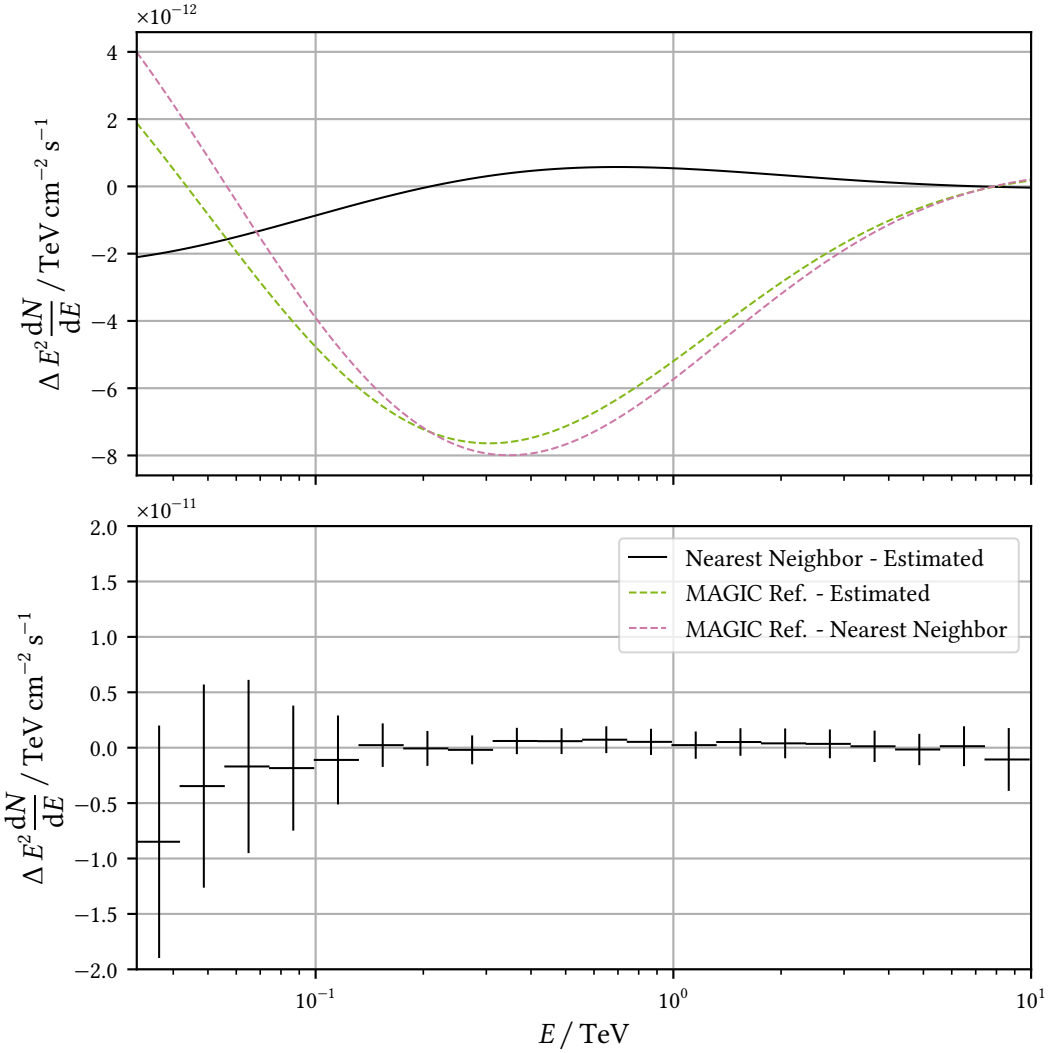

Figure 5.10: Difference between the Nearest Neighbor and Estimated IRF SEDs alongside the difference to the MAGIC reference (top) and the difference between the nearest neighbor and estimated IRF flux points (bottom). Errorbars in the lower panel from numerical error propagation assuming Gaussian errors and 10^7 draws each flux point.

Table 5.2: Results from estimating SEDs in analyses using both nearest neighbor (NN) and estimated (Estim.) IRFs.

Parameter	A	E_0	α	β
Meaning	Amplitude	Ref. Energy	Spectral Ind. at E_0	Curvature
Unit	$\mathrm{cm}^{-2}\,\mathrm{s}^{-1}\,\mathrm{TeV}^{-1}$	TeV		
Value (NN)	$3.342 \cdot 10^{-10}$	0.400	2.251	0.132
Error (NN)	$0.025 \cdot 10^{-10}$		0.009	0.007
Value (Estim.)	$3.313 \cdot 10^{-10}$	0.400	2.261	0.127
Error (Estim.)	$0.025 \cdot 10^{-10}$		0.009	0.007

To assess the agreement between this work's results and those obtained in the neighboring energy band, Figure 5.11 depicts the respective nearest neighbor and estimated IRF SED alongside flux points and a combined inverse Compton and log-parabola SED from 7.4 yr of *Fermi*-LAT operations. Evidently, this work's flux points tie in seamlessly with the *Fermi*-LAT results in both analyses. This finding is supported by the joint SED fit applied to the combined *Fermi*-LAT and LST-1 flux points between 2 GeV and 2 TeV, with the respective parametrizations in Table 5.3. A log-parabola SED can describe *Fermi*-LAT's medium-to-high and LST-1's low-to-medium energies in both instances. However, a fit including the full LST-1 energy range proved more complex, resulting in a less-matching SED. Given the simplicity of a log parabola and the complexity of fitting a SED over 4 orders of magnitude, this is to be expected. Consequently, using a more complicated SED model, e.g., by introducing an exponential cutoff at high energies, might be more justified. One could anticipate such an exponential cutoff to include the high energy flux points in Figure 5.11.

Table 5.3: Results from the joint SED fit using *Fermi*-LAT flux points and flux points from both nearest neighbor (NN) and estimated (Estim.) IRFs analyses.

Parameter	A	E_0	α	β
Meaning	Amplitude	Ref. Energy	Spectral Ind. at E_0	Curvature
Unit	$\mathrm{cm}^{-2}\,\mathrm{s}^{-1}\,\mathrm{TeV}^{-1}$	TeV		
Value (NN)	$3.281 \cdot 10^{-10}$	0.400	2.230	0.068
Error (NN)	$0.022 \cdot 10^{-10}$		0.012	0.003
Value (Estim.)	$3.259 \cdot 10^{-10}$	0.400	2.244	0.071
Error (Estim.)	$0.022 \cdot 10^{-10}$		0.012	0.003

In summary, the SED fitting was successful and provided reasonable results for both the nearest neighbor and estimated IRFs. Both results tie in with earlier results from *Fermi*-LAT, even though estimated fluxes lie slightly higher than those from MAGIC. The estimated IRFs proved to be well-usable substitutes for nearest neighbor IRFs. Similar results are thus to be expected from the following light curves.

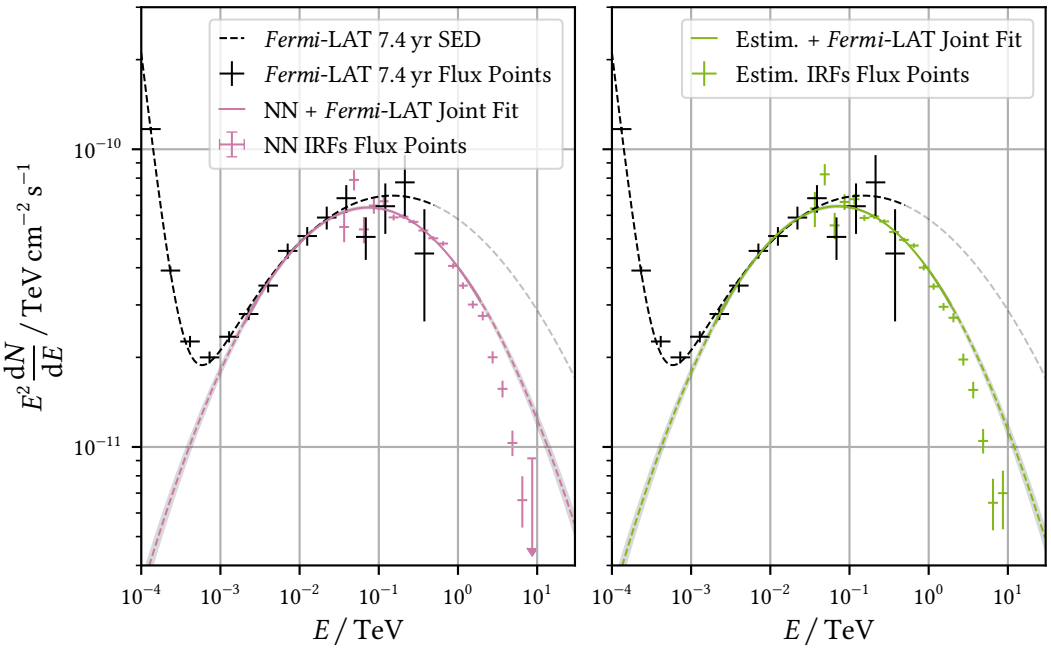

Figure 5.11: Joint log-parabola fit between 2 GeV and 2 TeV (indicated through the solid lines contrary to the dashed extension beyond that energy band) using flux points from 7.4 yr of *Fermi*-LAT Crab Nebula observations [18] and flux points from the nearest neighbor (left) and estimated IRF (right) analysis. For comparison, the *Fermi*-LAT SED is shown as a dashed, black line and extended beyond 500 GeV, indicated through higher opacity.

5.2.3 Obtaining Light Curves

As the final result of this Crab Nebula analysis, Figure 5.12 presents light curves obtained using both nearest neighbor and estimated IRFs. To account for typical fluctuations, the light curves were computed after stacking the observations of one observation night, which typically includes more than one run in each time bin. There are, however, occurrences where only one observation run with less than 20 min of observation time per observation night survived the selection criteria employed in [5] and is thus present in this work. Since the Crab Nebula is a bright source, even those short observation times allow for extracting an entry in the light curve. This is also eased by only considering one energy bin, integrating all energies above 100 GeV. Doing so, as discussed in [5], threshold effects near LST-1's lower energy boundary are eluded. Additionally, small fluctuations due to the changing position of the wobble positions are compensated above that energy.

As was expected from the previous results, deviations when comparing both analyses are minor. While the night-wise difference is compatible with zero for almost all entries, two values in early September 2021 defy this trend. As those two values were taken shortly after fixing LST-1's trigger settings in August 2021, span only one observation run, and were taken at a comparably high zenith angle of over 30 deg, numerous possible explanations exist for these deviations, not causing any concern. Besides that, both light curves show no signs of unexpected changes in the Crab Nebula spectral features, as is expected from this source. The computed best fit to constant flux model value, however, seems to either contradict the assumption of a constant flux or is derived from underestimated errors in the light curve values, as in both cases only about 50 % of the light curve values agree with the fitted model within their respective 1 σ intervals. While the former is definitively a possibility, even though the Crab Nebula is regarded as an extraordinarily stable source, it is imperative to state that the provided error bars in this light curve and, thus, the derived fit value only include statistical errors. Following the often found adding of a systematic error in quadrature to the statistical error, see, e.g., [5] and [10], a 5 to 5.5 % systematic error would suffice to raise the fit-to-data-point agreement rate to over 70 % and thus over the 1 σ containment of a Gaussian in the estimated or nearest neighbor analysis, respectively.

Comparing this analysis with the Crab Nebula reference obtained by MAGIC, the results are consistent with those obtained by comparing the SEDs earlier. The offset between the MAGIC value and this work's constant flux estimates is, ignoring the statistical model errors, at about 0.59 to 0.60 $\mathrm{cm}^{-2}\,\mathrm{s}^{-1}$, depending on the analysis, and thus on the order of 10 % of this work's results. As only few night-wise entries are compatible with the MAGIC reference and far more overshoot their value, this offset seems again to be systematical. The possible explanations are as with the SED deviations, and these analyses should, once more, be revisited once the LST-1 commissioning concludes and more LSTs are available. Besides these discrepancies, the performance of estimated IRFs is excellent and comparable to the nearest neighbor IRFs. It should again be mentioned that in the present IRF grid density and the overall observation conditions, deviations between both analyses are not expected and would, on the contrary, indicate technical problems with the estimated IRFs.

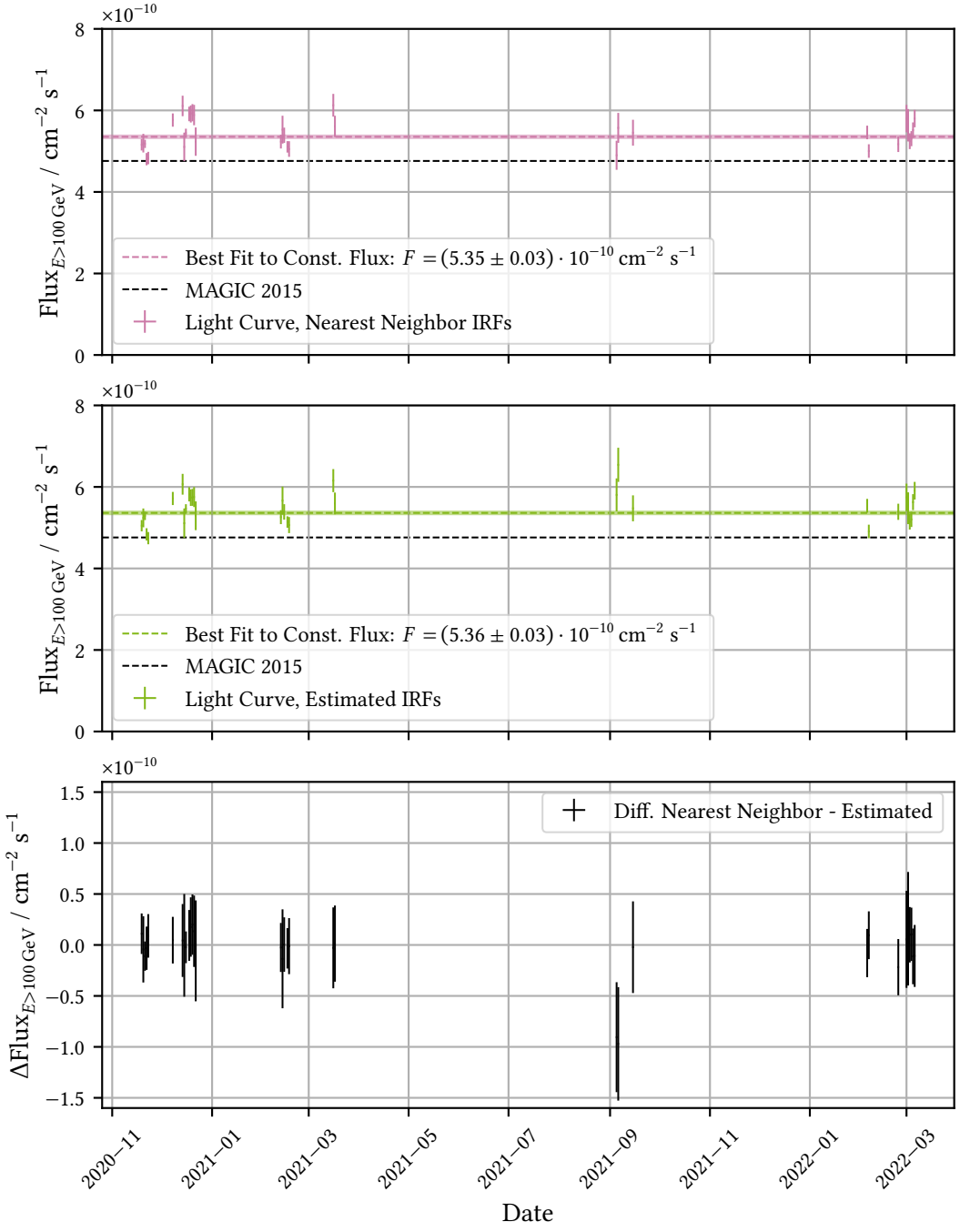

Figure 5.12: Night-wise light curves obtained using both nearest neighbor (top) and estimated IRFs (center) and 117 runs of Crab Nebula observations alongside the night-wise difference (bottom). Errorbars in the lower panel from numerical error propagation assuming Gaussian errors and drawing 10^7 samples per light curve data point. The best-fit value to a constant flux model is given alongside its statistical error in the respective panels. For reference, the MAGIC flux from Equation 2.2 (derived from [10]) is shown.

5.3 Dependence of the Analysis Results on the Grid Density

While the previous tests yielded negligible deviations between analyses using nearest neighbor and estimated IRFs, which was not unexpected due to the dense IRF grid spacing and has proven the correct performance of the estimated IRFs, a logical next step is to determine how far the estimation algorithms can compensate for a sparser grid. In case sparser grids can provide results of the same quality as dense grids with nearest neighbor IRFs, capacities for Monte Carlo simulations can be freed. Producing and processing these simulation files towards usable DL2 files requires tremendous computational resources and energy. Limiting the need for Monte Carlo simulations thus saves both financial and ecological resources, increasing the sustainability of modern, data-intensive experiments such as CTAO.

To test the quality of this work's estimation algorithms compared to nearest neighbor estimates, this chapter will repeat both Crab Nebula analyses on a set of the increasingly sparser IRF grids shown in Figure 5.13. While configurations A and B increase the interpolation distance inside the convex hull, configuration C increases the amount of points requiring extrapolation. For the computation of SEDs, the runs will analysed in the distance-to-nearest-neighbor bins shown in Figure 5.14. Due to the distance to the nearest neighbor changing drastically between the configurations, each binning was partially arbitrarily chosen to allow for sufficient runs and, thus, observation time in each bin. The direct comparison between the configurations must consequently be made carefully and does not allow for any strong statements to be made. However, the binning used for each configuration's nearest neighbor and estimated IRF analysis is the same, so comparing these two results is unproblematic and allows for assessing this work's algorithms. This caveat does not apply to the comparison of night-wise light curves, as no binning with respect to the nearest neighbor distance is applied there. All configurations use the same night-wise run binning for each data point in all light curves.

5.3.1 A High Statistic Case: Comparing SEDs

Comparing the SEDs obtained in the respective grid configurations, excluding extrapolation, as shown in Figure 5.15, reveals the apparent trend of an increased min-max range with increasing sparsity of the template nodes in the nearest neighbor IRF analysis, reaching a spread of half an order of magnitude in setting C. At the same time, estimated IRFs show minimal alterations from about 100 GeV onwards, and the results are exceptionally stable compared to nearest neighbor IRFs. For lower energies, both analysis types show a wide spread, regardless of the grid configuration, peaking at over half an order of magnitude in setting B. As these energies come close to the system's threshold energy, a complicated and non-linear behavior of the IRF components is expected, and the decreasing performance is thus anticipated. While the min-max ranges and thus the outliers, especially of the nearest neighbor IRF analysis, are widespread, both the mean and full-dataset SEDs (see Table 5.4) from both analysis types fall closely together up to setting B. This suggests some compensation of the outliers even in the nearest neighbor analysis, probably due to the immense amount of data used in the present analysis. All full-dataset SEDs, however, move away from the MAGIC reference with increasing sparsity.

This overall picture holds when including observations requiring extrapolation, as done in Fig-

ure 5.16. Especially in setting C, where the amount of extrapolated IRFs increases drastically as a node close to the turning of the Crab Nebula's trajectory is taken out of the template IRF dataset, the nearest neighbor analysis suffers greatly. While the min-max range, in this case, increases over all energies, indicating more extreme outliers, estimated IRFs can keep their consistency, showcaseing a sound performance of the used extrapolation algorithms in the present case. As, however, the full SED moves further away from both the MAGIC reference and the previous configurations results, caution is warrented. Consequently, setting C should be deemed too coarse for a reasonable analysis.

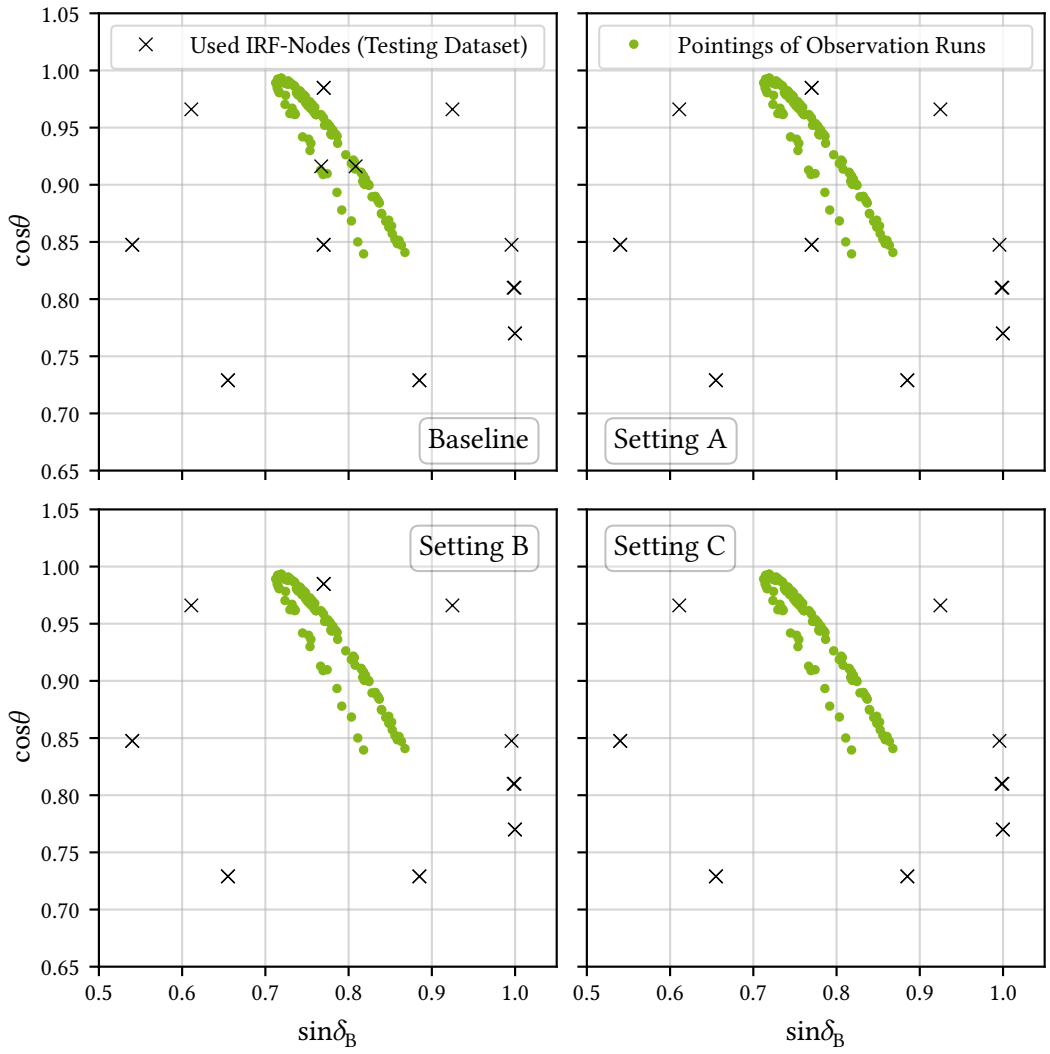

Figure 5.13: Baseline grid used for the previously presented Crab Nebula analysis (upper left), grid setting A without nodes at a zenith distance of 23 deg (upper right), grid setting B without nodes at zenith distances of 23 and 32 deg (lower left), and grid setting C without nodes at zenith distances of 10, 23 and 32 deg (lower right) alongside the positions of the used observation sample.

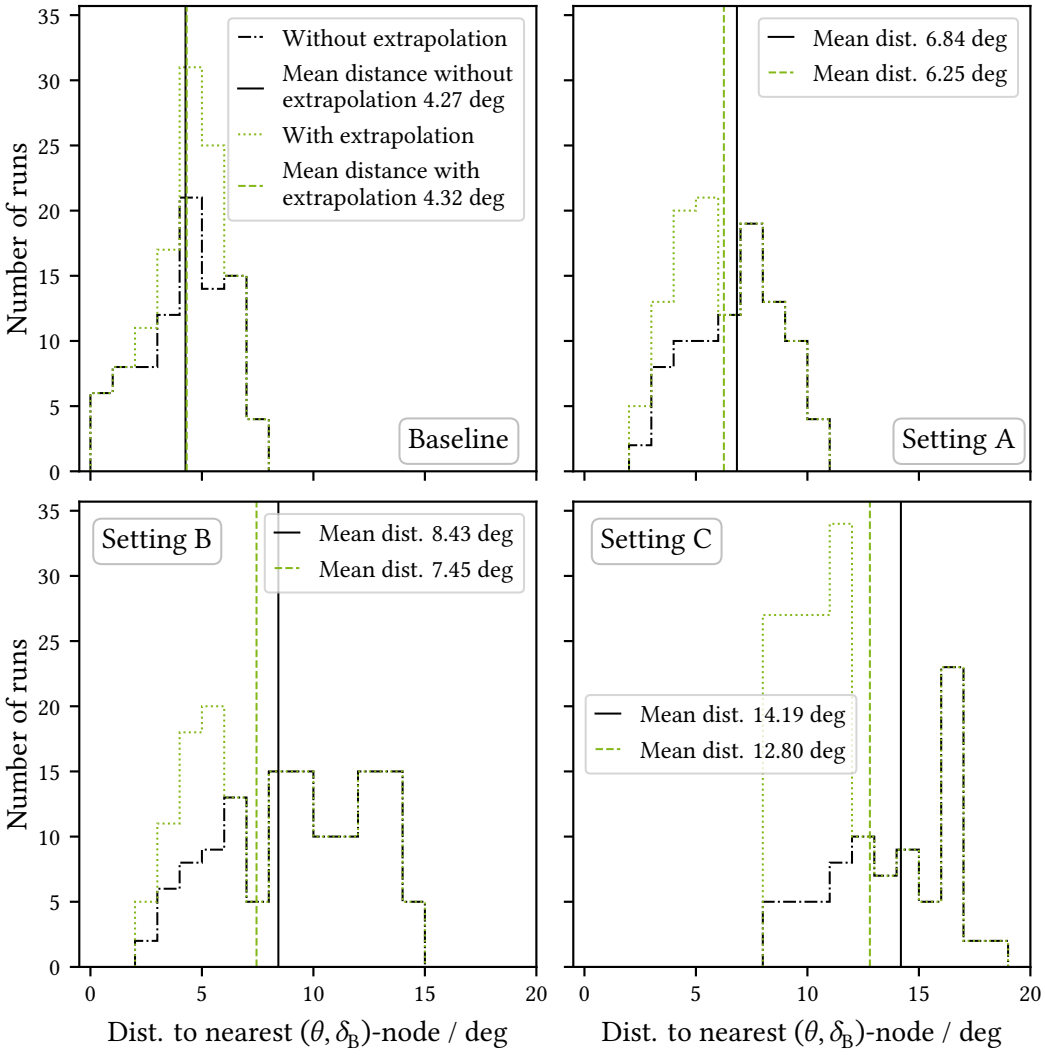

Figure 5.14: Binning of the used runs with respect to the nearest node for the baseline setting (upper left) and grid settings A (upper right), B (lower left), and C (lower right).

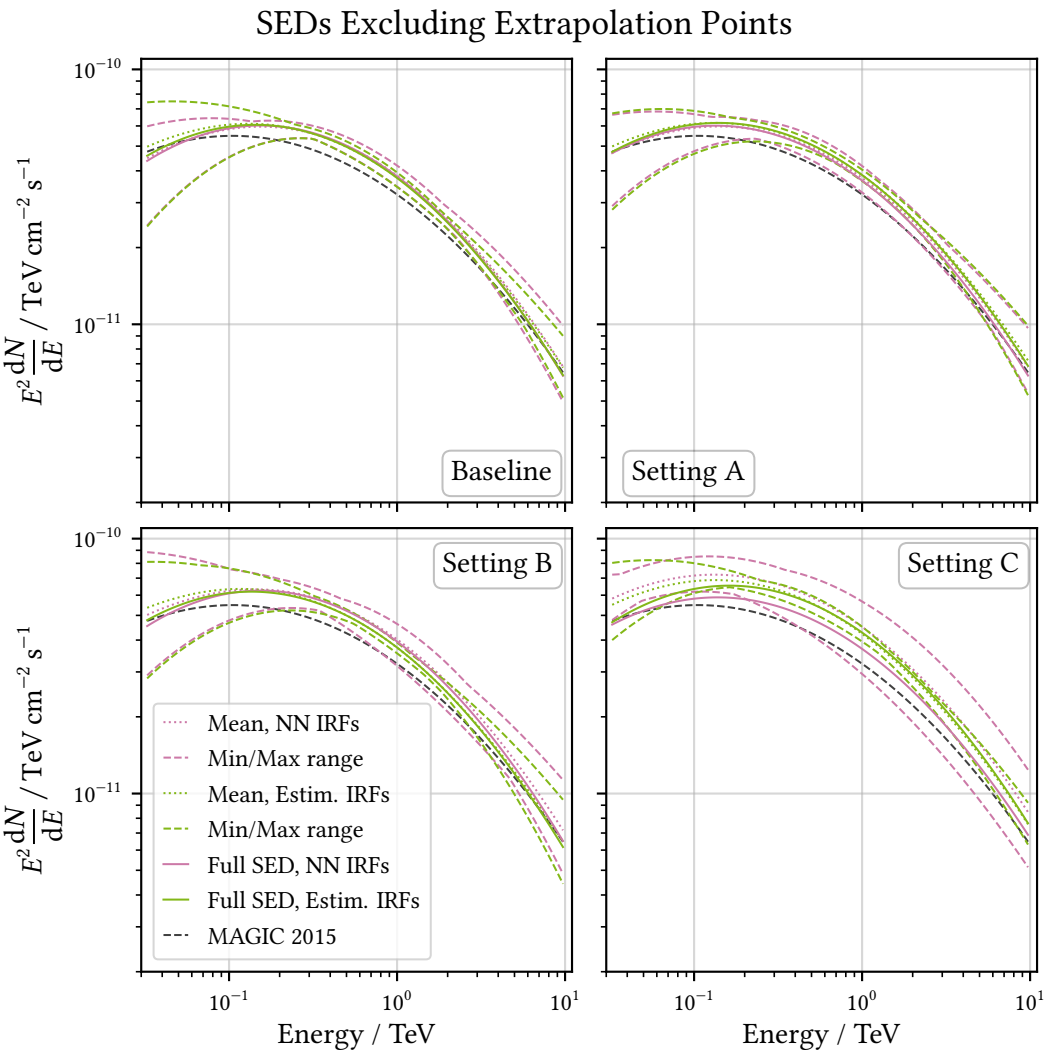

Figure 5.15: Comparison of the min-max range of the SEDs computed in each bin from Figure 5.14 from nearest neighbor and estimated IRFs excluding extrapolation points in the baseline configuration (upper left) and grid settings A (upper right), B (lower left), and C (lower right). All panels also include the SED computed from all observation runs without a binning dependent on the distance to the nearest node in the respective grid configuration, named "full" SED. The "mean" SED shows the mean computed from the ensemble of binned SEDs. For reference, the SED obtained from Equation 2.1 ([10]) is shown.

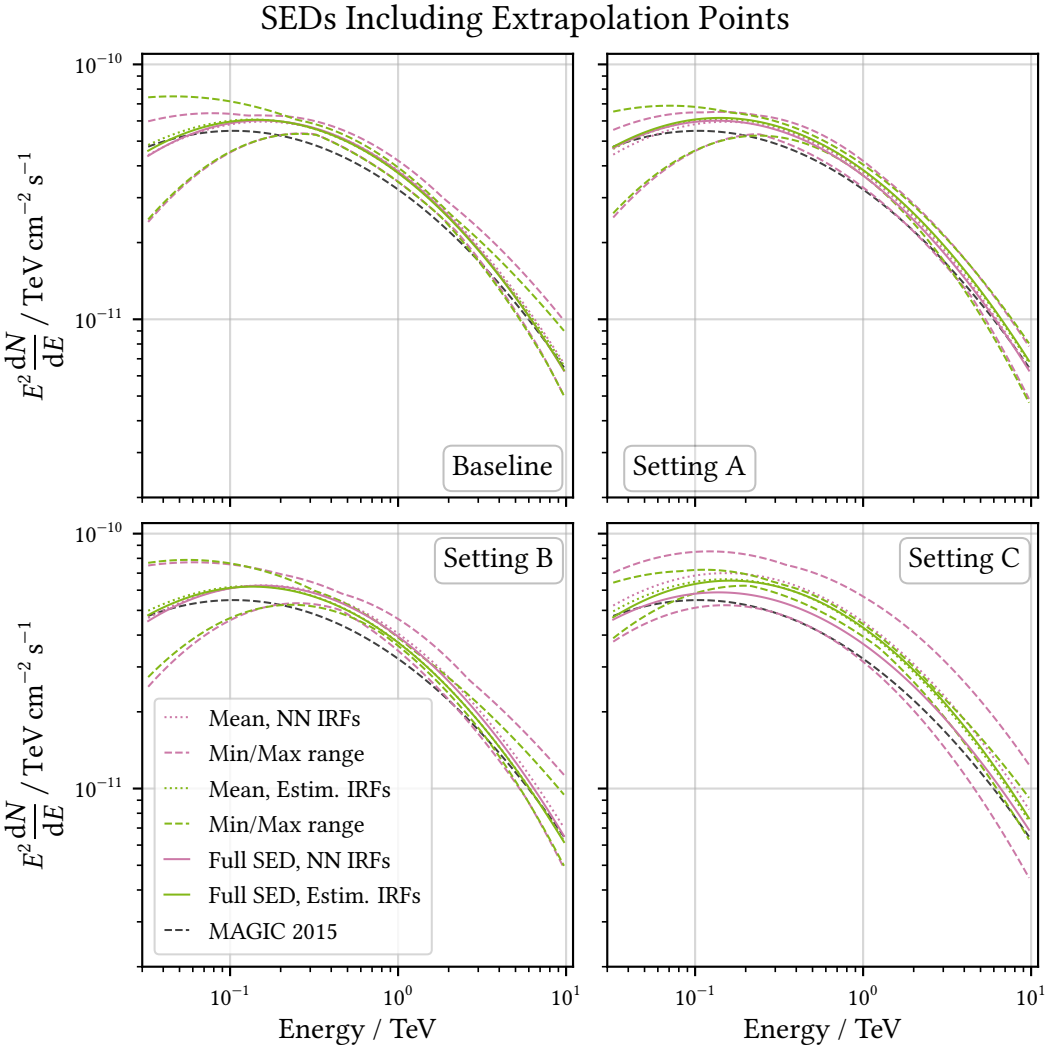

Figure 5.16: Comparison of the min-max range of the SEDs computed in each bin from Figure 5.14 from the nearest neighbor and estimated IRFs, including extrapolation points in the baseline configuration (upper left) and grid settings A (upper right), B (lower left), and C (lower right). All panels also include the SED computed from all observation runs without a binning dependent on the distance to the nearest node in the respective grid configuration, named "full" SED. The "mean" SED shows the mean computed from the ensemble of binned SEDs. For reference, the SED obtained from Equation 2.1 ([10]) is shown.

Table 5.4: Results from estimating SEDs in all grid configurations and using all events with nearest neighbor (NN) and estimated (Estim.) IRFs.

Config.	Parameter	A	E_0	α	β
	Meaning	Amplitude	Ref. Energy	Spectral Ind. at E_0	Curvature
	Unit	$\mathrm{cm}^{-2}\,\mathrm{s}^{-1}\,\mathrm{TeV}^{-1}$	TeV		
Base	Value	$3.342 \cdot 10^{-10}$	0.400	2.251	0.132
(NN)	Error	$0.025 \cdot 10^{-10}$		0.009	0.007
Base	Value	$3.313 \cdot 10^{-10}$	0.400	2.261	0.127
(Estim.)	Error	$0.025 \cdot 10^{-10}$		0.009	0.007
A	Value	$3.247 \cdot 10^{-10}$	0.400	2.269	0.123
(NN)	Error	$0.025 \cdot 10^{-10}$		0.009	0.007
A	Value	$3.371 \cdot 10^{-10}$	0.400	2.256	0.122
(Estim.)	Error	$0.026 \cdot 10^{-10}$		0.009	0.007
B	Value	$3.468 \cdot 10^{-10}$	0.400	2.251	0.132
(NN)	Error	$0.027 \cdot 10^{-10}$		0.009	0.007
B	Value	$3.339 \cdot 10^{-10}$	0.400	2.274	0.126
(Estim.)	Error	$0.026 \cdot 10^{-10}$		0.009	0.007
C	Value	$3.214 \cdot 10^{-10}$	0.400	2.253	0.118
(NN)	Error	$0.027 \cdot 10^{-10}$		0.010	0.008
C	Value	$3.682 \cdot 10^{-10}$	0.400	2.231	0.128
(Estim.)	Error	$0.029 \cdot 10^{-10}$		0.009	0.007

5.3.2 A Low Statistic Case: Comparing Night-Wise Light Curves

The notion of increasingly prevalent outliers in the nearest neighbor analysis carries over to the night-wise light curves in Figure 5.17. Compared to estimated IRFs, nearest neighbor IRFs result in an evidently wider spread of the light curve's points. Due to the Crab Nebula being regarded as an exceptionally stable source, this behavior is most likely not physical but a relict of using non-matching IRFs in the analysis. In contrast to the full-dataset SEDs discussed above, the limited observation time used in each entry of the presented light curves does compensate for the effects introduced by outliers. Consequently, estimated IRFs can express their full potential over the nearest neighbor analysis, producing fewer outliers and generally more stable results. However, this is not without limits, as can be seen in Figure 5.18, where the differences between the light curves from the baseline configuration and the settings A, B, and C are shown. While estimated IRFs allow for deviations compatible with 0 in settings A and B, this is not the case for setting C. In this configuration, even estimated IRFs start to systematically shift to flux higher values, even though to less of an extent than nearest neighbor IRFs, where no setting is without outliers. As extrapolation is numerically the more complicated scenario than interpolation, a worsening of the estimation performance is not unexpected, and a scenario like setting C should be avoided in real analysis cases as was already found when comparing the SEDs.

While nearest neighbor IRFs thus perform comparably to estimated IRFs given enough statistics to compensate for outliers, analyses conducted with inter- and extrapolated IRFs severely outperform the former ones in scenarios with limited observation time. One such analysis case will be presented in the following chapter with NGC 1275, and estimated IRFs will provide the superior analysis tool, following this chapter's results. In addition to outperforming in limited statistic cases, estimated IRFs simultaneously allow for sparser grids up to configurations as in setting B. As extrapolation proves to be more complicated, the amount of pointings where such estimations are needed should be minimized.

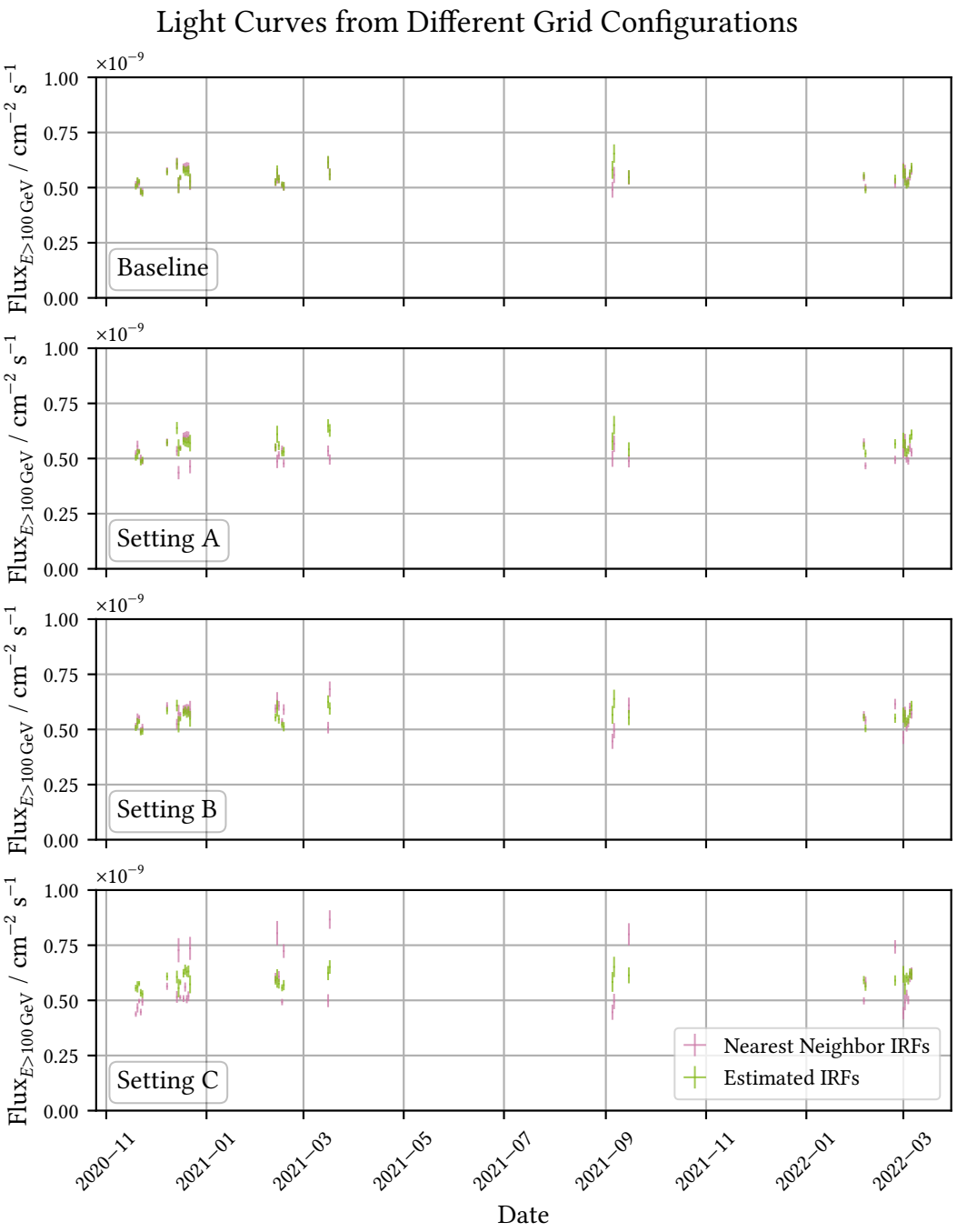

Figure 5.17: Comparison of the light curves from nearest neighbor and estimated IRFs in all configurations, from top to bottom: baseline, grid setting A, B, and C.

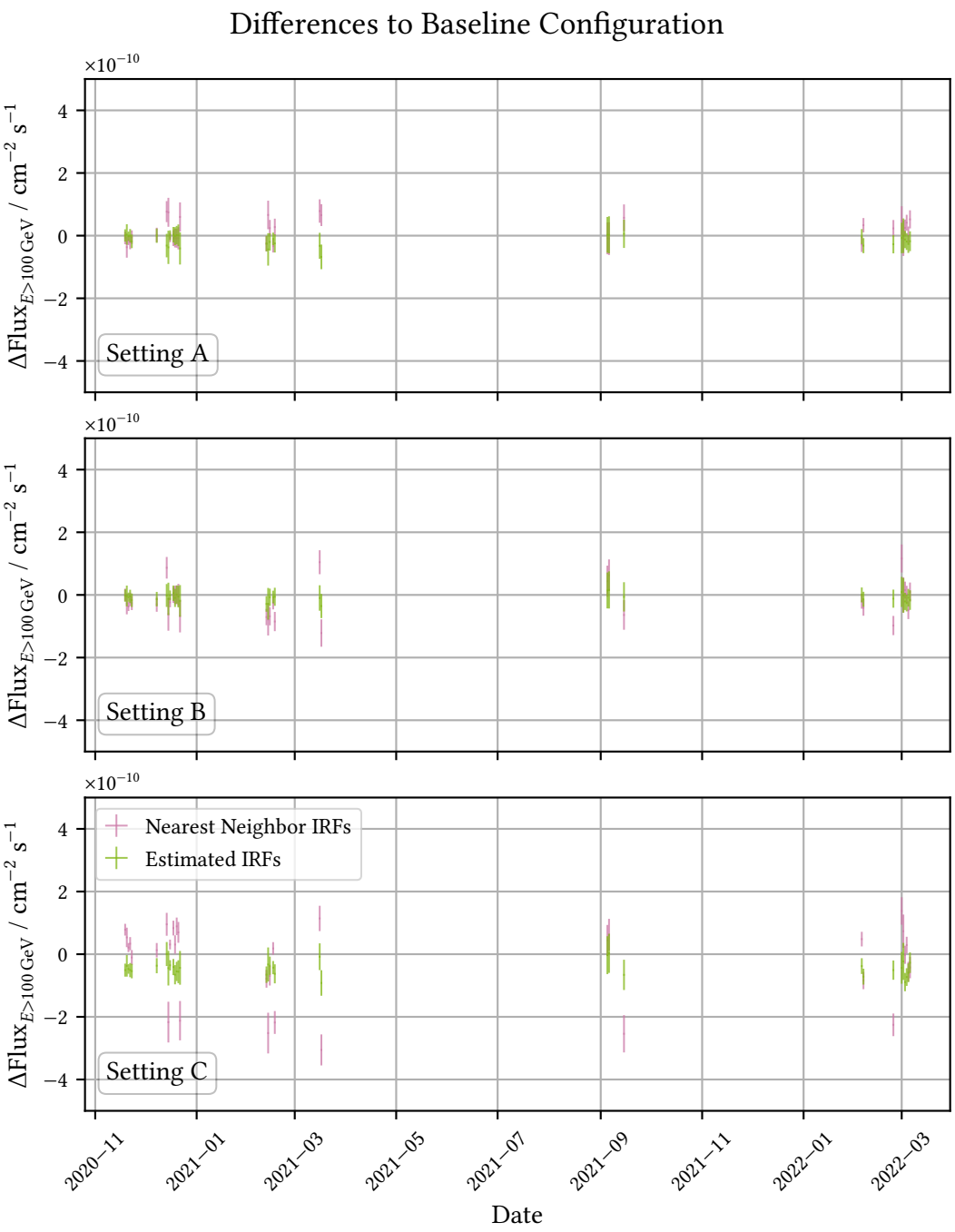

Figure 5.18: Difference of the light curves from Figure 5.17 with respect to the baseline configuration, from top to bottom: grid setting A, B, and C.

Analysis of the TeV Radio-Galaxy NGC 1275 in a Post-Flare State

6

With the principal usability of estimated IRFs and their superiority over nearest neighbor IRF analyses shown in the previous chapter using Crab Nebula observations with a zenith angle below 35 deg, the next step is to apply them to a real physics case. As introduced in subsection 2.1.1, NGC 1275 is a promising astrophysical source presenting multiple fascinating characteristics. This includes two flares reported through Astronomer's Telegrams (ATELs), the first in December 2022 by LST-1 [46], MAGIC [34], and MACE [133] and the second one in January 2023 by the MACE telescope [135]. Despite triggering a follow-up analysis for neutrino events by IceCube [81] and the flaring-series falling into a period of a reported brightness-increase at optical wavelengths [88], no reports of noteworthy *Fermi*-LAT NGC 1275 observations were found in this time-frame. The aim of this chapter is thus to analyze NGC 1275 observations taken at this time.

6.1 Data Selection

Contrary to the Crab Nebula analysis in the previous chapter, the available data must be preselected and is present only at DL1b, processed with some standard settings used with the default LST-1 analysis. The first step is thus the selection of suitable observation runs from the whole set of available observations. In the context of the abovementioned flaring events, data-taking lasted from December 20 to December 23, 2022. It was continued on January 9, 2023, one day before the second flare, for one observation run at difficult observation conditions, completed between January 13 and January 15, 2023. This baseline data amounts to 36 observation runs with a total observation time of 7.69 h.

The first selection cut on this data is applied to the highest zenith angle pointed to during the respective runs, as shown in Figure 6.1. As the Crab Nebula analysis was only performed on low zenith angle observations, all observations with a zenith angle over 35 deg are not considered for further analysis. NGC 1275 was only observed under a medium to high zenith angle on the night of the first flaring event. Consequently, this night is not considered for further analysis. One further run on December 24, 2022, was also taken at a zenith angle above the threshold. Following this selection step, 29 observation runs amounting to 6 h of observation time remain.

The second selection step aims to ensure dark observation conditions and, thus, low contamination by background light. The primary sources for this contamination are either the Sun not setting far enough below the horizon and, thus, atmospheric scattering remains significant or the Moon being over the horizon while being significantly illuminated by the Sun. Data-wise, a high level of background light would be found by a high deviation in the charges deposited in pedestal events, as

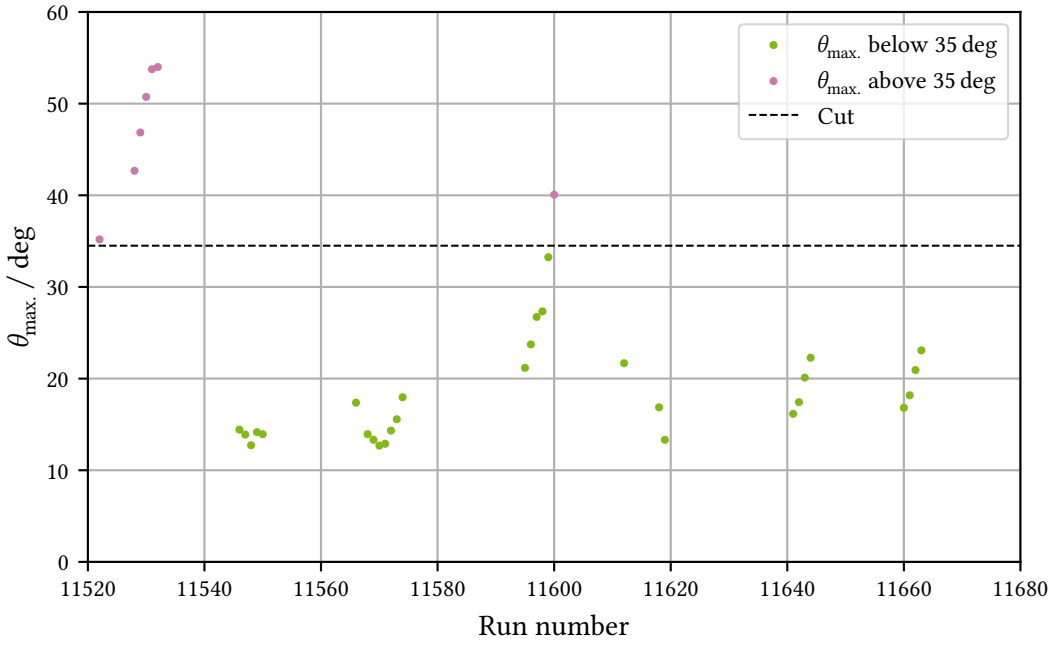

Figure 6.1: Maximal zenith angle per available run of NGC 1275 observation. Runs with a maximal zenith angle over 35° were removed from the dataset.

discussed in section 3.3, coincident with either celestial body being present in these configurations. No observation was conducted with the Sun being less than 20 deg below the horizon, and no coincidence between it being close to the horizon and high pedestal charge deviations were found. Consequently, no cut was applied with respect to its position. This is not the case for the Moon, as seen in Figure 6.2. Here, the one run observed on January 9, 2023, directly before the report of the second flare by the MACE experiment in the night from January 10 to 11, 2024, shows the undesired coincidence and is thus removed. This second flare fell into the so-called moon break, where observations are typically paused around full moon, which was only briefly interrupted by LST-1 trying to observe NGC 1275. As this was seemingly deemed unsuccessful during observation, LST-1 operations were only resumed on January 13, 2023, about three days after the second MACE ATEL's observation time. Discarding this observation run, 28 runs or 5.75 h of telescope operations remain.

To conclude the data selection, Figure 6.3 shows the trigger rate of physical events fulfilling the actual trigger conditions discussed in section 3.3 alongside the subset of events containing pulses of over 10 and 30 p.e. after the previous selection steps. The total trigger rate fluctuates between 6000 and 7000 s^{-1}, indicating normal and stable telescope operations and proper trigger settings. The same holds for those event rates with high charge depositions. Consequently, no further selection cuts were applied, concluding the data selection with the 28 from December 21, 2022, to January 15, 2023. The distribution of these run's observation times is shown in Figure 6.4. From the 5.44 h of actual observation time, about 56 % were taken in December 2022 and 44 % in January 2023. The finally selected observation runs are given in Listing 10 of Appendix B.

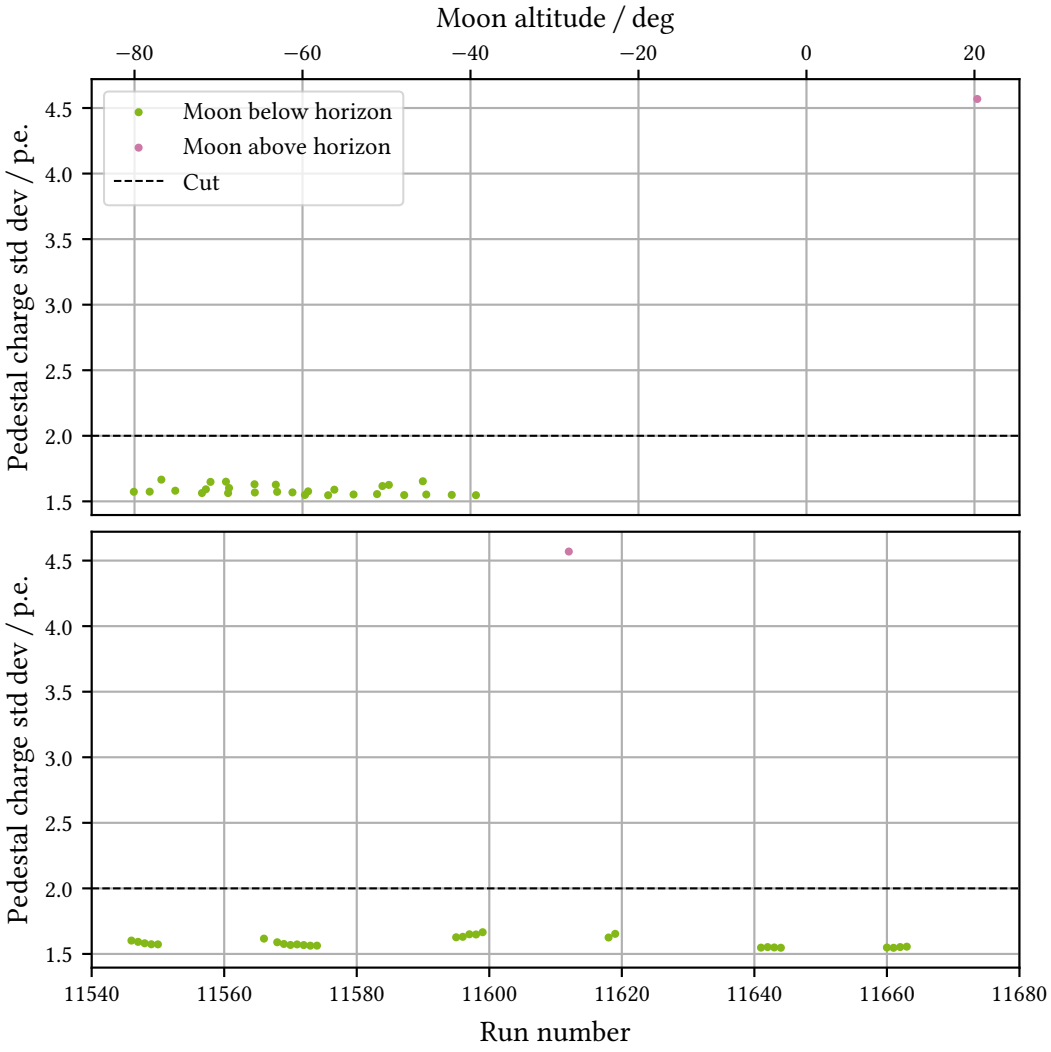

Figure 6.2: Standart deviation of the charge deposition in pedestal events (see section 3.3) with respect to the moon's altitude above the horizon (top) and per run (bottom) for all runs not discarded from the dataset after the zenith angle cut from Figure 6.1. A high deviation of the pedestal event charge indicates a high background light level that a simple offset cannot describe and, in the present case, coincident with high moonlight levels. Runs with a deviation over 2 p.e. were removed from the dataset.

As discussed in subsection 2.1.1, NGC 1275 is lies spatially close to the TeV radio-galaxy IC 310. It is important to mention that the used wobble positions omitted Perseus-MA, the central point between both sources. Thus, IC 310 does not fall into the following analysis' background regions.

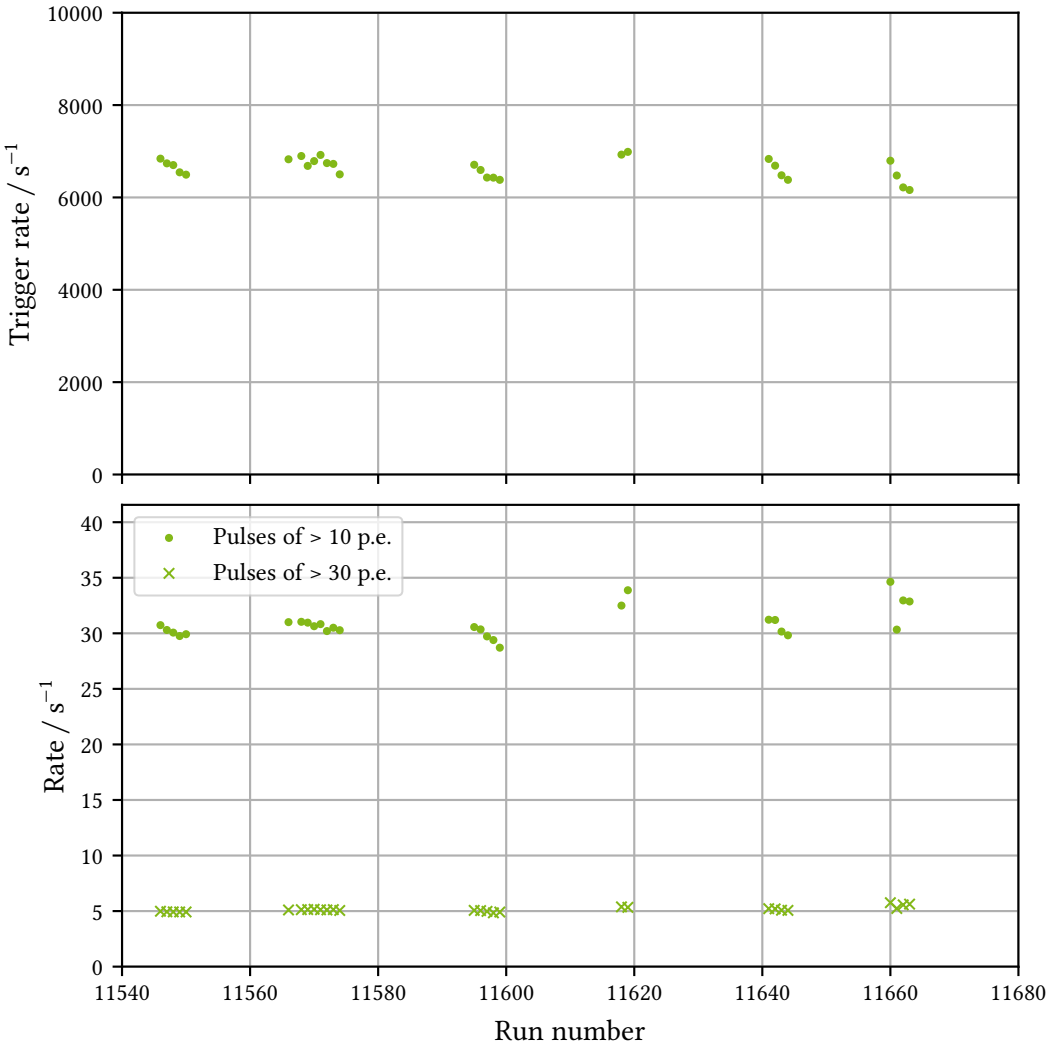

Figure 6.3: Rates of triggered events classified as physical (top) and the rates of the subset of these events with a deposited charge over 10 and 30 p.e. (bottom) for all runs not discarded from the dataset after the zenith angle (Figure 6.1) and pedestal charge deviation (Figure 6.2) cuts.

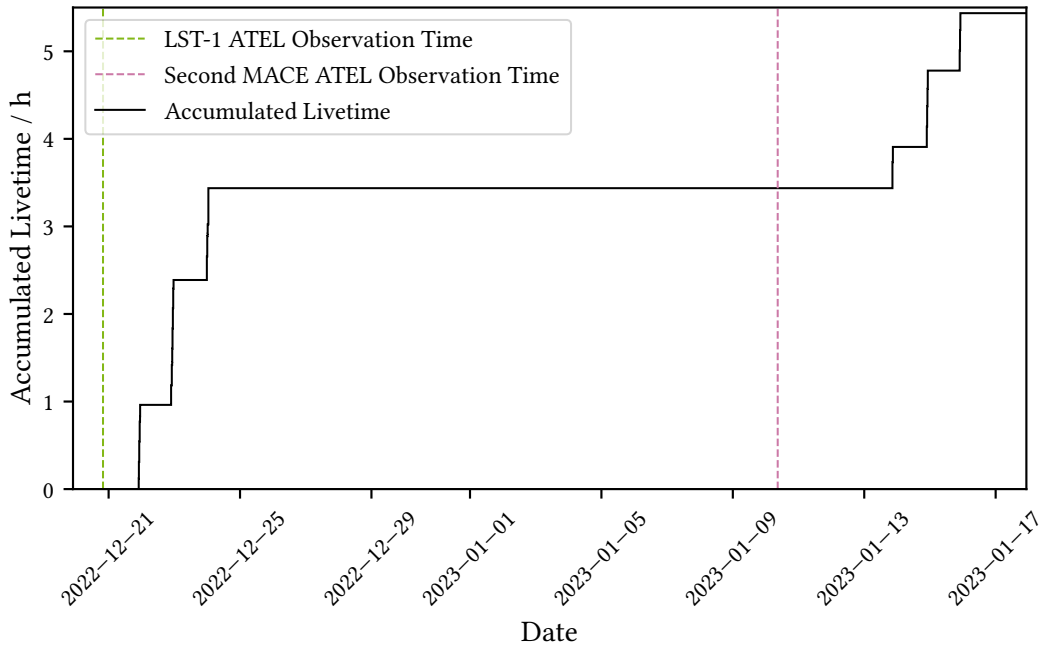

Figure 6.4: Cumulative distribution of the dead-time corrected measurement time used for the presented NGC 1275 analysis, accounted for deadtime. The observation times of the two ATELs from December 2022 [46] and January 2023 [135] are highlighted.

6.2 Preprocessing up to DL2 and Analysis Configuration

While the Crab Nebula analysis could be started at DL2, the used data is only available at DL1b. Thus, the reconstruction of the needed properties particle type, energy, and origin using machine learning methods was not yet conducted. To stay close to the use case for estimated IRFs, analyses on short time scales using standard settings, no specialized random forests were trained, and existing models were used. As shown in Figure 3.6, the simulations for these models lie on a training declination line. For this NGC 1275 analysis, models trained on the 34.76 deg line were used. The actual observed DL1b files were processed with the configuration used to train the machine learning models and are shown in Listing 4 of section A.2.

For the DL2 to DL3 processing step, the configuration matches the one used in the Crab Nebula analysis. Only the intensity cut was lowered to a value of 50 p.e., as all data was taken after the trigger settings were fixed, as discussed in [5]. The corresponding configuration file is given in Listing 5 of section A.2. As with the Crab Nebula analysis, the high-level analysis also utilizes point-like IRFs with energy-dependent gamma-hadroness cut and θ_{cut} tables with efficiencies and containments of 70 %. The SED was fitted between 80 GeV and 5 TeV to follow a log-parabola with starting values as given in Table 6.1, and 10 flux points between 100 GeV and 1 TeV were extracted. The reference energy E_0 has been kept fixed and was thus not optimized. As a MAGIC analysis of

a NGC 1275 flare in 2017 [17] provided the best results when an exponential cutoff power law

$$N(E) = A\left(\frac{E}{E_0}\right)^{\Gamma} \exp\left(-\lambda E\right) \tag{6.1}$$

with spectral index Γ and cutoff energy $E_{\text{cut.}} = \lambda^{-1}$ at a fixed reference energy E_0 was used, this SED model was also considered with starting values as in Table 6.2. For the light curve, one night-wise energy bin above 100 GeV was computed. The configuration files are shown in Listing 5 to 8 of section A.2. As for the Crab Nebula analysis, these configurations partially rely on defaults.

Table 6.1: Starting values for the minimization used to derive the NGC 1275 log-parabola SEDs as in Equation 2.7

Parameter	A	E_0	α	β
Meaning	Amplitude	Ref. Energy	Spectral Ind. at E_0	Curvature
Value	1×10^{-11}	0.3	2	0.1
Unit	$\text{cm}^{-2}\,\text{s}^{-1}\,\text{TeV}^{-1}$	TeV		

Table 6.2: Starting values for the minimization used to derive the NGC 1275 exponential cutoff power law SEDs as in Equation 6.1

Parameter	A	E_0	Γ	$\lambda = 1/E_{\text{cut.}}$
Meaning	Amplitude	Ref. Energy	Spectral Ind.	Inv. Cutoff Energy
Value	1×10^{-12}	0.3	2	0.1
Unit	$\text{cm}^{-2}\,\text{s}^{-1}\,\text{TeV}^{-1}$	TeV		TeV^{-1}

6.3 Analysis Results

Contrary to the Crab Nebula analysis presented in the previous chapter, the reported flaring activity leads one to expect differences between the single runs. While the amount of observations available is too low to expect a significant night-wise observation, a grouping of the observations in post-first and post-second flare seems promising and will be applied.

6.3.1 θ^2 Plots and Excess Significances

Starting again with θ^2 distributions, shown in Figure 6.5 both for the time bins and cumulated, an apparent excess is visible close to the catalog position of NGC 1275. While the excess rates are naturally lower than those obtained for the Crab Nebula, given less observation time and a dimmer source, the corresponding significances after the second flare and for the cumulated events lie over $5\,\sigma$. Even though the significance from the first flare observations falls slightly below the $5\,\sigma$ threshold, it is well above the $3\,\sigma$ threshold, rendering a random fluctuation unlikely. Consequently, both time bins are expected to yield good results. Tests aiming to separate the first flare's observations to isolate December 21 from the following two days, trying to analyze changes in NGC 1275's SED to greater detail, yielded significances below $3\,\sigma$. This idea was consequently dismissed.

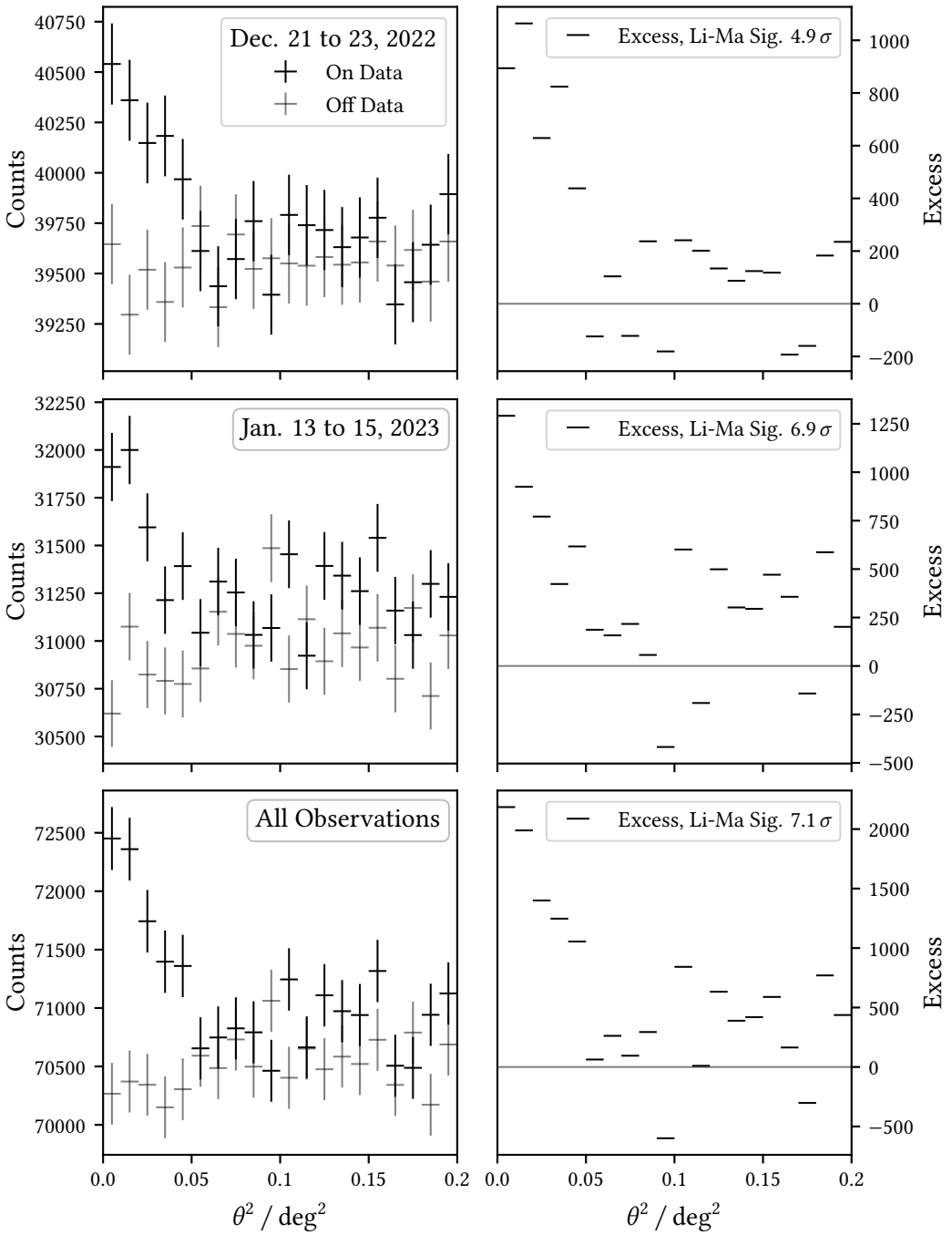

Figure 6.5: Left Side: θ^2 plots of observations from December 21 to 23, 2022 (top), January 13 to 15, 2023 (center), and the cumulated observations (bottom). Right Side: Corresponding excess plots with Li-Ma significance according to Equation 3.1.

6.3.2 SED Modeling

The results of the SED fitting for the two time bins are shown in Figure 6.6 with a log-parabola and Figure 6.7 from the exponential cutoff power law introduced in Equation 6.1 above. The parametric fitting results are given in Table 6.3 and Table 6.4, respectively. Both time bins and both model types yield fluxes in the same order of magnitude, with the exponential cutoff power law being, as the name suggests, cut off and consequently not extending to energies as high as the log-parabola. Given that the January 2023 observations were taken with considerably higher delay to the corresponding flare than the December 2022 ones due to the moon break, this consistent flux level is quite interesting. It might either indicate that NGC 1275 remained in a stable flux state for some time after the flare, a faster "cool-off", or a higher overall rise in the second flare. Comparing the SEDs with an earlier MAGIC analysis of the 2017 NGC 1275 flaring event [17], the flux levels fall well between the post-flare and low state observed both by optical inspection and when comparing the parametric fit values. This behavior is expected due to the flare follow-up nature of the used observations. In this regard especially a more finely resolved analysis of the first flare's observations, including the high-zenith observations taken directly after the flare, should be pursued to further study the spectral evolution.

The computed flux points show a high consistency with the models, indicating stable SED fit performances. Nevertheless, all models resulted in only upper limits at energies approaching 1 TeV, given the steep decline of the flux and the limited observation time. Thus, a detection of NGC 1275 as a TeV source cannot be claimed in either time bin.

Compared to the Crab Nebula analysis results, both model and flux point error estimates are considerably higher, most probably due to lower statistics. This becomes even more evident when looking at the parametric values in Table 6.3 and Table 6.4 and comparing the error estimated to, e.g., Table 5.4. In this NGC 1275 analysis, some relative error estimates go as high as or even higher than 50 %, while in the Crab Nebula case, relative errors are in the order of a few per thousand. This impressively showcases the influence of observation time and statistics on the results. Comparing this work's error estimates to those of the MAGIC reference, whose error relative estimates are also at most in the order of around 10 %, again makes this analysis' errors seem extreme. It is, however, important to state that their observations comprised a higher total observation time, stating around 1 to 3 h per night and utilizing a stereoscopic system yielding more information per event and thus should allow for a better reconstruction. While the exact amount of their follow-up observation time is not stated in the publication, it is probable to assume they observed at the higher end of this span in a flare or post-flare setting. Adding to these high error estimates, as already stated in the Crab Nebula analysis, it is essential to mention that this analysis' error estimates are purely statistical. Even more significant error estimates have to be expected if, at some point, systematical errors can be accounted for.

The combined SEDs of Figure 6.8 follow the same description as the time binned discussed above; the parametric values derived in the analysis are given in the abovementioned tables. For both SED types, the result falls again between the MAGIC post-flare and low state, and the combined models agree well with the time-resolved ones. Given the combined amount of observations, the error estimates are, as would be expected, smaller but still considerable compared to both the Crab Nebula and MAGIC analysis, even though the total observation time should at least come close to

those used by MAGIC for their post-flare result. The increased statistic allowed for the computation of actual flux points over the whole analyzed energy range and resulted in no upper limits. Again, the flux points indicate stable fit results due to their high consistency with the model. While the flux points estimated for the exponential cutoff power law fall slightly closer towards the model expectation when considering only the nominal values, all points agree within their respective errors. As far as the comparison to the previous post-flare SEDs is valid to assess the performance of the estimated IRFs used here, the latter result in a good compatibility with literature, confirming the sound performance of the used estimation principles.

Table 6.3: Results from fitting log-parabola SEDs the NGC 1275 observations.

Parameter	A	E_0	α	β
Meaning	Amplitude	Ref. Energy	Spectral Ind. at E_0	Curvature
Unit	$\mathrm{cm}^{-2}\,\mathrm{s}^{-1}\,\mathrm{TeV}^{-1}$	TeV		
Value (Dec. 22)	$2.11 \cdot 10^{-10}$	0.30	3.12	0.80
Error (Dec. 22)	$0.21 \cdot 10^{-10}$		0.18	0.28
Value (Jan. 23)	$1.56 \cdot 10^{-10}$	0.30	3.17	0.73
Error (Jan. 23)	$0.24 \cdot 10^{-10}$		0.27	0.40
Value (Full)	$1.87 \cdot 10^{-10}$	0.30	3.14	0.77
Error (Full)	$0.16 \cdot 10^{-10}$		0.15	0.23

Table 6.4: Results from fitting exponential cutoff power law SEDs the NGC 1275 observations.

Parameter	A	E_0	Γ	$\lambda = 1/E_{\mathrm{cut.}}$
Meaning	Amplitude	Ref. Energy	Spectral Ind.	Inv. Cutoff Energy
Unit	$\mathrm{cm}^{-2}\,\mathrm{s}^{-1}\,\mathrm{TeV}^{-1}$	TeV		TeV^{-1}
Value (Dec. 22)	$7.81 \cdot 10^{-10}$	0.30	1.60	4.44
Error (Dec. 22)	$4.49 \cdot 10^{-10}$		0.55	1.69
Value (Jan. 23)	$4.97 \cdot 10^{-10}$	0.30	1.81	3.93
Error (Jan. 23)	$3.97 \cdot 10^{-10}$		0.78	2.33
Value (Full)	$6.48 \cdot 10^{-10}$	0.30	1.69	4.22
Error (Full)	$3.09 \cdot 10^{-10}$		0.46	1.40

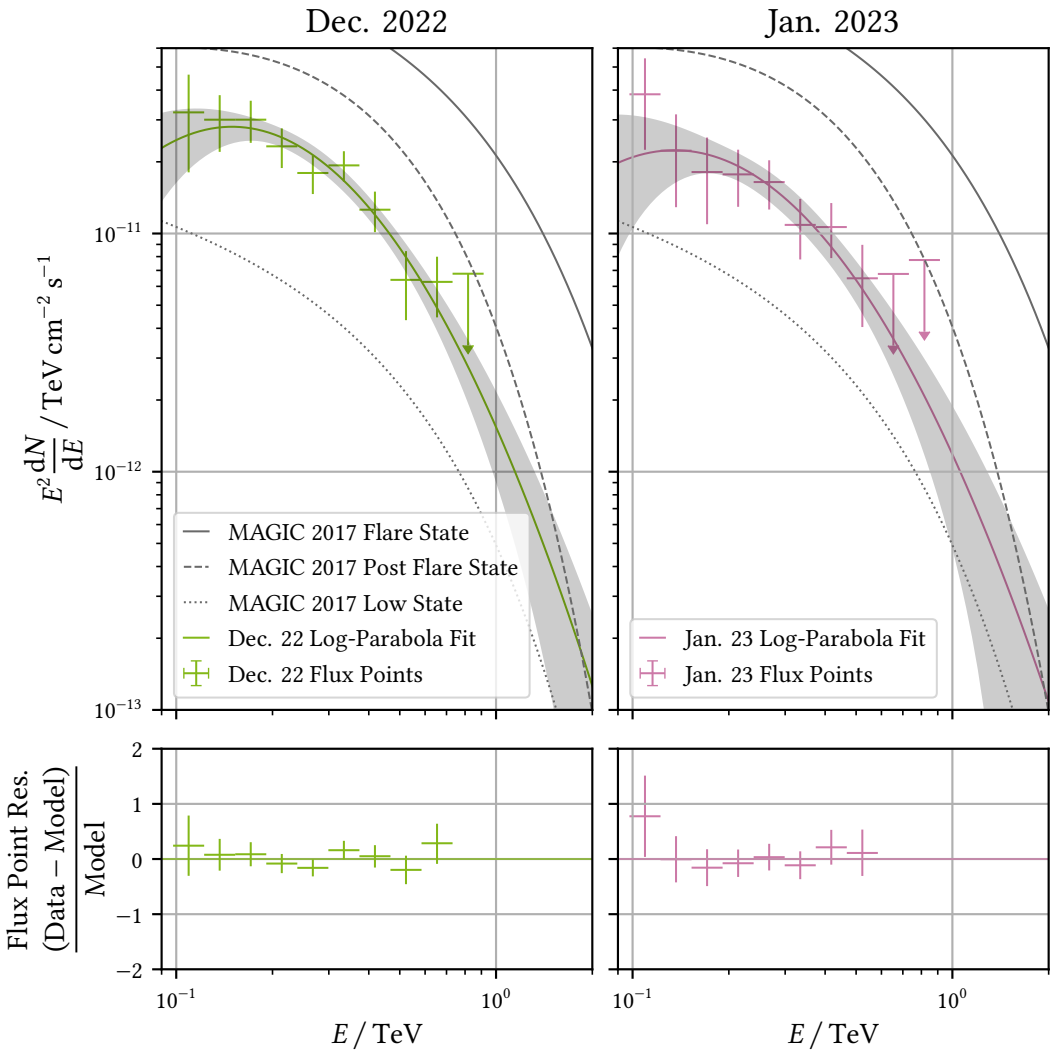

Figure 6.6: NGC 1275 log-parabola SEDs as in Equation 2.7 with flux points (top) and corresponding residuals (bottom) computed using observations from December 21 to 23, 2022 (left), January 13 to 15, 2023 (right). Results from a 2017 MAGIC analysis [17] of a previous NGC 1275 flare are given as a reference.

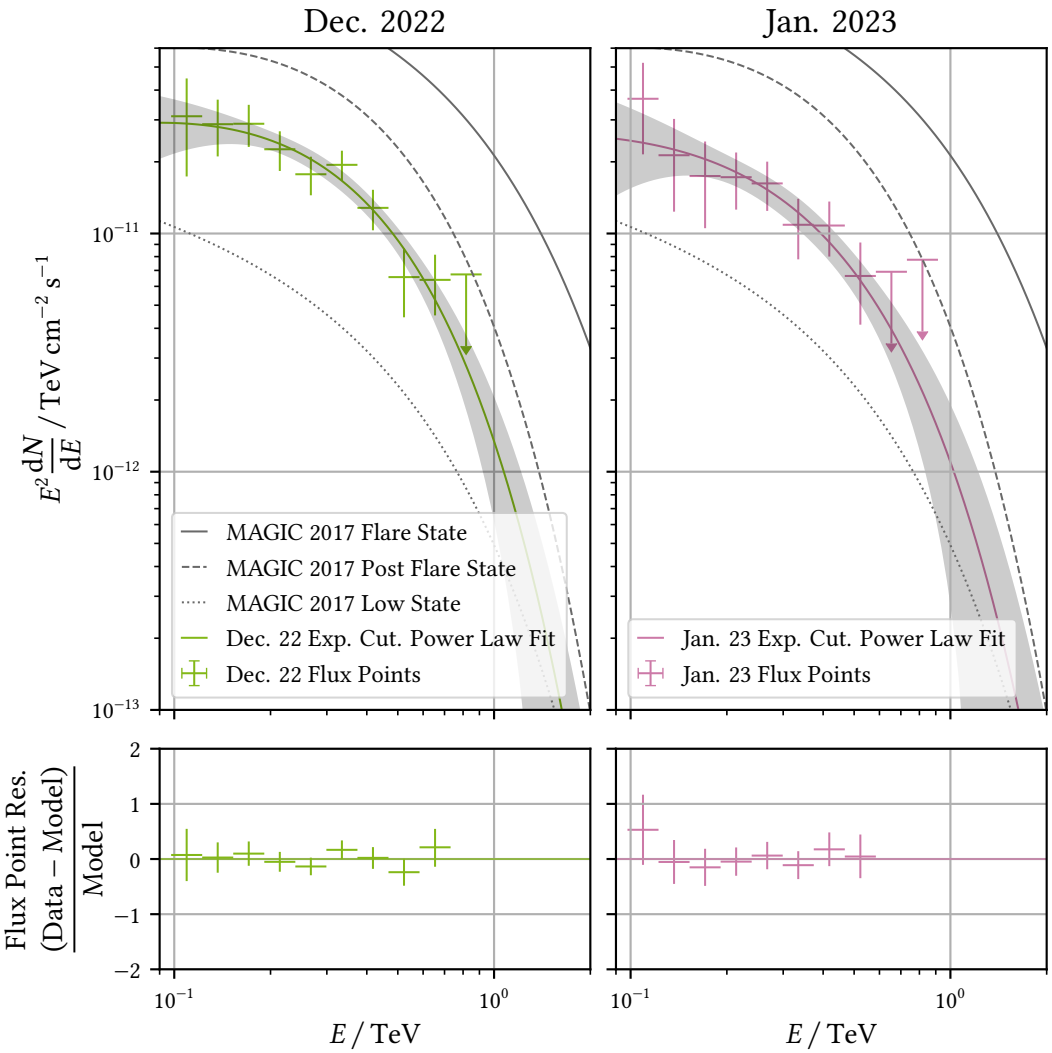

Figure 6.7: NGC 1275 exponential cutoff power law SEDs as in Equation 6.1 with flux points (top) and corresponding residuals (bottom) computed using observations from December 21 to 23, 2022 (left), January 13 to 15, 2023 (right). Results from a 2017 MAGIC analysis [17] of a previous NGC 1275 flare are given as a reference.

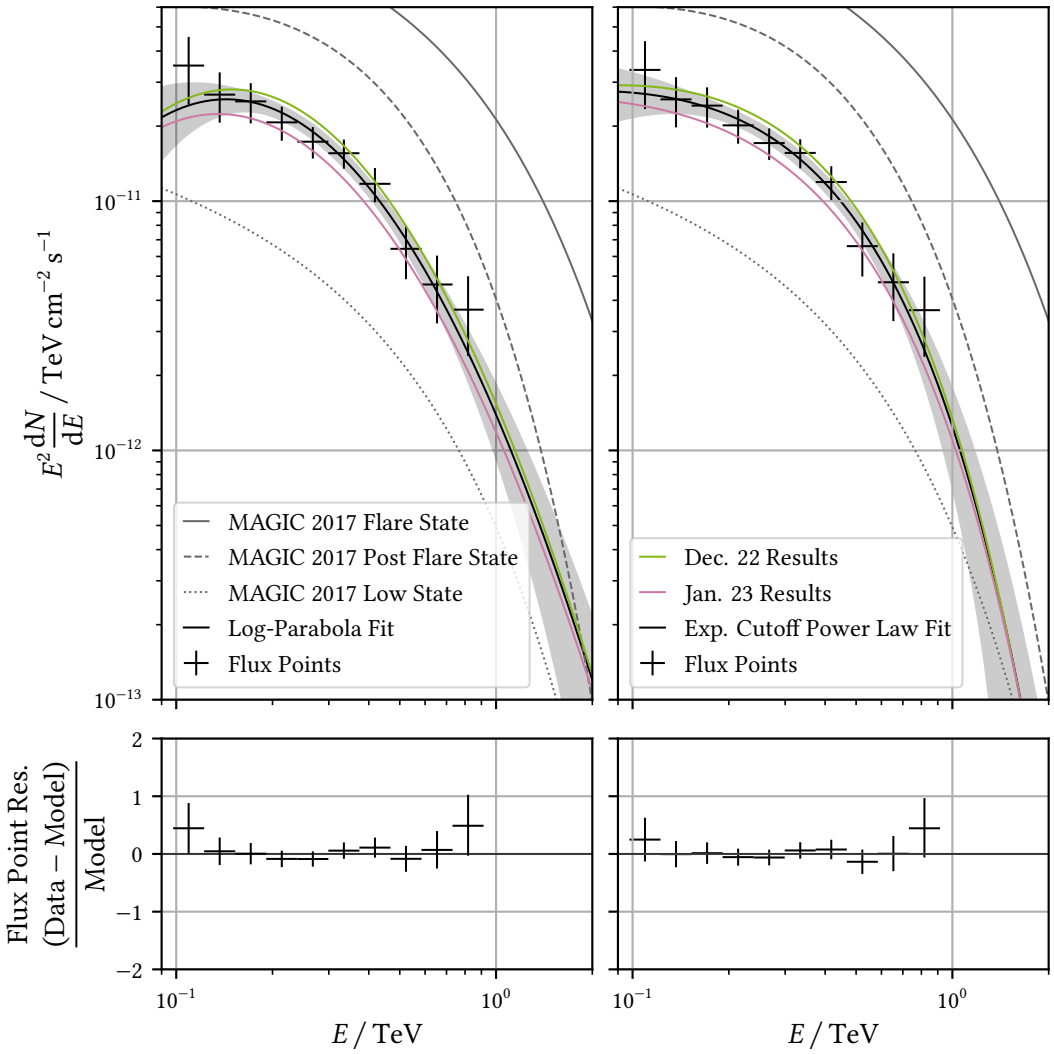

Figure 6.8: NGC 1275 SEDs from a log-parabola (left) and exponential cutoff power law (right) model with flux points (top) and corresponding residuals (bottom) computed using all 28 selected observation runs. The SEDs from Figure 6.6 and Figure 6.7, alongside results from a 2017 MAGIC analysis [17] of a previous NGC 1275 flare, are given as references.

6.3.3 Light Curves

With the good agreement between the December 2022 and January 2023 measurements on the one hand and both of these time-bins with the combined SED on the other, it is reasonable to compute the night-wise light curve using the combined model for better comparability. The resulting light curves above 100 GeV from both the log-parabola and exponential cutoff power law SEDs are shown in Figure 6.9. As expected from the comparable performance of both SED model types, the respective light curve points also fall closely together and agree within their error estimates.

The light curves show an apparent decrease in the flux level after the first and second flare, as expected in such a scenario. Again, it is surprising to find the second flare follow-up at the same flux level as the first one despite the higher time delay. Even though they were taken multiple days after the respective flares, the light curves peak at about half the Crab Nebula flux found in Figure 5.9. Compared to the post-flare state from 2017 [17], for which the MAGIC telescopes observed NGC 1275 in the two nights following a flare night, the comparable follow-up of the first flare peaks at about 60 % of the 2017 reference flux. However, the development in the days after the flare is comparable to the light curve computed by MAGIC in 2017. There, they also found a stable flux level on the first and second night after the flare, followed by a significant decrease on the third night. The third night of both the December 2022 and January 2023 observations is in agreement with the low state reported by MAGIC, indicating an end to the respective flare states.

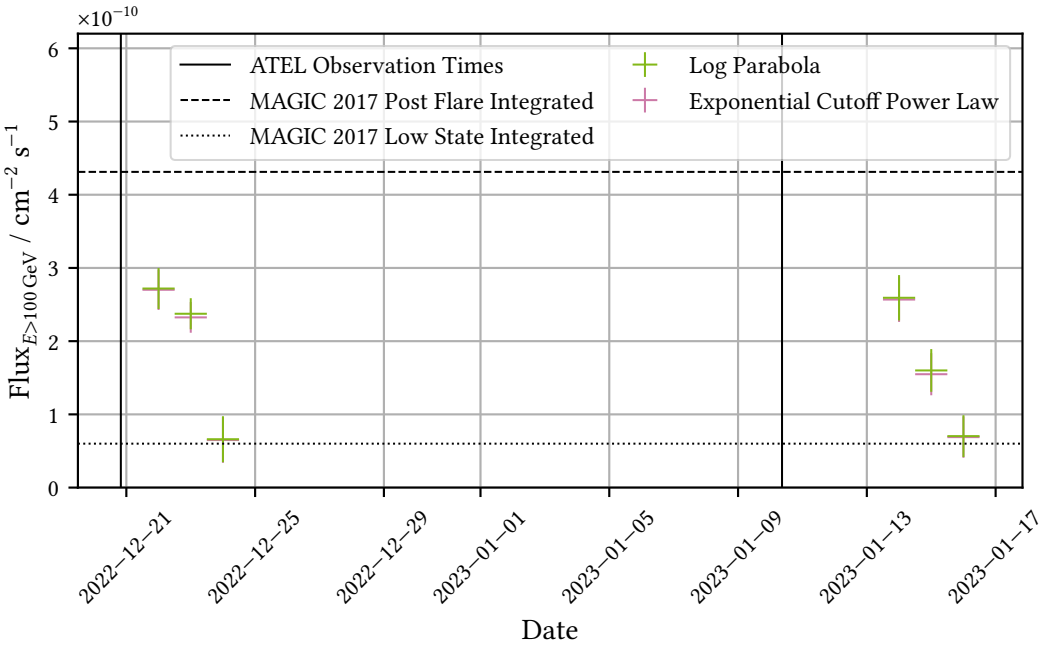

Figure 6.9: Light curves computed from night-wise NGC 1275 observations using the log-parabola and exponential cutoff power law SEDs computed from the total 28 observation runs, as shown in Figure 6.8. The integral fluxes computed from the 2017 MAGIC [17] analysis results in the low and post flare state are given as reference, the observation times of the 2022 LST-1 [46] and the 2023 MACE ATEL [135] are indicated.

Conclusion and Outlook

7

The processing of IACT observations towards high-level data products needs in-depth knowledge of the system's performance in the form of IRFs, depending on the observation conditions and traditionally gained through extensive Monte Carlo simulations. Especially in circumstances where obtaining results on short time scales is of the utmost importance, these resource-intensive simulations cannot be computed using the full traditional analysis chain. One currently discussed approach to limit the need for simulations and enable analyses on short time scales, planned for the LST-1 in the context of the CTAO, is the inter- and extrapolation on a grid of precomputed IRFs. This work successfully implemented and tested said approach on toy data and actual observations of the Crab Nebula and NGC 1275, taken at zenith angles up to 35 deg, using point-like IRFs.

The results obtained from 35.9 h of Crab Nebula observation yield flux levels close to those already published by the MAGIC telescopes observing in the same energy range and tying into lower-energy results by *Fermi*-LAT. However, this work's results predict higher Crab Nebula fluxes than well-established references and shift the spectrum slightly towards higher energies, followed by a steeper decline than previously published. As this effect is apparent for estimated and nearest neighbor IRFs alike, the cause cannot lie with this work's estimation algorithms. As LST-1 is still undergoing commissioning and the more established experiments all rely on stereoscopic operation collecting more reliable information about the measured particles, this analysis should be revisited with future observations of an array of LSTs. This includes possible remaining bugs in the components of the analysis software. Currently, all parts of the analysis chain but `gammapy` are beta versions, and even though `gammapy` is available as a stable released software, development is still ongoing and essential analysis paradigms such as unfolded flux points are actively being worked on [32]. Despite the discrepancy to existing results, estimated IRFs proved to perform on par with nearest neighbor IRFs on dense IRF grids. With decreasing grid densities, estimated IRFs could maintain stable performances longer than the nearest neighbor analysis. This opens the possibility of limiting the number of Monte Carlo simulations, at least in the studied zenith range below 35 deg. As simulations use up a considerable amount of modern experiment budgets through computation hardware and power consumption, with directly connected negative consequences for the environment, this work can assist in enabling a more sustainable future for IACT experiments.

Applying estimated IRFs onto NGC 1275 data, taken in a period of flaring activity and thus data taken in an extent to be expected in case CTAO detects a transient event, yields results expected for flare follow-up observations. While the data taken after the first flare matches the cooling observed after previous flares, the second flare's follow-up behaves differently. As the time delay between the last reported flare by another experiment and the start of the three nights of observations was four days, a time scale on which previous NGC 1275 flaring states cooled towards their low states,

it was not expected to find comparable flux levels as with the first flare follow up. While this might indicate a different cooling mechanism at work in this instance, another possible explanation would be to attribute the measured flux to a different flare than the one reported by the MACE experiment for the night from January 10 to 11, 2022. This would make this presumed flare the third in a row of flaring activity. Contradicting this theory, no other experiment reported such findings. Unexpectedly, *Fermi*-LAT has not reported any NGC 1275 flaring activity during December 2022 and January 2023, despite being close to an "all-sky" observatory and a typical contributor to the observation of AGN flares. An analysis of existing *Fermi*-LAT data from this period might aid the further study of this sequence of NGC 1275 flares and the underlying physics and should thus be pursued. Regardless of these open questions, estimated IRFs showed themselves capable of facilitating data analysis in settings that are typically the main application case for short-time-scale or even RTAs to issue alerts to the scientific community. The results obtained from the physical analyses of NGC 1275 should be considered under this prerequisite and, thus, be primarily seen as an indicator to prepare a more in-depth analysis of the flares. This includes, but is not limited to, more specialized configurations for the high-level `gammapy` analysis, as this analysis used default values in many instances.

With the excellent performance of estimated IRFs under the circumstances discussed, the next logical step is to repeat such studies for more complicated environments. This includes the step from point-like IRFs towards full-enclosure analyses, adding a spatial component to the results. As the current simulation grid used for LST-1 does not offer the needed diffuse photon simulation at testing grid nodes, an extension of the simulations is imperative. Regardless, a first range of early 3D analyses, e.g., in [107], is actively developed for LST-1. Extending them with estimated PSFs can contribute to such studies. Another open question is the performance of estimated IRFs at zenith angles beyond 35 deg. This work omitted observations beyond that point due to the nature of the existing data and the current grid being regular only in parameters where linearity can only be assumed in a small angle approximation, as discussed in section 4.2. While a good performance of the estimated IRFs in settings where the assumption of linearity holds can be anticipated from this work, the nature of such a grid at high zenith angles is an open question. As final recommendation towards the refinement of the simulation grid, the points forming the convex hull should be moved slightly to also encapsulate the apex of the Crab Nebula trajectory or even the whole physically observable parameter space for LST-1. This would minimize the need for extrapolation, which performs less stable than interpolation algorithms.

Changes or extensions to the used grid parameters also offer the possibility of including more effects and existing auxiliary measurements. One candidate for an additional grid parameter might be the optical efficiency estimated from muon ring events. As muons form abundantly in EAS and, being charged, cause the emission of Cherenkov light, they are frequently detected by IACTs. Due to them originating relatively close to the telescopes, the Cherenkov emission can typically be measured without losses to parts of the emission falling outside the telescope's collection area. This data thus offers the possibility to get a handle on the optical efficiency of the whole telescope system and atmospheric conditions [62]. They are thus a prime candidate for an estimation parameter, including them in IACT analyses more meaningfully than currently. Such considerations should, however, always aim only to minimize the number of grid dimensions.

Another open question is the development of parameters for an IRF grid suitable for the use with a whole array of telescopes. While the definition of the parameters used for a monoscopic telescope is more or less straightforward, individual telescopes in extended arrays may experience different observation conditions. This may, e.g., present itself in different parameter values for each telescope, complicating the estimation of a suitable set of IRFs. This is especially the case when combining different telescope types, as planned for the CTAO.

Obvious room for future improvements to estimated IRFs lies within the employed estimation algorithms. While this thesis implemented and extended known algorithms already employed in particle physics, recent advancements in numerical mathematics offer interesting options. One notable example is the usage of spline interpolation for probability density functions varying with some time instance, or in this thesis' wording, some grid parameter value, as discussed in [6]. This method shows promise, especially in describing more complex probability density function shapes, a needed behavior as the currently used algorithms show declining performance as soon as Gaussianity can no longer be assumed. Another option lies within the advances in modern machine and deep learning. One simple idea is to use convolutions to combine the template IRFs with the respective grid points through convolutional neural networks toward the estimated IRF. As neural networks can work with high-dimensional inputs and especially map them onto non-linear functions, non-linear dependencies on, e.g., the zenith angle might be more efficiently implemented. While deep learning applications heavily depend on the amount of available training data, extended simulations would be needed in the case of IRFs. Using random numbers from known probability density functions with readily available random number generators can provide a proof-of-concept in a first test of this idea.

The remaining goal of this work is the inclusion into a RTA software for LST-1 and CTAO. One central aspect of a RTA, a strong focus on optimized computation time, has already been found significant consideration during the implementation of this work's algorithms. Consequently, using this work's estimated IRFs within the currently developed LST-1 RTA [42] should be straightforward. This RTA currently uses a shared IRF computed from simulations at a zenith angle of 20 deg and would, thus, profit from more closely matching IRFs. From there on, the next step is to use estimated IRFs with the intended science case, facilitating short time-scale analyses of transient events, including issuing alerts to the community. This will aid in understanding sources such as NGC 1275 with its many unresolved mysteries.

Bibliography

For closed-access publications, an open-access preprint, usually from the arXiv or alternatively through the NASA ADS, is also provided. Where an open-access version could not be found, this is noted.

1. A. Aab et al. (The Pierre Auger Collaboration). "The flux of ultra-high energy cosmic rays after ten years of operation of the Pierre Auger Observatory". In: *The Pierre Auger Observatory: Contributions to the 34th International Cosmic Ray Conference (ICRC 2015)*. 2015, pages 9–16.
   ARXIV: 1509.03732 [astro-ph.HE] (Cit. on p. 12)
2. M. G. Aartsen et al. "Measurement of the cosmic ray energy spectrum with IceTop-73". In: *Phys. Rev. D* 88.4, 042004, 2013, page 042004.
   DOI: 10.1103/PhysRevD.88.042004. ARXIV: 1307.3795 [astro-ph.HE] (Cit. on p. 12)
3. A. A. Abdo et al. "Fermi Large Area Telescope Observations of the Crab Pulsar and Nebula". In: *Astrophys. J.* 708.2, 2009, page 1254.
   DOI: 10.1088/0004-637X/708/2/1254 (Cit. on p. 9)
4. S. Abdollahi et al. "Incremental Fermi Large Area Telescope Fourth Source Catalog". In: *Astrophys. J. Suppl. Ser.* 260.2, 2022, page 53.
   DOI: 10.3847/1538-4365/ac6751 (Cit. on p. 3)
5. H. Abe et al. (the CTAO-LST project). "Observations of the Crab Nebula and Pulsar with the Large-sized Telescope Prototype of the Cherenkov Telescope Array". In: *Astrophys. J.* 956.2, 2023, page 80.
   DOI: 10.3847/1538-4357/ace89d (Cit. on pp. 49, 50, 61, 77)
6. I. Adouani and C. Samir. "Numerical algorithms for spline interpolation on space of probability density functions". In: *J. Comput. Appl. Math.* 42.3, 2023, page 127.
   DOI: 10.1007/s40314-023-02262-5. Note: No open access publication available. (Cit. on p. 89)
7. G. Agnetta et al. "Time structure of the extensive air shower front". In: *Astropart. Phys.* 6.3, 1997, pages 301–312.
   DOI: 10.1016/S0927-6505(96)00064-3. Note: No open access publication available. (Cit. on p. 15)
8. F. Aharonian et al. (The H.E.S.S. Collaboration). "Observations of the Crab nebula with HESS". In: *Astron. Astrophys.* 457.3, 2006, pages 899–915.
   DOI: 10.1051/0004-6361:20065351 (Cit. on p. 9)
9. J. Aleksić et al. "Black hole lightning due to particle acceleration at subhorizon scales". In: *Science* 346.6213, 2014, pages 1080–1084.
   DOI: 10.1126/science.1256183. ARXIV: 1412.4936 [astro-ph.HE] (Cit. on p. 10)

10. J. Aleksić et al. "Measurement of the Crab Nebula spectrum over three decades in energy with the MAGIC telescopes". In: *J. High Energy Astrophys.* 5-6, 2015, pages 30–38.
DOI: 10.1016/j.jheap.2015.01.002 (Cit. on pp. 9, 56, 57, 61, 62, 66, 67)

11. J. Aleksić et al. "The major upgrade of the MAGIC telescopes, Part II: A performance study using observations of the Crab Nebula". In: *Astropart. Phys.* 72, 2016, pages 76–94.
DOI: 10.1016/j.astropartphys.2015.02.005. ARXIV: 1409.5594 [astro-ph.IM] (Cit. on p. 17)

12. D. Alexandreas et al. "Status report on CLUE". In: *Nucl. Instr. Meth. A* 360.1, 1995, pages 385–389.
DOI: 10.1016/0168-9002(94)01622-4. Note: No open access publication available. (Cit. on p. 17)

13. P. Alfeld. *Triangular Extrapolation.* Tech. rep. Wisconsin Univ.-Madison Mathematics Research Center, 1984.
https://apps.dtic.mil/sti/pdfs/ADA144660.pdf (Cit. on p. 37)

14. M. Amenomori et al. (The Tibet ASγ Collaboration). "The All-Particle Spectrum of Primary Cosmic Rays in the Wide Energy Range from 10^{14} to 10^{17} eV Observed with the Tibet-III Air-Shower Array". In: *Astrophys. J.* 678.2, 2008, page 1165.
DOI: 10.1086/529514 (Cit. on p. 12)

15. H. Anderhub et al. "Design and operation of FACT – the first G-APD Cherenkov telescope". In: *J. Instrum.* 8.06, 2013, P06008.
DOI: 10.1088/1748-0221/8/06/P06008 (Cit. on p. 17)

16. C. D. Anderson. "The Positive Electron". In: *Phys. Rev.* 43, 6 1933, pages 491–494.
DOI: 10.1103/PhysRev.43.491 (Cit. on p. 15)

17. S. Ansoldi et al. (The MAGIC Collaboration). "Gamma-ray flaring activity of NGC 1275 in 2016–2017 measured by MAGIC". In: *Astron. Astrophys.* 617, 2018, A91.
DOI: 10.1051/0004-6361/201832895 (Cit. on pp. 2, 6, 10, 78, 80, 82–85)

18. M. Arakawa et al. "Detection of Small Flares from the Crab Nebula with *Fermi*-LAT". In: *Astrophys. J.* 897.1, 2020, page 33.
DOI: 10.3847/1538-4357/ab9368 (Cit. on p. 60)

19. W. D. Arnett et al. "Supernova 1987A." In: *Annu. Rev. Astron. Astrophys.* 27, 1989, pages 629–700.
DOI: 10.1146/annurev.aa.27.090189.003213. NASA ADS: 1989ARA&A..27..629A (Cit. on p. 7)

20. Astropy Collaboration et al. "The Astropy Project: Sustaining and Growing a Community-oriented Open-source Project and the Latest Major Release (v5.0) of the Core Package". In: *Astrophys. J.* 935.2, 2022, page 167.
DOI: 10.3847/1538-4357/ac7c74 (Cit. on p. 123)

21. A. M. Atoyan and C. D. Dermer. "Neutral Beams from Blazar Jets". In: *Astrophys. J.* 586.1, 2003, page 79.
DOI: 10.1086/346261 (Cit. on p. 11)

22. W. B. Atwood et al. “The Large Area Telescope on the Fermi Gamma-Ray Space Telescope Mission”. In: *Astrophys. J.* 697.2, 2009, pages 1071–1102.
DOI: 10.1088/0004-637X/697/2/1071 (Cit. on p. 1)

23. M. Baak et al. “Interpolation between multi-dimensional histograms using a new non-linear moment morphing method”. In: *Nucl. Instrum. Meth. A* 771, 2015, pages 39–48.
DOI: 10.1016/j.nima.2014.10.033 (Cit. on p. 35)

24. J. Ballet et al. (The Fermi-LAT collaboration). *Fermi Large Area Telescope Fourth Source Catalog Data Release 4 (4FGL-DR4).* 2024.
ARXIV: 2307.12546 [astro-ph.HE] (Cit. on p. 3)

25. Y. Becherini and M. Punch (The H.E.S.S. Collaboration). “Performance of HESS-II in multi-telescope mode with a multi-variate analysis”. In: *High Energy Gamma-Ray Astronomy: 5th International Meeting on High Energy Gamma-Ray Astronomy.* 2012, pages 741–744.
DOI: 10.1063/1.4772366. Note: No open access publication available. (Cit. on p. 17)

26. E. G. Berezhko. “Composition of Cosmic Rays Accelerated in Active Galactic Nuclei”. In: *Astrophys. J.* 698.2, 2009, page L138.
DOI: 10.1088/0004-637X/698/2/L138 (Cit. on p. 12)

27. K. Bernlöhr. “Impact of atmospheric parameters on the atmospheric Cherenkov technique”. In: *Astropart. Phys.* 12.4, 2000, pages 255–268.
DOI: 10.1016/S0927-6505(99)00093-6. ARXIV: astro-ph/9908093 [astro-ph] (Cit. on p. 32)

28. K. Bernlöhr. “Simulation of imaging atmospheric Cherenkov telescopes with CORSIKA and sim_telarray”. In: *Astropart. Phys.* 30.3, 2008, pages 149–158.
DOI: 10.1016/j.astropartphys.2008.07.009. ARXIV: 0808.2253 [astro-ph] (Cit. on p. 26)

29. K. Bernlöhr et al. “The Cosmic Ray Tracking (CRT) detector system”. In: *Nucl. Instr. Meth. A* 369.1, 1996, pages 284–292.
DOI: 10.1016/0168-9002(95)00772-5. Note: No open access publication available. (Cit. on p. 17)

30. K. Bernlöhr et al. *CTAO Simulation Telescope Models for CORSIKA and sim_telarray - prod5.* Version 1.0.0. Zenodo, 2022.
DOI: 10.5281/zenodo.6218687 (Cit. on p. 19)

31. H. J. Bhabha and W. Heitler. “The passage of fast electrons and the theory of cosmic showers”. In: *Proc. R. Soc. Lond. A* 159, 898 1937, pages 432–458.
DOI: 10.1098/rspa.1937.0082 (Cit. on p. 14)

32. N. Biederbeck. “Unfolding the spectrum of the blazar Markarian 421 using data from the first Large-Sized Telescope of the Cherenkov Telescope Array”. PhD thesis. TU Dortmund University, 2023.
DOI: 10.17877/DE290R-24039 (Cit. on pp. 47, 87)

33. A. J. Bird et al. “The Third IBIS/ISGRI Soft Gamma-Ray Survey Catalog”. In: *Astrophys. J. Suppl. Ser.* 170.1, 2007, page 175.
DOI: 10.1086/513148 (Cit. on p. 6)

34. O. Blanch et al. on behalf of the MAGIC collaboration. *Detection of flaring very-high-energy gamma-ray emission from NGC 1275 with the MAGIC telescopes*. 2022.
ATEL: 15820. Note: Astronomer's Telegram (Cit. on p. 73)

35. F. Bradascio on behalf of the CTA MST Project. "Status of the Medium-Sized Telescopes for the Cherenkov Telescope Array Observatory". In: *Proceedings of 38th International Cosmic Ray Conference — PoS(ICRC2023)*. 2023, page 859.
DOI: 10.22323/1.444.0859 (Cit. on p. 20)

36. T. Bretz et al. for the MAGIC Collaboration. "Comparison of On-Off and Wobble mode observations for MAGIC". In: *The MAGIC Project: Contributions to ICRC 2005, Pune, India, Part 3: MAGIC Detector and Analysis Details*. 2005, pages 11–14.
ARXIV: astro-ph/0508274 [astro-ph] (Cit. on p. 21)

37. T. Bretz. "Zenith angle dependence of the cosmic ray rate as measured with imaging air-Cherenkov telescopes". In: *Astropart. Phys.* 111, 2019, pages 72–86.
DOI: 10.1016/j.astropartphys.2019.02.004. ARXIV: 1902.03875 [astro-ph.IM] (Cit. on pp. 32, 33)

38. K. Brügge. "Unmasking the gamma-ray sky: Comprehensive and reproducible analysis for Cherenkov telescopes". PhD thesis. TU Dortmund University, 2019.
DOI: 10.17877/DE290R-20440 (Cit. on p. 11)

39. A. Burrows and D. Vartanyan. "Core-collapse supernova explosion theory". In: *Nature* 589.7840, 2021, pages 29–39.
DOI: 10.1038/s41586-020-03059-w. ARXIV: 2009.14157 [astro-ph.SR] (Cit. on pp. 7, 8)

40. Z. Cao et al. "Ultrahigh-energy photons up to 1.4 petaelectronvolts from 12 γ-ray Galactic sources". In: *Nature* 594.7861, 2021, pages 33–36.
DOI: 10.1038/s41586-021-03498-z. Note: No open access publication available. (Cit. on p. 1)

41. J. F. Carlson and J. R. Oppenheimer. "On Multiplicative Showers". In: *Phys. Rev.* 51, 4 1937, pages 220–231.
DOI: 10.1103/PhysRev.51.220. Note: No open access publication available. (Cit. on p. 14)

42. S. Caroff et al. on behalf of the CTA-LST Project. "The Real Time Analysis framework of the Cherenkov Telescope Array's Large-Sized Telescope". In: *Proceedings of 38th International Cosmic Ray Conference — PoS(ICRC2023)*. Vol. 444. 2023, page 616.
DOI: 10.22323/1.444.0616 (Cit. on p. 89)

43. P. A. Čerenkov. "Visible Radiation Produced by Electrons Moving in a Medium with Velocities Exceeding that of Light". In: *Phys. Rev.* 52, 4 1937, pages 378–379.
DOI: 10.1103/PhysRev.52.378. Note: Letter by P. A. Čherenkov, summarizing his research from 1934 to 1937, otherwise only available in Russian language. No open access publication available. (Cit. on p. 15)

44. Cherenkov Telescope Array Observatory and Cherenkov Telescope Array Consortium. *CTAO Instrument Response Functions - prod5 version v0.1*. Version v0.1. Zenodo, 2021.
DOI: 10.5281/zenodo.5499840 (Cit. on p. 30)

45. M. Chiaberge, A. Capetti and A. Celotti. "The HST view of FR I radio galaxies: evidence for non-thermal nuclear sources". In: *Astron. Astrophys.* 349, 1999, pages 77–87.
ARXIV: astro-ph/9907064 [astro-ph]. Note: Original journal reference not available online. (Cit. on p. 6)

46. J. Cortina for the CTA LST Collaboration. *Detection of enhanced very-high-energy gamma-ray emission from the radio-galaxy NGC1275 with the LST-1*. 2022.
ATEL: 15819. Note: Astronomer's Telegram (Cit. on pp. 6, 73, 77, 85)

47. J. Cortina on behalf of the CTA LST project. "Status of the Large Size Telescopes of the Cherenkov Telescope Array". In: *Proceedings of 36th International Cosmic Ray Conference — (ICRC2019)*. 2019, 653, page 653.
DOI: 10.22323/1.358.0653 (Cit. on p. 20)

48. CTA Consortium. *Science with the Cherenkov Telescope Array*. World Scientific, 2019.
DOI: 10.1142/10986 (Cit. on pp. 1, 7, 9)

49. A. Daum et al. "First results on the performance of the HEGRA IACT array". In: *Astropart. Phys.* 8.1, 1997, pages 1–11.
DOI: 10.1016/S0927-6505(97)00031-5. ARXIV: astro-ph/9704098 [astro-ph] (Cit. on p. 26)

50. H. Dembinski et al. *scikit-hep/iminuit*. Version v2.25.2. 2024.
DOI: 10.5281/zenodo.10638795 (Cit. on p. 46)

51. D. Depaoli et al. "Silicon photomultipliers for the SST camera of the Cherenkov Telescope Array". In: *13th International Conference on Position Sensitive Detectors*. 2024, page 169047.
DOI: 10.1016/j.nima.2023.169047 (Cit. on p. 20)

52. R. M. Dominik et al. "3C 84: a possibly precessing jet in 43-GHz observations". In: *Mon. Not. R. Astron. Soc.* 503.4, 2021, pages 5448–5454.
DOI: 10.1093/mnras/stab799 (Cit. on pp. 2, 6)

53. R. M. Dominik, M. Linhoff and J. Sitarek for the CTA Consortium. "Interpolation of Instrument Response Functions for the Cherenkov Telescope Array in the Context of pyirf". In: *Proceedings of 38th International Cosmic Ray Conference — PoS(ICRC2023)*. 2023, 618.
DOI: 10.22323/1.444.0618 (Cit. on pp. 24, 29, 35)

54. A. Donath et al. "Gammapy: A Python package for gamma-ray astronomy". In: *Astron. Astrophys.* 678, 2023, A157.
DOI: 10.1051/0004-6361/202346488 (Cit. on p. 46)

55. E. Dwek and F. Krennrich. "The extragalactic background light and the gamma-ray opacity of the universe". In: *Astropart. Phys.* 43, 2013, pages 112–133.
DOI: 10.1016/j.astropartphys.2012.09.003. ARXIV: 1209.4661 [astro-ph.HE] (Cit. on p. 13)

56. D. C. Ellison, F. C. Jones and S. P. Reynolds. "First-Order Fermi Particle Acceleration by Relativistic Shocks ". In: *Astrophys. J.* 360, 1990, page 702.
DOI: 10.1086/169156 (Cit. on p. 11)

57. M. Erdmann et al. “Origins of extragalactic cosmic ray nuclei by contracting alignment patterns induced in the galactic magnetic field”. In: *Astropart. Phys.* 108, 2019, pages 74–83.
DOI: 10.1016/j.astropartphys.2018.11.004 (Cit. on p. 13)

58. V. Fonseca on behalf of the HEGRA Collaboration. “Status of the HEGRA Experiment at La Palma”. In: *24th International Cosmic Ray Conference, Vol. 1*. 1995, page 474.
NASA ADS: 1995ICRC....1..474H (Cit. on p. 16)

59. I. M. Frank and I. E. Tamm. “Coherent Visible Radiation of Fast Electrons Passing Through Matter”. In: *Selected Papers*. Ed. by B. M. Bolotovskii, V. Y. Frenkel and R. Peierls. Springer Berlin Heidelberg, Berlin, Heidelberg, 1991, pages 29–35.
DOI: 10.1007/978-3-642-74626-0_2. Note: Translated reprint of the original publication. No open access publication available. (Cit. on p. 15)

60. S. Funk. “Ground- and Space-Based Gamma-Ray Astronomy”. In: *Annu. Rev. Nucl. Part. Sci.* 65.1, 2015, pages 245–277.
DOI: 10.1146/annurev-nucl-102014-022036 (Cit. on pp. 10, 11)

61. B. M. Gaensler and P. O. Slane. “The Evolution and Structure of Pulsar Wind Nebulae”. In: *Annu. Rev. Astron. Astrophys.* 44, 2006, pages 17–47.
DOI: 10.1146/annurev.astro.44.051905.092528. Note: No open access publication available. (Cit. on p. 8)

62. M. Gaug et al. “Using Muon Rings for the Calibration of the Cherenkov Telescope Array: A Systematic Review of the Method and Its Potential Accuracy”. In: *Astrophys. J. Suppl. Ser.* 243.1, 2019, page 11.
DOI: 10.3847/1538-4365/ab2123 (Cit. on p. 88)

63. E. Giro et al. “First optical validation of a Schwarzschild Couder telescope: the ASTRI SST-2M Cherenkov telescope”. In: *Astron. Astrophys.* 608, 2017, A86.
DOI: 10.1051/0004-6361/201731602 (Cit. on p. 20)

64. J. T. Gosling et al. “Ion acceleration at the earth’s bow shock: A review of observations in the upstream region”. In: *AIP Conf. Proc.* Vol. 56. 1. 1979, pages 81–99.
DOI: 10.1063/1.32069. Note: No open access publication available. (Cit. on p. 12)

65. V. Grebenyuk et al. “Energy spectra of abundant cosmic-ray nuclei in the NUCLEON experiment”. In: *Adv. Space Res.* 64.12, 2019, pages 2546–2558.
DOI: 10.1016/j.asr.2019.10.004. ARXIV: 1809.05333 [astro-ph.IM] (Cit. on p. 12)

66. K. Greisen. “End to the Cosmic-Ray Spectrum?” In: *Phys. Rev. Lett.* 16, 17 1966, pages 748–750.
DOI: 10.1103/PhysRevLett.16.748. Note: No open access publication available. (Cit. on p. 13)

67. C. R. Harris et al. “Array programming with NumPy”. In: *Nature* 585.7825, 2020, pages 357–362.
DOI: 10.1038/s41586-020-2649-2 (Cit. on p. 123)

68. R. G. Harrison. “The Global Atmospheric Electrical Circuit and Climate”. In: *Surv. Geophy.* 25.5, 2004, pages 441–484.
DOI: 10.1007/s10712-004-5439-8. ARXIV: physics/0506077 [astro-ph] (Cit. on p. 34)

69. D. Heck et al. *CORSIKA: a Monte Carlo code to simulate extensive air showers.* Tech. rep. 6019. Forschungszentrum Karlsruhe, 1998.
https://web.iap.kit.edu/corsika/physics_description/corsika_phys.pdf (Cit. on p. 15)

70. T. M. Heckman and P. N. Best. "The Coevolution of Galaxies and Supermassive Black Holes: Insights from Surveys of the Contemporary Universe". In: *Annu. Rev. Astron. Astrophys.* 52.1, 2014, pages 589–660.
DOI: 10.1146/annurev-astro-081913-035722 (Cit. on pp. 3, 6)

71. W. Heitler. *The quantum theory of radiation.* 2nd ed. Oxford University Press, 1944.
https://archive.org/details/in.ernet.dli.2015.37198 (Cit. on p. 14)

72. W. Herschel. "XIV. Experiments on the refrangibility of the invisible rays of the sun". In: *Philos. Trans. R. Soc.* 90, 1800, pages 284–292.
DOI: 10.1098/rstl.1800.0015 (Cit. on p. 1)

73. V. F. Hess. "Über Beobachtungen der durchdringenden Strahlung bei sieben Freiballonfahrten". In: *Phys. Z.* 13, 1912, pages 1084–1091.
INSPIRE HEP: 1623161. Note: Originally in German, English translation on arXiv. (Cit. on p. 1)

74. A. M. Hillas. "Cerenkov Light Images of EAS Produced by Primary Gamma Rays and by Nuclei". In: *19th International Cosmic Ray Conference (ICRC19), Volume 3.* 1985, page 445.
NTRS: 19850026666 (Cit. on p. 24)

75. A. M. Hillas. "Differences Between Gamma-Ray and Hadronic Showers". In: *TeV Gamma-Ray Astrophysics: Theory and Observations Presented at the Heidelberg Workshop, October 3–7, 1994.* Ed. by H. J. Völk and F. A. Aharonian. Springer Netherlands, Dordrecht, 1996, pages 17–30.
DOI: 10.1007/978-94-009-0171-1_2. NASA ADS: 1996SSRv...75...17H (Cit. on p. 16)

76. A. M. Hillas. "Evolution of ground-based gamma-ray astronomy from the early days to the Cherenkov Telescope Arrays". In: *Astropart. Phys.* 43, 2013, pages 19–43.
DOI: 10.1016/j.astropartphys.2012.06.002. Note: No open access publication available. (Cit. on p. 16)

77. W. Hillebrandt and J. C. Niemeyer. "Type Ia Supernova Explosion Models". In: *Annu. Rev. Astron. Astrophys.* 38, 2000, pages 191–230.
DOI: 10.1146/annurev.astro.38.1.191. ARXIV: astro-ph/0006305 [astro-ph] (Cit. on p. 7)

78. J. A. Hinton. "The status of the HESS project". In: *New Astron. Rev.* 48.5, 2004, pages 331–337.
DOI: 10.1016/j.newar.2003.12.004. ARXIV: astro-ph/0403052 [astro-ph] (Cit. on p. 17)

79. J. Holder. "VERITAS: Status and Highlights". In: *Proc. 32th International Cosmic Ray Conference.* 2011, page 137.
DOI: 10.7529/ICRC2011/V12/H11. ARXIV: 1111.1225 [astro-ph.HE]. Note: The DOI is currently broken. (Cit. on p. 17)

80. B. Hollister and A. Pang. *Interpolation of Non-Gaussian Probability Distributions for Ensemble Visualization.* Tech. rep. UC Santa Cruz, Baskin School of Engineering, 2013.
https://tr.soe.ucsc.edu/sites/default/files/technical-reports/UCSC-SOE-13-13.pdf (Cit. on p. 35)

81. S. Hori for the IceCube collaboration. *NGC 1275: Upper limits from a neutrino search with IceCube*. 2023.
ATEL: 15852. Note: Astronomer's Telegram (Cit. on p. 73)

82. IceCube Collaboration. "Observation of high-energy neutrinos from the Galactic plane". In: *Science* 380.6652, 2023, pages 1338–1343.
DOI: 10.1126/science.adc9818. ARXIV: 2307.04427 [astro-ph.HE] (Cit. on p. 2)

83. A. P. Igoshev, S. B. Popov and R. Hollerbach. "Evolution of Neutron Star Magnetic Fields". In: *Universe* 7.9, 2021.
DOI: 10.3390/universe7090351 (Cit. on p. 8)

84. D. Ivanov. "TA Spectrum Summary". In: *34th International Cosmic Ray Conference (ICRC2015)*. Vol. 34. 2015, 349, page 349.
DOI: 10.22323/1.236.0349 (Cit. on p. 12)

85. F. James and M. Roos. "Minuit - a system for function minimization and analysis of the parameter errors and correlations". In: *Comput. Phys. Commun.* 10.6, 1975, pages 343–367.
DOI: 10.1016/0010-4655(75)90039-9. Note: No open access publication available. (Cit. on p. 46)

86. K. G. Jansky. "Electrical Disturbances Apparently of Extraterrestrial Origin". In: *Proc. IRE* 21.10, 1933, pages 1387–1398.
DOI: 10.1109/JRPROC.1933.227458 (Cit. on p. 1)

87. C. U. Keller. "X-rays from the Sun". In: *Cell. Mol. Life Sci.* 51.7, 1995, pages 710–720.
DOI: 10.1007/BF01941268. Note: No open access publication available. (Cit. on p. 1)

88. L. Kimmel et al. *Slow but steady increase of brightness of NGC 1275 over the last 5 months*. 2023.
ATEL: 15938. Note: Astronomer's Telegram (Cit. on p. 73)

89. K.-L. Klein and S. Dalla. "Acceleration and Propagation of Solar Energetic Particles". In: *Space Sci. Rev.* 212.3, 2017, pages 1107–1136.
DOI: 10.1007/s11214-017-0382-4. ARXIV: 1705.07274 [astro-ph.SR] (Cit. on p. 12)

90. C. M. G. Lattes et al. "Processes Involving Charged Mesons". In: *Nature* 159.4047, 1947, pages 694–697.
DOI: 10.1038/159694a0. Note: No open access publication available. (Cit. on p. 15)

91. E. Lefa, S. R. Kelner and F. A. Aharonian. "On the Spectral Shape of Radiation due to Inverse Compton Scattering Close to the Maximum Cutoff". In: *Astrophys. J.* 753.2, 2012, page 176.
DOI: 10.1088/0004-637X/753/2/176 (Cit. on p. 10)

92. M. Lemoine-Goumard, B. Degrange and M. Tluczykont. "Selection and 3D-reconstruction of gamma-ray-induced air showers with a stereoscopic system of atmospheric Cherenkov telescopes". In: *Astropart. Phys.* 25.3, 2006, pages 195–211.
DOI: 10.1016/j.astropartphys.2006.01.005. ARXIV: astro-ph/0601373 [astro-ph] (Cit. on p. 26)

93. T.-P. Li and Y.-Q. Ma. "Analysis methods for results in gamma-ray astronomy." In: *Astrophys. J.* 272, 1983, pages 317–324.
NASA ADS: 1983ApJ...272..317L (Cit. on p. 22)

94. M. Linhoff et al. for the CTA Consortium and Observatory. "ctapipe – Prototype Open Event Reconstruction Pipeline for the Cherenkov Telescope Array". In: *Proceedings, 38th International Cosmic Ray Conference*. 2023, 703.
DOI: 10.22323/1.444.0703 (Cit. on p. 24)

95. R. López-Coto et al. for the CTA LST Project. "Physics Performance of the Large Size Telescope prototype of the Cherenkov Telescope Array". In: *Proceedings, 37th International Cosmic Ray Conference*. 2021, 806.
DOI: 10.22323/1.395.0806 (Cit. on p. 24)

96. E. Massaro et al. "Roma-BZCAT: a multifrequency catalogue of blazars". In: *Astron. Astrophys.* 495.2, 2009, pages 691–696.
DOI: 10.1051/0004-6361:200810161 (Cit. on p. 6)

97. E. Massaro et al. "Log-parabolic spectra and particle acceleration in the BL Lac object Mkn 421: Spectral analysis of the complete BeppoSAX wide band X-ray data set". In: *Astron. Astrophys.* 413.2, 2004, pages 489–503.
DOI: 10.1051/0004-6361:20031558. ARXIV: astro-ph/0312260 [astro-ph] (Cit. on p. 11)

98. J. Matthews. "A Heitler model of extensive air showers". In: *Astropart. Phys.* 22.5, 2005, pages 387–397.
DOI: 10.1016/j.astropartphys.2004.09.003. Note: No open access publication available. (Cit. on p. 14)

99. D. Maurin, F. Melot and R. Taillet. "A database of charged cosmic rays". In: *Astron. Astrophys.* 569, 2014, A32.
DOI: 10.1051/0004-6361/201321344 (Cit. on p. 12)

100. M. Meyer, D. Horns and H.-S. Zechlin. "The Crab Nebula as a standard candle in very high-energy astrophysics". In: *Astron. Astrophys.* 523, 2010, A2.
DOI: 10.1051/0004-6361/201014108 (Cit. on pp. 8, 9)

101. R. Mirzoyan. "The Development of Ground-Based Gamma-Ray Astronomy: A Historical Overview of the Pioneering Experiments". In: *Handbook of X-ray and Gamma-ray Astrophysics*. Ed. by C. Bambi and A. Santangelo. Springer Nature Singapore, Singapore, 2022, pages 1–26.
DOI: 10.1007/978-981-16-4544-0_62-1. ARXIV: 2406.15037 [astro-ph.HE] (Cit. on p. 17)

102. F. Mölder et al. "Sustainable data analysis with Snakemake". In: *F1000Research* 10.33, 2021.
DOI: 10.12688/f1000research.29032.2 (Cit. on p. 123)

103. J. M. C. Montanus. "An extended Heitler–Matthews model for the full hadronic cascade in cosmic air showers". In: *Astropart. Phys.* 59, 2014, pages 4–11.
DOI: 10.1016/j.astropartphys.2014.03.010. ARXIV: 1311.0642 [astro-ph.HE] (Cit. on p. 15)

104. J. A. Morales-Soto and J. C. Arteaga-Velázquez on behalf of the HAWC Collaboration. "The all-particle cosmic ray energy spectrum measured with HAWC". In: *37th International Cosmic Ray Conference*. 2022, 330, page 330.
DOI: 10.22323/1.395.0330 (Cit. on p. 12)

105. I. V. Moskalenko, T. A. Porter and A. W. Strong. "Attenuation of Very High Energy Gamma Rays by the Milky Way Interstellar Radiation Field". In: *Astrophys. J.* 640.2, 2006, pages L155–L158.
DOI: 10.1086/503524 (Cit. on p. 13)

106. H. Nagai et al. "Limb-Brightened Jet of 3C 84 Reveaked by the 43 GHz Very-Long-Baseline-Array Observation". In: *Astrophys. J.* 785.1, 2014, page 53.
DOI: 10.1088/0004-637X/785/1/53 (Cit. on p. 6)

107. L. Nickel. "We are number one – Searching for Gamma-Ray Emission from the Radio-Galaxy M87 in Data of the First Large-Sized Telescope of the Cherenkov Telescope Array Observatory". PhD thesis. TU Dortmund University, 2024.
DOI: 10.17877/DE290R-24492 (Cit. on pp. 47, 88)

108. C. Nigro et al. "Towards open and reproducible multi-instrument analysis in gamma-ray astronomy". In: *Astron. Astrophys.* 625, 2019, A10.
DOI: 10.1051/0004-6361/201834938 (Cit. on p. 28)

109. C. Nigro, T. Hassan and L. Olivera-Nieto. "Evolution of Data Formats in Very-High-Energy Gamma-Ray Astronomy". In: *Universe* 7.374, 2021.
DOI: 10.3390/universe7100374 (Cit. on pp. 28, 46)

110. J. B. Oke and W. L. W. Sargent. "The Nucleus of the Seyfert Galaxy NGC 4151". In: *Astrophys. J.* 151, 1968, page 807.
NASA ADS: 1968ApJ...151..807O. Note: Original journal reference not available online. (Cit. on p. 4)

111. R. A. Ong. "Very high-energy gamma-ray astronomy". In: *Phys. Rep.* 305.3, 1998, pages 93–202.
DOI: 10.1016/S0370-1573(98)00026-X. Note: No open access publication available. (Cit. on p. 1)

112. D. W. Pankenier. "Notes on translations of the East Asian records relating to the supernova of AD 1054". In: *J. Astron. Hist. Herit.* 9.1, 2006, pages 77–82.
NASA ADS: 2006JAHH....9...77P (Cit. on p. 8)

113. J. S. Perkins and G. Maier (The VERITAS Collaboration). *VERITAS Telescope 1 Relocation: Details and Improvements*. 2009.
ARXIV: 0912.3841 [astro-ph.IM] (Cit. on p. 17)

114. A. L. Read. "Linear interpolation of histograms". In: *Nucl. Instrum. Meth. A* 425.1, 1999, pages 357–360.
DOI: 10.1016/S0168-9002(98)01347-3. Note: No open access publication available. (Cit. on p. 35)

115. S. P. Reynolds. "Supernova Remnants at High Energy". In: *Annu. Rev. Astron. Astrophys.* 46, 2008, pages 89–126.
DOI: 10.1146/annurev.astro.46.060407.145237. Note: No open access publication available. (Cit. on p. 7)

116. G. H. Rieke. "History of infrared telescopes and astronomy". In: *Exp. Astron.* 25.1, 2009, pages 125–141.
DOI: 10.1007/s10686-009-9148-7. Note: No open access publication available. (Cit. on p. 1)

117. S. Ritt, R. Dinapoli and U. Hartmann. "Application of the DRS chip for fast waveform digitizing". In: *Proceedings of the 1st International Conference on Technology and Instrumentation in Particle Physics*. 2010, pages 486–488.
DOI: 10.1016/j.nima.2010.03.045. Note: No open access publication available. (Cit. on p. 22)

118. G. D. Rochester and C. C. Butler. "Evidence for the Existence of New Unstable Elementary Particles". In: *Nature* 160.4077, 1947, pages 855–857.
DOI: 10.1038/160855a0. Note: No open access publication available. (Cit. on p. 15)

119. E. E. Salpeter. "Accretion of Interstellar Matter by Massive Objects." In: *Astrophys. J.* 140, 1964, pages 796–800.
NASA ADS: 1964ApJ...140..796S. Note: Original journal reference not available online. (Cit. on p. 3)

120. C. K. Seyfert. "Nuclear Emission in Spiral Nebulae." In: *Astrophys. J.* 97, 1943, page 28.
NASA ADS: 1943ApJ....97...28S. Note: Original journal reference not available online. (Cit. on p. 3)

121. F. W. Stecker and M. H. Salamonm. "Photodisintegration of Ultra-High-Energy Cosmic Rays: A New Determination". In: *Astrophys. J.* 512.2, 1999, page 521.
DOI: 10.1086/306816 (Cit. on p. 13)

122. J. C. Street and E. C. Stevenson. "New Evidence for the Existence of a Particle of Mass Intermediate Between the Proton and Electron". In: *Phys. Rev.* 52, 9 1937, pages 1003–1004.
DOI: 10.1103/PhysRev.52.1003. Note: No open access publication available. (Cit. on p. 15)

123. M. Tanabashi et al. (Particle Data Group). "Review of Particle Physics". In: *Phys. Rev. D* 98, 3 2018, page 030001.
DOI: 10.1103/PhysRevD.98.030001 (Cit. on p. 16)

124. L. A. Tejedor et al. "An Analog Trigger System for Atmospheric Cherenkov Telescope Arrays". In: *IEEE Trans. Nucl. Sci.* 60.3, 2013, pages 2367–2375.
DOI: 10.1109/TNS.2013.2257852. Note: No open access publication available. (Cit. on p. 22)

125. L. A. Tejedor et al. "A Trigger Interface Board for the Large and Medium Sized telescopes of the Cherenkov Telescope Array". In: *Nucl. Instr. Meth. A* 1027, 2022, page 166058.
DOI: 10.1016/j.nima.2021.166058 (Cit. on pp. 16, 22)

126. Telescope Array Collaboration. "An extremely energetic cosmic ray observed by a surface detector array". In: *Science* 382.6673, 2023, pages 903–907.
DOI: 10.1126/science.abo5095. ARXIV: 2311.14231 [astro-ph.HE] (Cit. on p. 13)

127. A. Tramacere, E. Massaro and A. M. Taylor. "Stochastic Acceleration and the Evolution of Spectral Distributions in Synchro-Self-Compton Sources: A Self-Consistent Modeling of Blazar Flares". In: *Astrophys. J.* 739.2, 2011, page 66.
DOI: 10.1088/0004-637X/739/2/66 (Cit. on p. 11)

128. C. M. Urry and P. Padovani. "Unified Schemes for Radio-Loud Active Galactic Nuclei". In: *Publ. Astron. Soc. Pac.* 107.715, 1995, page 803.
DOI: 10.1086/133630 (Cit. on p. 4)

129. V. V. Vassiliev and S. J. Fegan. "Schwarzschild-Couder two-mirror telescope for ground-based gamma-ray astronomy". In: *Proceedings of the 30th International Cosmic Ray Conference (ICRC2007)*. 2007.
ARXIV: 0708.2741 [astro-ph] (Cit. on p. 20)

130. P. Virtanen. "SciPy 1.0: Fundamental Algorithms for Scientific Computing in Python". In: *Nat. Methods* 17, 2020, pages 261–272.
DOI: 10.1038/s41592-019-0686-2 (Cit. on p. 123)

131. S. P. Wakely and D. Horan. "TeVCat: An online catalog for Very High Energy Gamma-Ray Astronomy". In: *Proceedings of the 30th International Cosmic Ray Conference (ICRC2007)*. Vol. 3. 2008, pages 1341–1344.
NASA ADS: 2008ICRC....3.1341W (Cit. on pp. 3, 4, 106)

132. T. C. Weekes et al. "Observation of TeV Gamma Rays from the Crab Nebula Using the Atmospheric Cerenkov Imaging Technique". In: *Astrophs. J.* 342, 1989, pages 379–395.
NASA ADS: 1989ApJ...342..379W (Cit. on pp. 2, 3, 16)

133. K. K. Yadav. *MACE detection of very high energy gamma-ray flare from the radio galaxy NGC 1275*. 2022.
ATEL: 15823. Note: Astronomer's Telegram (Cit. on p. 73)

134. K. K. Yadav on behalf of the HiGRO Collaboration. "Status update of MACE Gamma-ray telescope". In: *Proceedings of 37th International Cosmic Ray Conference — PoS(ICRC2021)*. Vol. 395. 2021, page 756.
DOI: 10.22323/1.395.0756 (Cit. on p. 17)

135. K. K. Yaday on behalf of the MACE team. *Detection of Renewed Gamma-Ray Flare from the Radio Galaxy NGC 1275 with the MACE telescope*. 2023.
ATEL: 15856. Note: Astronomer's Telegram (Cit. on pp. 6, 73, 77, 85)

136. V. Zabalza. "Naima: a Python package for inference of particle distribution properties from nonthermal spectra". In: *34th International Cosmic Ray Conference (ICRC2015)*. 2015, 922.
DOI: 10.22323/1.236.0922 (Cit. on p. 11)

137. R. Zanin et al. "CTA – the World's largest ground-based gamma-ray observatory". In: *Proceedings of 37th International Cosmic Ray Conference — PoS(ICRC2021)*. 2021, 005.
DOI: 10.22323/1.395.0005 (Cit. on p. 19)

Glossary

θ_{cut} Tables of cut-values on the radial distance between assumed source position and reconstructed event position, also known as RAD_MAX-tables. 31, 35, 42–45, 49, 51, 77, 105

A_{eff} Effective Area, a combination of the experiment's sensitive area with the probability for a gamma ray with some true properties to be present in the final dataset as a gamma ray after all analysis steps. 30, 33, 35, 42–45, 105

AGN Active Galactic Nucleus, the core to a galaxy as, e.g., NGC 1275, a highly energetic environment able to accelerate particles to the highest energies. 2–9, 11, 12, 88, 103–105

ATEL Astronomer's Telegram, an online, short-notice, unedited publication service intended to quickly distribute information on important observations in astronomy. 73, 74, 77, 85

BLR Broad-Line Region, dense gas clouds around an AGN's SMBH with a high-velocity dispersion, thus emitting emission lines with high Doppler-broadening. 4–6, 11, 105

CMB Cosmic Microwave Background, the remnant of the last scattering surface before the universe became transparent to photons, cooled by redshifting to about 2.725 K. 9, 11, 13

Crab Nebula Supernova remnant to the supernova SN 1054 in the constellation of Taurus, also designated M 1 or Taurus A, the first detected VHE source and standard candle in VHE astronomy. iii–v, 2–4, 8–11, 16, 21, 26–28, 41, 42, 49–52, 54, 56–58, 60–64, 66, 68, 70, 73, 77, 78, 80, 85, 87, 88, 106–109, 122

CTAO Cherenkov Telescope Array Observatory, the next generation, community and proposal-driven IACT experiment, currently build at two sites, the ORM, La Palma, Spain, and the Paranal Observatory, Chile. iii, iv, 1, 2, 6, 7, 9, 10, 12, 15, 17, 19, 20, 23–26, 28, 30, 46, 47, 49, 56, 63, 87, 89, 103–106

DL0 Lowest CTAO low-level data level, providing photon count waveforms and timing information for each pixel from all pixels of one triggered telescope that contained a clearly visible Chrenkov peak. 23, 24

DL1a Second lowest CTAO low-level data level, providing images of photon deposition and arrival time for each pixel of one triggered telescope that was deemed to belong to an EAS. 23–25, 104

DL1b More advanced version of the second lowest CTAO low-level data level, providing parametrized versions of DL1a's images to allow for machine learning applications. 24–26, 30, 73, 77, 116, 124

DL2 Second highest CTAO low-level data level, providing estimated particle type, energy, source position, and arrival time for all events detected by one or more telescopes. iv, 25, 27–30, 45, 49, 50, 63, 77, 108, 116, 117, 124

DL3 Highest low-level data level, providing estimated particle type, energy, source position, and arrival time for selected signal event detected by one or more telescopes and the associated IRFs. 24, 27–29, 46, 49–51, 55, 77, 104, 108, 117, 125

DL4 Binned and thus reduced version of the DL3 files. 46, 126

DL5 Final science data products such as light curves or SEDs. 46, 47, 104, 126

DL6 Highest foreseen data level, collecting DL5 information from different sources, e.g., in source catalogs or sky surveys, in a long-term archived form. 47

DRS4 Fourth generation Domino Ring Sampler, hardware implementing a switched capacitor array capable of storing multiple signals on short time scales, developed at Paul Scherrer Institute, Switzerland. 22

EAS Extended Air Shower, cascade of secondary particles developing after a highly energetic primary particle interacted with Earth's atmosphere. 1, 14–17, 22, 24–27, 32, 33, 44, 88, 103

EBL Extragalactic Background Light, radiation emitted by resolved and unresolved sources filling the intergalactic vacuum. 13

FACT First G-APD Cherenkov Telescope, a monoscopic IACT at the ORM, pioneering the use of Silicon Photomultipliers instead of PMTs. 17, 20, 28

FEB Front-End Board, hardware to combine multiple PMTs in the LST camera. 22

Fermi-LAT *Fermi* Large Area Telescope, one of the instruments deployed with the *Fermi Gamma-ray Space Telescope*, observing between 50 MeV and 1 TeV. 1, 3, 9, 28, 59, 60, 73, 87, 88

FR Fanaroff-Riley types I and II, designations given to a class of AGN featuring strong radio emission. 6

HEGRA High-Energy-Gamma-Ray-Astronomy, an installation of different detection principles in VHE gamma-ray astronomy at the ORM, including five IACTs. 16, 17

H.E.S.S. High Energy Stereoscopic System, an array of five IACTs in the Khomas region, Namibia. 9, 17, 26, 28

IACT Imaging Air Cherenkov Telescope, a design principle for telescopes in VHE gamma-ray astronomy. 1–3, 6, 12, 16, 17, 20, 21, 28, 29, 32, 34, 49, 87, 88, 103–106

IC 310 Neighboring galaxy to NGC 1275 in the constellation of Perseus and another known TeV-radio galaxy, can be observed simultaneously with NGC 1275 by pointing to so-called Perseus-MA, the central point between both sources. 6, 10, 76

ICRS International Celestial Reference System, a reference system and its realizations originating from the barycenter of the solar system. 4, 29

IRF Instrument Response Function, description of an IACTs response to an incomming signal, containing A_{eff}, M_{EDisp} and PSF or θ_{cut} components. iii, iv, 2, 6, 26–33, 35, 37, 39–46, 49–52, 54–64, 66–70, 73, 77, 81, 87–89, 104, 124, 125

LST Large-Sized Telescope, the largest of the three planned telescope sizes for CTAO. 19, 20, 22, 30, 40, 49, 51, 56, 61, 87, 104, 105

LST-1 LST-Prototype, currently undergoing comissioning at ORM. iii–v, 2, 19–24, 26, 28, 35, 40, 46, 49, 56, 59, 61, 73, 74, 85, 87–89, 121, 122

M_{EDisp} Energy Dispersion or EDISP, conditional probability to reconstruct a gamma-ray of some true properties at a certain $\mu = \hat{E}/E$. 30, 31, 35, 40–42, 49, 105

MACE Major Atmospheric Cerenkov Experiment Telescope, one IACT observing at the Indian astronomical observatory Hanle in the Ladakh region, India. 17, 73, 74, 85, 88

MAGIC Major Atmospheric Gamma Imaging Cherenkov, an installation of two IACTs at the ORM. 9, 17, 22, 28, 46, 56, 58, 59, 61–64, 73, 77, 80–85, 87

MST Medium-Sized Telescope, the second-largest of the three planned telescope sizes for CTAO. 20

NGC 1275 TeV radio galaxy in the constellation of Perseus, also designated 3C 84 or Perseus A. iii–v, 2, 4, 6, 7, 10, 13, 23, 26, 27, 69, 73, 74, 76–78, 80–85, 87–89, 103, 105, 109, 111, 113, 115–117, 119, 120, 122, 124

NLR Narrow-Line Region, gas clouds beyond an AGN's BLR with comparably lower velocity dispersion, thus emitting emission lines with less Doppler-broadening. 4–6

NSB Night Sky Background, remaining light from several sources providing a background during astronomical observations. 22, 23

ORM Observatorio del Roque de los Muchachos, an astronomical observatory located at the Canary island of La Palma. 16, 17, 19, 20, 27, 34, 103–105

PMT PhotoMultiplier Tube, detector design that is capable of converting and amplifying (single) photons to an electrical signal. 16, 17, 20, 22, 23, 104

PSF Point Spread Function, conditional probability to reconstruct a gamma-ray of some true properties at a certain source position. 30, 31, 35, 88, 105

PWN Pulsar Wind Nebula, a form of SNR with a pulsar in its center. 8

R0 Lowest CTAO raw data level, providing two gain channels of 40 ns digitalized but uncalibrated waveforms from all pixels of the triggered telescope. 23

R1 Second lowest CTAO raw data level, providing two gain channels of 40 ns digitalized and calibrated waveforms from all pixels of a triggered telescope. 23

RTA Real Time Analysis, analysis software to enable a quick-look analysis on short time scales. 2, 10, 88, 89

SED Spectral Energy Distribution, the emitted, energy-dependent flux of an astrophysical source or some derivative of it. 2, 9–11, 46, 50, 51, 56–61, 63, 64, 66–68, 77, 78, 80–85, 104, 106, 109, 119, 120

SMBH Super Massive Black Hole, black holes with masses between 10^6 and 10^{10} solar masses $M_\odot$. 3–6, 11, 103

SNR SuperNova Remnant, the remains of a star that has undergone a supernova explosion, e.g., the Crab Nebula. 7, 8, 11, 12, 106

SSC Synchroton Self-Compton, model to explain common shapes of SEDs. 10, 11

SST Small-Sized Telescope, the smallest of the three planned telescope sizes for CTAO. 20

TeVCat Catalog of known sources of VHE gamma-ray emission [131]. 3, 4

VERITAS Very Energetic Radiation Imaging Telescope Array System, an array of four IACTs at the Fred Lawrence Whipple Observatory in Southern Arizona, USA. 17, 28

VHE Very-High Energy, a designation given to photons with energies between about 100 GeV to a few 100 TeV. iii, iv, 1–5, 7–13, 15–17, 19, 22, 28, 49, 50, 52, 54, 56, 58, 60, 62, 64, 66, 68, 70, 103, 104, 106

Configuration Files

This appendix contains the configuration files used with the analyses in this thesis.

A.1 Analysis of Crab Nebula data

The following configurations were used when analyzing Crab Nebula observations.

```
{
  "EventSelector": {
    "filters": {
      "intensity": [80, Infinity],
      "width": [0, Infinity],
      "length": [0, Infinity],
      "r": [0, 1],
      "wl": [0, 1],
      "leakage_intensity_width_2": [0, 1],
      "event_type": [32, 32]
    }
  },
  "DL3Cuts": {
    "min_event_p_en_bin": 100,
    "min_gh_cut": 0.1,
    "max_gh_cut": 0.95,
    "min_theta_cut": 0.05,
    "max_theta_cut": 0.32,
    "fill_theta_cut": 0.32,
    "allowed_tels": [1]
  },
  "DataBinning": {
    "true_energy_min": 0.002,
    "true_energy_max": 200,
    "true_energy_n_bins_per_decade": 5,
    "reco_energy_min": 0.002,
    "reco_energy_max": 200,
    "reco_energy_n_bins_per_decade": 5,
    "energy_migration_min": 0.2,
```

```
    "energy_migration_max": 5,
    "energy_migration_n_bins": 31,
    "fov_offset_min": 0.1,
    "fov_offset_max": 1.1,
    "fov_offset_n_edges": 9,
    "bkg_fov_offset_min": 0,
    "bkg_fov_offset_max": 10,
    "bkg_fov_offset_n_edges": 21,
    "source_offset_min": 0.0001,
    "source_offset_max": 1.0001,
    "source_offset_n_edges": 1000
  }
}
```

Listing 1: Configuration file used for the processing from DL2 to DL3 in the Crab Nebula analysis.

```
general:
  log:
    level: info
observations:
  datastore: None
  obs_time:
    start: null
    stop: null
  required_irf:
    - aeff
    - edisp
    - rad_max
datasets:
  type: 1d
  stack: False
  geom:
    wcs:
      skydir: { frame: icrs, lon: 83.633 deg, lat: 22.014 deg }
      binsize: 0.02 deg
      width: { width: 2.0 deg, height: 2.0 deg }
      binsize_irf: 0.2 deg
    selection: { offset_max: 2.5 deg }
    axes:
      energy:
        min: 10 GeV
        max: 100 TeV
        nbins: 32 # Corresponds to 8 bins per decade
      energy_true:
```

```
        min: 5 GeV
        max: 200 TeV
        nbins: 93 # Corresponds to 20 bins per decade
  background:
  method: "reflected"
  on_region: { frame: icrs, lon: 83.633 deg, lat: 22.014 deg, radius: 0.3 deg }
  containment_correction: False
fit:
  fit_range: { min: 50 GeV, max: 10 TeV }
flux_points:
  energy: { min: 30 GeV, max: 10 TeV, nbins: 20 }
  source: Crab
light_curve:
  energy_edges: { min: 100 GeV, max: 200 TeV, nbins: 1 }
  source: Crab
```

Listing 2: Configuration file used with `gammapy` in the Crab Nebula high-level analysis.

```
components:
  - name: Crab
    type: SkyModel
    spectral:
      type: LogParabolaSpectralModel
      parameters:
        - name: amplitude
          value: 3.05e-10
          unit: cm-2 s-1 TeV-1
        - name: alpha
          value: 2.25
          unit: ""
        - name: beta
          value: 0.114
          unit: ""
        - name: reference
          value: 0.4
          unit: TeV
          frozen: true
```

Listing 3: Configuration file used to define the SED model in the Crab Nebula analysis.

A.2 Analysis of NGC 1275 data

The following configurations were used when analyzing NGC 1275 observations.

```
{
    "source_config": {
        "EventSource": {
            "allowed_tels": [
                1
            ],
            "max_events": null
        },
        "LSTEventSource": {
            "default_trigger_type": "ucts",
            "allowed_tels": [
                1
            ],
            "min_flatfield_adc": 3000,
            "min_flatfield_pixel_fraction": 0.8,
            "calibrate_flatfields_and_pedestals": false,
            "EventTimeCalculator": {
                "dragon_reference_counter": null,
                "dragon_reference_time": null
            },
            "PointingSource": {
                "drive_report_path": null
            },
            "LSTR0Corrections": {
                "calib_scale_high_gain": 1.088,
                "calib_scale_low_gain": 1.004,
                "drs4_pedestal_path": null,
                "calibration_path": null,
                "drs4_time_calibration_path": null
            }
        }
    },
    "events_filters": {
        "intensity": [
            0,
            Infinity
        ],
        "width": [
            0,
            Infinity
        ],
        "length": [
            0,
            Infinity
```

```
        ],
        "wl": [
            0,
            Infinity
        ],
        "r": [
            0,
            Infinity
        ],
        "leakage_intensity_width_2": [
            0,
            Infinity
        ]
    },
    "n_training_events": {
        "gamma_regressors": 1.0,
        "gamma_tmp_regressors": 0.8,
        "gamma_classifier": 0.2,
        "proton_classifier": 1.0
    },
    "tailcut": {
        "picture_thresh": 8,
        "boundary_thresh": 4,
        "keep_isolated_pixels": false,
        "min_number_picture_neighbors": 2,
        "use_only_main_island": false,
        "delta_time": 2
    },
    "tailcuts_clean_with_pedestal_threshold": {
        "picture_thresh": 8,
        "boundary_thresh": 4,
        "sigma": 2.5,
        "keep_isolated_pixels": false,
        "min_number_picture_neighbors": 2,
        "use_only_main_island": false,
        "delta_time": 2
    },
    "dynamic_cleaning": {
        "apply": true,
        "threshold": 267,
        "fraction_cleaning_intensity": 0.03
    },
    "random_forest_energy_regressor_args": {
        "max_depth": 30,
```

```
        "min_samples_leaf": 10,
        "n_jobs": -1,
        "n_estimators": 150,
        "bootstrap": true,
        "criterion": "squared_error",
        "max_features": "auto",
        "max_leaf_nodes": null,
        "min_impurity_decrease": 0.0,
        "min_samples_split": 10,
        "min_weight_fraction_leaf": 0.0,
        "oob_score": false,
        "random_state": 42,
        "verbose": 0,
        "warm_start": false
    },
    "random_forest_disp_regressor_args": {
        "max_depth": 30,
        "min_samples_leaf": 10,
        "n_jobs": -1,
        "n_estimators": 150,
        "bootstrap": true,
        "criterion": "squared_error",
        "max_features": "auto",
        "max_leaf_nodes": null,
        "min_impurity_decrease": 0.0,
        "min_samples_split": 10,
        "min_weight_fraction_leaf": 0.0,
        "oob_score": false,
        "random_state": 42,
        "verbose": 0,
        "warm_start": false
    },
    "random_forest_disp_classifier_args": {
        "max_depth": 30,
        "min_samples_leaf": 10,
        "n_jobs": -1,
        "n_estimators": 100,
        "criterion": "gini",
        "min_samples_split": 10,
        "min_weight_fraction_leaf": 0.0,
        "max_features": "auto",
        "max_leaf_nodes": null,
        "min_impurity_decrease": 0.0,
        "bootstrap": true,
```

```
    "oob_score": false,
    "random_state": 42,
    "verbose": 0.0,
    "warm_start": false,
    "class_weight": null
},
"random_forest_particle_classifier_args": {
    "max_depth": 30,
    "min_samples_leaf": 10,
    "n_jobs": -1,
    "n_estimators": 100,
    "criterion": "gini",
    "min_samples_split": 10,
    "min_weight_fraction_leaf": 0.0,
    "max_features": "auto",
    "max_leaf_nodes": null,
    "min_impurity_decrease": 0.0,
    "bootstrap": true,
    "oob_score": false,
    "random_state": 42,
    "verbose": 0.0,
    "warm_start": false,
    "class_weight": null
},
"energy_regression_features": [
    "log_intensity",
    "width",
    "length",
    "x",
    "y",
    "wl",
    "skewness",
    "kurtosis",
    "time_gradient",
    "leakage_intensity_width_2",
    "az_tel",
    "alt_tel"
],
"disp_method": "disp_norm_sign",
"disp_regression_features": [
    "log_intensity",
    "width",
    "length",
    "wl",
```

```
        "skewness",
        "kurtosis",
        "time_gradient",
        "leakage_intensity_width_2",
        "az_tel",
        "alt_tel"
    ],
    "disp_classification_features": [
        "log_intensity",
        "width",
        "length",
        "wl",
        "skewness",
        "kurtosis",
        "time_gradient",
        "leakage_intensity_width_2",
        "az_tel",
        "alt_tel"
    ],
    "particle_classification_features": [
        "log_intensity",
        "width",
        "length",
        "x",
        "y",
        "wl",
        "signed_skewness",
        "kurtosis",
        "signed_time_gradient",
        "leakage_intensity_width_2",
        "log_reco_energy",
        "reco_disp_norm",
        "reco_disp_sign",
        "az_tel",
        "alt_tel"
    ],
    "allowed_tels": [
        1
    ],
    "write_pe_image": false,
    "mc_image_scaling_factor": 1,
    "image_extractor": "LocalPeakWindowSum",
    "image_extractor_for_muons": "GlobalPeakWindowSum",
    "CameraCalibrator": {
```

```
        "apply_waveform_time_shift": false
    },
    "time_sampling_correction_path": "default",
    "LocalPeakWindowSum": {
        "window_shift": 4,
        "window_width": 8,
        "apply_integration_correction": true
    },
    "GlobalPeakWindowSum": {
        "window_shift": 4,
        "window_width": 8,
        "apply_integration_correction": true
    },
    "timestamps_pointing": "ucts",
    "train_gamma_src_r_deg": [
        0,
        Infinity
    ],
    "source_dependent": false,
    "mc_nominal_source_x_deg": 0.4,
    "mc_nominal_source_y_deg": 0.0,
    "volume_reducer": {
        "algorithm": null,
        "parameters": {}
    },
    "calibration_product": "LSTCalibrationCalculator",
    "LSTCalibrationCalculator": {
        "systematic_correction_path": null,
        "squared_excess_noise_factor": 1.222,
        "flatfield_product": "FlasherFlatFieldCalculator",
        "pedestal_product": "PedestalIntegrator",
        "PedestalIntegrator": {
            "sample_size": 10000,
            "sample_duration": 100000,
            "tel_id": 1,
            "time_sampling_correction_path": null,
            "charge_median_cut_outliers": [
                -10,
                10
            ],
            "charge_std_cut_outliers": [
                -10,
                10
            ],
```

```
            "charge_product": "FixedWindowSum",
            "FixedWindowSum": {
                "window_shift": 6,
                "window_width": 12,
                "peak_index": 18,
                "apply_integration_correction": false
            }
        },
        "FlasherFlatFieldCalculator": {
            "sample_size": 10000,
            "sample_duration": 100000,
            "tel_id": 1,
            "time_sampling_correction_path": null,
            "charge_product": "LocalPeakWindowSum",
            "charge_median_cut_outliers": [
                -0.5,
                0.5
            ],
            "charge_std_cut_outliers": [
                -10,
                10
            ],
            "time_cut_outliers": [
                2,
                38
            ],
            "LocalPeakWindowSum": {
                "window_shift": 5,
                "window_width": 12,
                "apply_integration_correction": false
            }
        }
    },
    "waveform_nsb_tuning": {
        "nsb_tuning": false,
        "nsb_tuning_ratio": 0.52,
        "spe_location": "lstchain/data/SinglePhE_ResponseInPhE_expo2Gaus.dat"
    }
}
```

Listing 4: Configuration file used for the processing from DL1b to DL2 in the NGC 1275 analysis.

```
{
  "EventSelector": {
```

```
    "filters": {
      "intensity": [50, Infinity],
      "width": [0, Infinity],
      "length": [0, Infinity],
      "r": [0, 1],
      "wl": [0, 1],
      "leakage_intensity_width_2": [0, 1],
      "event_type": [32, 32]
    }
  },
  "DL3Cuts": {
    "min_event_p_en_bin": 100,
    "min_gh_cut": 0.1,
    "max_gh_cut": 0.95,
    "min_theta_cut": 0.05,
    "max_theta_cut": 0.32,
    "fill_theta_cut": 0.32,
    "allowed_tels": [1]
  },
  "DataBinning": {
    "true_energy_min": 0.002,
    "true_energy_max": 200,
    "true_energy_n_bins_per_decade": 5,
    "reco_energy_min": 0.002,
    "reco_energy_max": 200,
    "reco_energy_n_bins_per_decade": 5,
    "energy_migration_min": 0.2,
    "energy_migration_max": 5,
    "energy_migration_n_bins": 31,
    "fov_offset_min": 0.1,
    "fov_offset_max": 1.1,
    "fov_offset_n_edges": 9,
    "bkg_fov_offset_min": 0,
    "bkg_fov_offset_max": 10,
    "bkg_fov_offset_n_edges": 21,
    "source_offset_min": 0.0001,
    "source_offset_max": 1.0001,
    "source_offset_n_edges": 1000
  }
```

Listing 5: Configuration file used for the processing from DL2 to DL3 in the NGC 1275 analysis.

```
general:
  log:
```

```
    level: info

observations:
  datastore: None
  obs_time:
    start: null
    stop: null
  required_irf:
    - aeff
    - edisp
    - rad_max

datasets:
  type: 1d
  stack: False
  geom:
    wcs:
      skydir: { frame: icrs, lon: 49.950 deg, lat: 41.512 deg }
      binsize: 0.02 deg
      width: { width: 2.0 deg, height: 2.0 deg }
      binsize_irf: 0.2 deg
    selection: { offset_max: 2.5 deg }
    axes:
      energy:
        min: 50 GeV
        max: 100 TeV
        nbins: 34
      energy_true:
        min: 10 GeV
        max: 100 TeV
        nbins: 40
  background:
    method: "reflected"
  on_region: { frame: icrs, lon: 49.950 deg, lat: 41.512 deg, radius: 0.3 deg }
  containment_correction: False

fit:
  fit_range: { min: 80 GeV, max: 5 TeV }

flux_points:
  energy: { min: 100 GeV, max: 1 TeV, nbins: 10}
  source: NGC 1275

light_curve:
```

```
  energy_edges: { min: 100 GeV, max: 200 TeV, nbins: 1 }
  source: NGC 1275
```

Listing 6: Configuration file used with `gammapy` in the NGC 1275 high-level analysis.

```
components:
  - name: NGC 1275
    type: SkyModel
    spectral:
      type: LogParabolaSpectralModel
      parameters:
        - name: amplitude
          value: 1.0e-11
          unit: cm-2 s-1 TeV-1
        - name: alpha
          value: 2.0
          unit: ""
        - name: beta
          value: 0.1
          unit: ""
        - name: reference
          value: 0.3
          unit: TeV
          frozen: true
```

Listing 7: Configuration file used to define the SED model in the NGC 1275 analysis.

```
components:
  - name: NGC 1275
    type: SkyModel
    spectral:
        type: ExpCutoffPowerLawSpectralModel
        parameters:
        -   name: index
            value: 2.0
        -   name: amplitude
            value: 1.0e-12
            unit: cm-2 s-1 TeV-1
        -   name: reference
            value: 0.3
            unit: TeV
            frozen: true
        -   name: lambda_
            value: 0.1
            unit: TeV-1
        -   name: alpha
```

```
      value: 1.0
      frozen: true
```

Listing 8: Configuration file used to define the exponential cutoff power law SED model in the NGC 1275 analysis. As `gammapy` implements a more general version of this SED model with an additional parameter α, this parameter was fixed at 1, resulting in a fit of Equation 6.1.

Selected LST-1 Observation Runs

B

This appendix lists the identifying run numbers alongside the observation dates of the observation runs used in this work.

```
2020-11-17 : [2914]
2020-11-18 : [2929, 2930, 2931, 2932, 2933, 2934]
2020-11-19 : [2949, 2950]
2020-11-20 : [2967, 2968, 2969, 2970, 2971, 2972, 2973, 2974, 2975, 2976, 2977]
2020-11-21 : [2988, 2989, 2990, 2991, 2992]
2020-11-22 : [3004, 3005, 3006, 3007, 3008]
2020-12-07 : [3093, 3094, 3095, 3096]
2020-12-13 : [3231, 3232]
2020-12-14 : [3243]
2020-12-15 : [3270, 3271, 3272, 3273, 3274, 3275, 3276, 3277, 3278, 3279]
2020-12-17 : [3318, 3319, 3320, 3321]
2020-12-18 : [3328, 3329, 3330]
2020-12-19 : [3338, 3339, 3340]
2020-12-20 : [3355, 3356]
2020-12-21 : [3373]
2021-02-11 : [3598, 3599, 3600, 3601]
2021-02-12 : [3615]
2021-02-13 : [3632, 3633, 3634, 3635]
2021-02-15 : [3672, 3673, 3674, 3675, 3676, 3677]
2021-02-16 : [3706, 3707, 3708]
2021-03-15 : [4067, 4068]
2021-03-16 : [4086, 4087]
2021-09-04 : [6045]
2021-09-05 : [6073]
2021-09-14 : [6304]
2022-02-04 : [6872, 6873, 6874, 6875]
2022-02-05 : [6892, 6893, 6894, 6895]
2022-02-23 : [7097, 7098, 7099]
2022-02-28 : [7133, 7136]
2022-03-01 : [7161]
2022-03-02 : [7195, 7196, 7197, 7199, 7200]
2022-03-03 : [7227, 7228, 7231, 7232, 7233]
2022-03-04 : [7253, 7254, 7255, 7256]
```

```
2022-03-05 : [7274, 7275, 7276, 7277]
```

Listing 9: Observation runs used for the Crab Nebula analyses.

```
2022-12-21 : [11546, 11547, 11548, 11549, 11550]
2022-12-22 : [11566, 11568, 11569, 11570, 11571, 11572, 11573, 11574]
2022-12-23 : [11595, 11596, 11597, 11598, 11599]
2023-01-13 : [11618, 11619]
2023-01-14 : [11641, 11642, 11643, 11644]
2023-01-15 : [11660, 11661, 11662, 11663]
```

Listing 10: Observation runs used for the NGC 1275 analysis.

Software and Reproducibility

C

This appendix lists the environment files used with `snakemake==7.32.4` workflows [102] to compute this work's results in a reproducible manner. To create the respective environments, `snakemake` used `mamba==1.4.2` building upon `conda==23.3.1` as solver. The original environment files did not necessarily contain all fixed versions; they were added here as extracted from the resulting environments. The complete exports of the environments into `.yaml`-files are archived alongside this work's resources and workflows, as are the additional `pip`-installed custom `scriptutils` mentioned in the listings.

The implementations of the estimation algorithms created in this work are available in the GitHub-hosted `Python` software package `pyirf`. They rely heavily on `numpy` [67] and `scipy` [130] while using `astropy` [20] for unit handling.

```yaml
name: lst-v0.9
channels:
  - conda-forge
  - default
dependencies:
  - python=3.8.18
  - numpy=1.21.6
  - astropy=4.3.1
  - pip=24.0
  - scipy=1.10.1
  - ctapipe=0.12.0
  - gammapy=0.19
  - h5py=3.9.0
  - ipython=8.12.2
  - jupyter=1.0.0
  - notebook=7.1.1
  - iminuit=2.25.2
  - joblib=1.2.0
  - toml=0.10.2
  - protozfits=2.0.1.post1
  - protobuf=3.20.3
  - pyparsing=3.1.1
  - scikit-learn=1.0.2
  - numba=0.56.4
```

```
  - pydantic=1.10.13
  - pandas=1.5.3
  - pymongo=4.6.2
  - seaborn=0.13.2
  - jinja2=3.0.3
  - pip:
      - matplotlib=3.7.5
      - ctapipe-io-lst==0.18.3
      - ctaplot==0.6.4
      - pyirf==0.6.0
      - lstchain==0.9.14
    # - scriptutils
```

Listing 11: Environment with `lstchain==0.9.14`, used to process DL1b files in the NGC 1275 analysis and to compute IRFs from simulated DL2-files, as they were not yet reprocessed with `lstchain`-version 0.10.x and thus incompatible with the latter version.

```
name: pyirf-v0.10
channels:
  - conda-forge
dependencies:
  - python=3.11.8
  - numpy=1.26.4
  - ipython=8.22.1
  - jupyter=1.0.0
  - scipy=1.11.4
  - astropy=5.3.4
  - setuptools=69.1.1
  - tqdm=4.66.2
  - pyirf=0.10.1
  - uproot=4.3.7
  - awkward=1.10.3
  - gammapy=1.1
  - pip=24.0
  - pip:
    - matplotlib==3.7.5
    - ogadf_schema==0.2.4.post1
    # - scriptutils
```

Listing 12: Evironment used to estimate the IRFs.

```
name: lst-v0.10
channels:
  - conda-forge
dependencies:
  - python=3.11.8
```

```
  - numpy=1.26.4
  - scipy=1.11.4
  - astropy=5.3.4
  - pip=24.0
  - ctapipe=0.19.2
  - ctaplot=0.6.4
  - gammapy=1.1
  - h5py=3.10.0
  - ipython=8.22.1
  - jupyter=1.0.0
  - matplotlib=3.7.3
  - notebook=7.1.1
  - iminuit=2.25.2
  - joblib=1.2.0
  - toml=0.10.2
  - protobuf=3.20.3
  - pyparsing=3.1.1
  - scikit-learn=1.2.2
  - sphinx=4.5.0
  - sphinx-automodapi=0.17.0
  - sphinx_rtd_theme=1.3.0
  - sphinx-argparse=0.4.0
  - sphinxcontrib-mermaid=0.9.2
  - nbsphinx=0.9.3
  - numba=0.59.0
  - numpydoc=1.5.0
  - pandas=2.2.1
  - pymongo=4.6.2
  - seaborn=0.13.2
  - ctapipe_io_lst=0.22.6
  - pytest=8.0.2
  - lstchain=0.10.5
  - pydantic=1.10.13
# - pip:
    # - scriptutils
```

Listing 13: Environment with `lstchain==0.10.5`, used to generate DL3-files, as `lstchain` 0.9.x does not automatically handle the matching of observations with their respective nearest neighbor IRF, which was utilized heavily in this work to simplify the analysis workflow for both the estimated and nearest neighbor analyses.

```
name: gammapy
channels:
  - conda-forge
dependencies:
```

```
  - python=3.11.8
  - scipy=1.11.4
  - astropy=5.3.4
  - gammapy=1.1
  - pydantic=1.10.13
  # - pip:
    # - scriptutils
```

Listing 14: Environment used for the high-level analysis at DL4 and DL5.

Acknowledgements

First, I want to thank Prof. Dr. Dr. Wolfgang Rhode for providing me with this opportunity and for the countless possibilities to start an academic career, whether through helping me attend conferences, through discussion or any other support. I also thank Prof. Dr. Julia Tjus for kindly agreeing to act as a secondary advisor to this thesis.

Max, thank you for introducing me to the LST and CTAO community and for guiding me through this thesis. Lukas, thank you for helping me with `snakemake` and `gammapy` and especially for listening to my rants about this software. And for listening to my information about every upcoming Electric Callboy release, whether you cared or not. Thank you, Noah, for always helping me regardless of how basic my coding and configuration questions were, and for trying to introduce me to `Rust`. Dominik, thank you for always acting in the best interest of us Ph.D. students and helping us through academic bureaucracy. Andrea and Sarah, thank you for always ensuring that we can focus on our research and for always listening to our problems. Thank you, Kevin, Jonas, Felix, and everyone who shared an office with me, for the discussions and fun, both on and off-topic, and for becoming friends in the process. It was a delight sharing my time with you. While many of our breakfast group's members have already been personally thanked for different reasons, thanks again to all of you for bringing a bit of structure to our mornings. Thanks to every member of the chair of astroparticle physics for the discussions and the great working environment, and to every member of the LST and CTAO community for the help I got over the last years. Lastly, thanks to all of you that helped proof-reading this thesis: Lukas, Max, and Noah.

Thank you to everyone that have ever teached me anything: Teachers, Professors, all those outside an education institution.

I want to thank all those friends who supported me through my studies, especially Alexander, Felix, Jannine, Julian, Karl, and Yvonne. My special thanks have to go to Felix, for enduring this whole journey with me, from the first physics tutorial until now, both inside and outside this university. My further thanks have to go to all those committed to "our" DLRG Ortsgruppe Dortmund-Hombruch e.V., especially those of you trying to organize this bunch with me. Even though it is sometimes exhausting and demanding, this work would not have been finished without the distraction and meaning you provide to me. Thanks to everyone attending concerts and festivals with me, this thesis profitted from Q-Dance events; WOW WOW!

Lastly, there are the ones closest to me. To my family, especially my parents, thank you for the unconditional support you give me. Without your help, I would not have been able to finish my studies, or to start this project. And then, to Yvonne, thank you. Your unconditional love and support mean the world to me. Without you, this document would not exist and I would not be the person I am today.

Funding Acknowledgements

Part of this work has been supported by Deutsche Forschungsgemeinschaft (DFG) through the Collaborative Research Centers (Sonderforschungsbereiche – SFBs) SFB 876 "Providing Information by Resource-Constrained Analysis" and SFB 1491 "Cosmic Interacting Matters – From Source to Signal". The presentation and discussion of results obtained in this work at conferences were partly supported by the Wilhelm and Else Heraeus Stiftung and the Deutscher Akademischer Austauschdienst (DAAD).

I want to express my gratitude to the abovementioned funding agencies for providing me with the resources that made this work possible.